INFORMATION TO USERS

This manuscript has been reproduced from the microfilm master. UMI films the text directly from the original or copy submitted. Thus, some thesis and dissertation copies are in typewriter face, while others may be from any type of computer printer.

The quality of this reproduction is dependent upon the quality of the copy submitted. Broken or indistinct print, colored or poor quality illustrations and photographs, print bleedthrough, substandard margins, and improper alignment can adversely affect reproduction.

In the unlikely event that the author did not send UMI a complete manuscript and there are missing pages, these will be noted. Also, if unauthorized copyright material had to be removed, a note will indicate the deletion.

Oversize materials (e.g., maps, drawings, charts) are reproduced by sectioning the original, beginning at the upper left-hand corner and continuing from left to right in equal sections with small overlaps. Each original is also photographed in one exposure and is included in reduced form at the back of the book.

Photographs included in the original manuscript have been reproduced xerographically in this copy. Higher quality 6" x 9" black and white photographic prints are available for any photographs or illustrations appearing in this copy for an additional charge. Contact UMI directly to order.

UMI

A Bell & Howell Information Company
300 North Zeeb Road, Ann Arbor MI 48106-1346 USA
313/761-4700 800/521-0600

FLOW AND TURBULENCE IN A TIDAL CHANNEL

by

©Youyu Lu

B.Eng, Tsinghua University, 1986; MSc, Ocean University of Qingdao, 1991;

MSc, Memorial University of Newfoundland, 1994

A Dissertation Submitted in Partial Fulfillment of the

Requirements for the Degree of

DOCTOR OF PHILOSOPHY

in the

SCHOOL OF EARTH AND OCEAN SCIENCES

We accept this thesis as conforming

to the required standard

Dr. [illegible], Supervisor (School of Earth and Ocean Sciences)

Dr. A. Weaver, Departmental Member (School of Earth and Ocean Sciences)

Dr. R. Chapman, Departmental Member (School of Earth and Ocean Sciences)

Dr. C. Garrett, Outside Member (Department of Physics and Astronomy)

Dr. M. Foreman, Additional Member (Institute of Ocean Sciences)

Dr. S. Monismith, External Examiner (Department of Civil and Environmental Engineering, Stanford University)

Abstract

An acoustic Doppler current profiler (ADCP) has been tried and found suitable for taking profiles of the time-mean three-dimensional velocity, vertical shear, Reynolds stress and turbulent kinetic energy (TKE) density in a coastal tidal channel. The velocity profiles have been used to reveal the existence of a log-layer. The data collected with the ADCP have been combined with fine- and microstructure data collected with a moored instrument (TAMI) to examine the TKE budget and turbulence characteristics in tidal flows.

The ADCP was rigidly mounted to the bottom of the channel and the instrument was set to rapidly collect samples of along-beam velocities. In the derivation of the mean flow vector and the second-order turbulent moments, one must assume that the mean flow and turbulence statistics are homogeneous over the distance separating beam pairs. A comparison of the estimated mean velocity against the "error" velocity provides an explicit test for the assumption of homogeneity of the mean flow. The number of horizontal velocity estimates that pass a simple test for homogeneity increases rapidly with increasing averaging distance, exceeding 95% for distances longer than 55 beam separations. The Reynolds stress and TKE density are estimated from the variances of the along-beam velocities. Doppler noise causes a systematic bias in the estimates of the TKE density but not in the Reynolds stress. With increasing TKE density, the statistical uncertainty of the Reynolds stress estimates increases, whereas the relative uncertainty decreases. The spectra of the Reynolds stress and the TKE density are usually resolved; velocity fluctuations with periods longer than 20 minutes contribute little to the estimates.

Stratification in the channel varies with the strength of the tidal flow and is weak below mid-depth. The ADCP measurements provide clear examples of secondary

circulation, intense up/down-welling events, shear reversals, and transverse velocity shear. Profiles of the streamwise velocity are fitted to a logarithmic form with 1% accuracy up to a height, defined as the height of the log-layer, that varies tidally and reaches 20 m above the bottom during peak flows of 1 m s^{-1}. The height is well predicted by $0.04u_*/\omega$, where u_* is the friction velocity and ω is the angular frequency of the dominant tidal constituent. The mean non-dimensional shear, $(\partial U/\partial z)/(u_*/\kappa z)$, is within 1% of unity at the 95% level of confidence inside the log-layer.

Estimates of the rates of the TKE production and dissipation, eddy viscosity and diffusivity coefficients and mixing length, are derived by combining measurements with the ADCP and TAMI located at mid-depth. Near the bottom (z = 3.6 m), the production rate is 100 times larger than all other measurable terms in the TKE equation. Hence, the rate of production of TKE must be balanced by dissipation. The observed rate of production is proportional to the rate of dissipation calculated using the observed TKE density and mixing length, following the closure scheme of Mellor and Yamada (1974). This proportionality holds for the entire 3 decades of the observed variations in the rate of TKE production. At mid-depth, the eddy diffusivity of density and heat, deduced from microstructure measurements, agrees with the eddy viscosity derived from measurements with the ADCP.

The scaling of the log-layer height with tidal frequency in the channel is comparable to the scaling with Coriolis parameter for the log-layer in steady planetary boundary layer. However, some results are inconsistent with those from boundary layers over horizontal homogeneous bottoms. The Reynolds stress is not constant within the log-layer, and its magnitude at 3.6 m above the bottom is 3 times smaller than the shear velocity squared (u_*^2) derived from log-layer fitting. The peak of the non-dimensional spectrum for the Reynolds stress, when compared to measurements from atmospheric boundary layer, is shifted to higher wavenumbers by a factor of 2.5. One possible explanation for these discrepancies is the influence of horizontal

inhomogeneity caused by bed forms.

Examiners:

Dr. R. Luck, Supervisor (School of Earth and Ocean Sciences)

Dr. A. Weaver, Departmental Member (School of Earth and Ocean Sciences)

Dr. R. Chapman, Departmental Member (School of Earth and Ocean Sciences)

Dr. C. Garrett, Outside Member (Department of Physics and Astronomy)

Dr. M. Foreman, Additional Member (Institute of Ocean Sciences)

Dr. S. Monismith, External Examiner (Department of Civil and Environmental Engineering, Stanford University)

Table of Contents

List of Tables

List of Figures

Acknowledgments

I greatly appreciate my supervisor, Dr. Rolf Lueck, for providing me with the opportunity to study at University of Victoria. He has generously offered me his time and energy over the course of my thesis. His thoughtful design for the experiment is the key to this project's accomplishment. His guidance has covered a wide "spectrum," ranging from detailed data analysis techniques, proposal and testing of hypotheses, to the style of writing. He has always been encouraging, supporting my interest and choices. My thanks extends to the other members in my supervisory committee, Drs. Chris Garrett, Andrew Weaver, Ned Djilali, and Mike Foreman, for their advice on contemplating general scientific questions from this study. Dr. Foreman has set up three-dimensional numerical models for making comparisons with the measurement results. This model-data comparison work inspired the idea of connecting the measurements to the turbulence closure models. I appreciate the very constructive comments from the external examiner, Dr. Stephen Monismith, on subjects related to Chapter 6.

The field experiment was conducted with the excellent technical support of Don Newman, John Box, and Fabian Wolk. Daiyan Huang took part in the field work, and shared many techniques of data analyses with me during this study. He also provided his analyses of data from the moored instrument. Dr. David Farmer and his research group provided the meteorological and CTD data. Chin Yuen did the proof reading.

Upon finishing my graduate studies, I would like to take this opportunity to express my sincere thanks to my teachers, who have educated me in science and engineering in China and Canada. Dr. Richard Greatbatch and Prof. Shizuo Feng

have offered me continuous encouragement in my study of oceanography.

Within the School of Earth and Ocean Sciences, I would also like to thank Simon Holgate and my other fellow graduate students for sharing their ideas. Furthermore, I deeply appreciate the members of UVic's Chinese Student Association and many others for their friendship. Daiyan Huang, Jie Yang, Yongqin Pang, Lingqi Zhang, and Sheng Zhang are thanked for their help to my family.

I am indebted to my parents and parents-in-law, the siblings of both my wife and my own, for their tremendous support and encouragement during my study in Canada. Lastly but not least, my gratitude goes to my wife, Chunmei Yu, for her love and contribution during this busy period in our lives.

Chapter 1

Introduction and Motivation

1.1 Introduction

Fluid motions in natural environments are usually turbulent. The variations of a turbulent field cover a vast range of spatial and time scales. It is common practice to decompose a quantity into a "mean" component (averaging out turbulence) and a turbulent fluctuation component, and to describe the mean field and the statistics of the turbulence. In coastal seas, the flow and turbulence are stronger than in the open ocean. Turbulence plays important roles in the transfer of momentum and in the mixing of water properties and environmental tracers. Our ability to predict the behavior of the coastal environment depends largely on our understanding of the flow and mixing processes.

Field measurements and numerical modeling are two major approaches to the study of the physical oceanography of coastal seas. The challenge to field work is to measure the spatial and time variations of a quantity of interest, and this poses the need for efficient instrumentation. The validity of numerical models can depend largely on the accuracy of turbulent closure schemes. Numerical models always need to include empirical closure schemes for turbulence, partly because of the constraint imposed by computer power and partly because of the classical problem that the governing equations for the turbulent moments are not closed at any order. The feasibility of the closure schemes needs to be tested by comparing the model output against observations. So far, the models have been tested mainly on their ability to reproduce the time-mean field because of the lack of turbulence measurements. It

has been realized that more critical tests of turbulent parameterization should be on the ability of the models to describe the spatial variability and temporal evolution of the turbulent parameters (e.g., Brors and Eidsvik, 1994; Xing and Davies, 1996; Simpson et al., 1996).

In order to investigate a variety of new techniques for oceanic turbulence measurements, and to describe the tidally-forced turbulence characteristics, a multi-investigator experiment was conducted in a swift tidal channel along the coast of British Columbia. The two instruments deployed by our Ocean Turbulence Laboratory, University of Victoria, are a broadband acoustic Doppler current profiler (ADCP) and a novel moored microstructure instrument. The objectives of this thesis are to investigate the use of an ADCP to measure flow and turbulence in a highly turbulent environment; to study the tidally forced flow and turbulence characteristics in the channel from the measurements of the ADCP and the moored microstructure instrument; and to test some aspects of the turbulent closure schemes with the available data. The next two sections explain the application of an ADCP to oceanic measurements and the study of tidally forced flow and turbulence in coastal waters.

1.2 Measurement methods

Conventional instruments to measure oceanic flow are various types of point current meters and expendable current profilers. An ADCP offers significant advantages over these conventional instruments: it can remotely sense the spatial variation of the flow and its evolution with time. The spatial resolution and profiling range of an ADCP are usually adequate to measure the flow and shear throughout a large portion of water column in coastal seas. However, the measurement principles of an ADCP differ from those of the point current meters and the expendable current profilers. The difference prevents an ADCP from measuring the instantaneous velocity vector in a turbulent flow and poses requirements on the amount of averaging needed to

derive the time-mean flow vector. The estimates of the mean flow also contain an uncertainty due to turbulent fluctuations.

Oceanic turbulence measurements have been taken for more than 30 years since the pioneering work of Grant et al. (1962). Away from the boundaries, turbulence is essentially assessed by measuring velocity (and/or temperature) fluctuations at dissipation scales. Conventionally, velocity fluctuations are measured by mounting shear probes (Osborn and Crawford, 1980) on free-falling (e.g. Dewey and Crawford, 1988), towed (e.g.Lueck, 1987), or moored bodies (Lueck et al., 1996; Lueck and Huang, 1997). The quantity derived from these measurements is the dissipation rate of turbulent kinetic energy (TKE). Near the boundaries, such as the upper mixed layer under the sea ice (McPhee, 1994) and the bottom boundary layer near the seabed (e.g. Gross and Nowell, 1983, 1985), point current meters are used. These current meters are capable of sampling data at rapid rates, and offer estimates of the TKE dissipation rate, the Reynolds stress, and the TKE density. An array of current meters is needed to resolve the spatial variability of the turbulent quantities. Turbulence measurements using current meters are usually confined within a short (typically a few meters) distance from the bottom because of constraints on the size of the frame to which the current meters are mounted.

The ability of an ADCP to remotely sense velocity and to sample data at rapid rates lends it to the estimation of turbulent quantities. An ADCP provides an efficient way to study the structure of turbulent boundary layers in coastal waters, since the layer usually extends to large distances from the bottom and can cover the whole water depth (Bowden, 1978; Soulsby, 1983). So far several approaches have been designed to estimate turbulent quantities with an ADCP (see section 4.1). In this contribution, we study the "variance technique" proposed by Lohrmann et al. (1990).

1.3 Tidally forced flow and turbulence in coastal seas

Apart from forcing by atmospheric motions and fresh water input at the air-sea or sea-land interfaces, a major driving force of flow and turbulence in coastal waters is the tide. The time-mean flow and turbulence interact with each other due to the nonlinearity of the motions. Swift currents rub against solid boundaries (the seabed and coast), causing shear in the flow field. Shear instability is a major mechanism of turbulence production. Kinetic energy is passed from the mean flow to turbulence by a cascade from large to small scale eddies and is finally dissipated at the smallest scales by molecular diffusion.

The frictional force at the seabed plays an important role in the momentum balance, and the velocity varies rapidly with height. Velocity profiles are shaped by turbulent momentum fluxes. Scaling arguments of classical turbulent theory lead to a logarithmic velocity profile in the boundary layer (e.g., Tennekes and Lumley, 1972). It is important to verify the existence of the log-layer in oceanic boundary layers because it provides an estimate of the bottom drag force and is a necessary condition to justify the scaling arguments. Previous studies have only convincingly revealed the existence of the log-layer in the near-bottom region of tidal boundary layers, and showed that modifications on the classical scaling arguments are frequently required to explain the complexity in the measured velocity profiles (see section 5.1). Log-layers extending to large distances above the seabed have not been convincingly observed until now.

The description of turbulence requires the measurements of various scalings and moments of turbulent fluctuations. The measurement of a turbulent quantity usually requires a specific instrument or technique. The opportunity to get more than one estimate of turbulent quantities from a field experiment, especially to resolve both the spatial and time variations, is rare. In this study, measurements with two instruments provide estimates of turbulent quantities at both the energy-containing

and dissipation scales. Combined with measurements of the mean flow and density gradient, the turbulent quantities provide estimates of the eddy viscosity/diffusivity coefficients and the mixing length. The estimated quantities provide a description of the spatial and time variations of turbulence in the channel.

Turbulent closure models are commonly composed from scaling arguments and include empirical constants to be determined. Higher order turbulent closure schemes are designed to reduce the level of arbitrariness in parameterization, but more scalings, moments, and empirical constants are involved. For example, the hierarchy of closure models proposed by Mellor and Yamada (1974,, 1982) includes parameterization of the mixing coefficients and dissipation rate as functions of the TKE density and a mixing length. Tests on the feasibility of such schemes require measurements of the second-order moments of turbulent fluctuations. Although laboratory and atmospheric measurements have been used to test the closure models and to determine the empirical constants (Mellor and Yamada, 1982), such tests are lacking for the oceanic environment.

The scalings of turbulence are simplified if the TKE budget reduces to a local balance. The evaluation of the magnitudes of the terms contained in the TKE conservation equation is required to examine the local TKE balance. In this study, the local TKE balance in the tidal boundary layer is examined using measurements and quantities derived with the Mellor-Yamada closure.

1.4 Plan of this thesis

In the rest of this thesis, a description of the study area, experiment setup and background measurements, and the deployment method of the ADCP, is first provided in Chapter 2. Chapters 3 to 6 are the main contents of the four papers I (in collaboration with Dr. R. G. Lueck) wrote during my PhD program. New insights of this thesis are further highlighted in the introduction section of each of these chapters. Specific

topics to be addressed are measurement and data handling techniques to estimate the mean flow and shear (Chapter 3), turbulent quantities (Chapter 4), the log-layer revealed from analyses of the mean velocity profiles (Chapter 5), and the turbulence characteristics from analyses of measurement results with the ADCP and a moored instrument (Chapter 6). General conclusions of this thesis are presented in Chapter 7.

Chapter 2

Experiment and Study Area

2.1 Experiment Description

The coastal waters between Vancouver Island and the mainland of North America are composed of a chain of straits, with both the northern (Queen Charlotte Strait) and the southern (Juan de Fuca Strait) ends open to the Pacific Ocean. Our experimental site, Cordova Channel, is a side channel among a series of narrow passages that link Juan de Fuca Strait to the Strait of Georgia. There is a substantial estuarine circulation in this area due to the runoff of several rivers, of which the Fraser River is the largest. Tidal flow is strong in these straits and increases when passing through the channels. Strong mixing occurs in these passages, significantly influencing the estuarine circulation (e.g., Thompson, 1981; Foreman et al., 1995).

A multi-investigator experiment in Cordova Channel was conducted in from September 19 - 30, 1994. Fig. 2.1 shows a map of the experiment site. Most of the measurements were taken in the narrowest part of the channel which has a width about 1 km and a depth about 30 m. The eastern side of the channel is bounded by James Island and has a fairly smooth curvature. The western boundary presents a headland (Cordova Spit) and a shallow bay (Saanichton Bay) that broadens the channel to the north (see the 20-m isobath). The channel to the south of the headland is fairly straight.

The two instruments deployed by our group are a 600 kHz ADCP and a moored microstructure instrument (TAMI). Fig. 2.2 summarizes the durations of the measurements with the standard working mode (mode 4) of the ADCP and two deployments

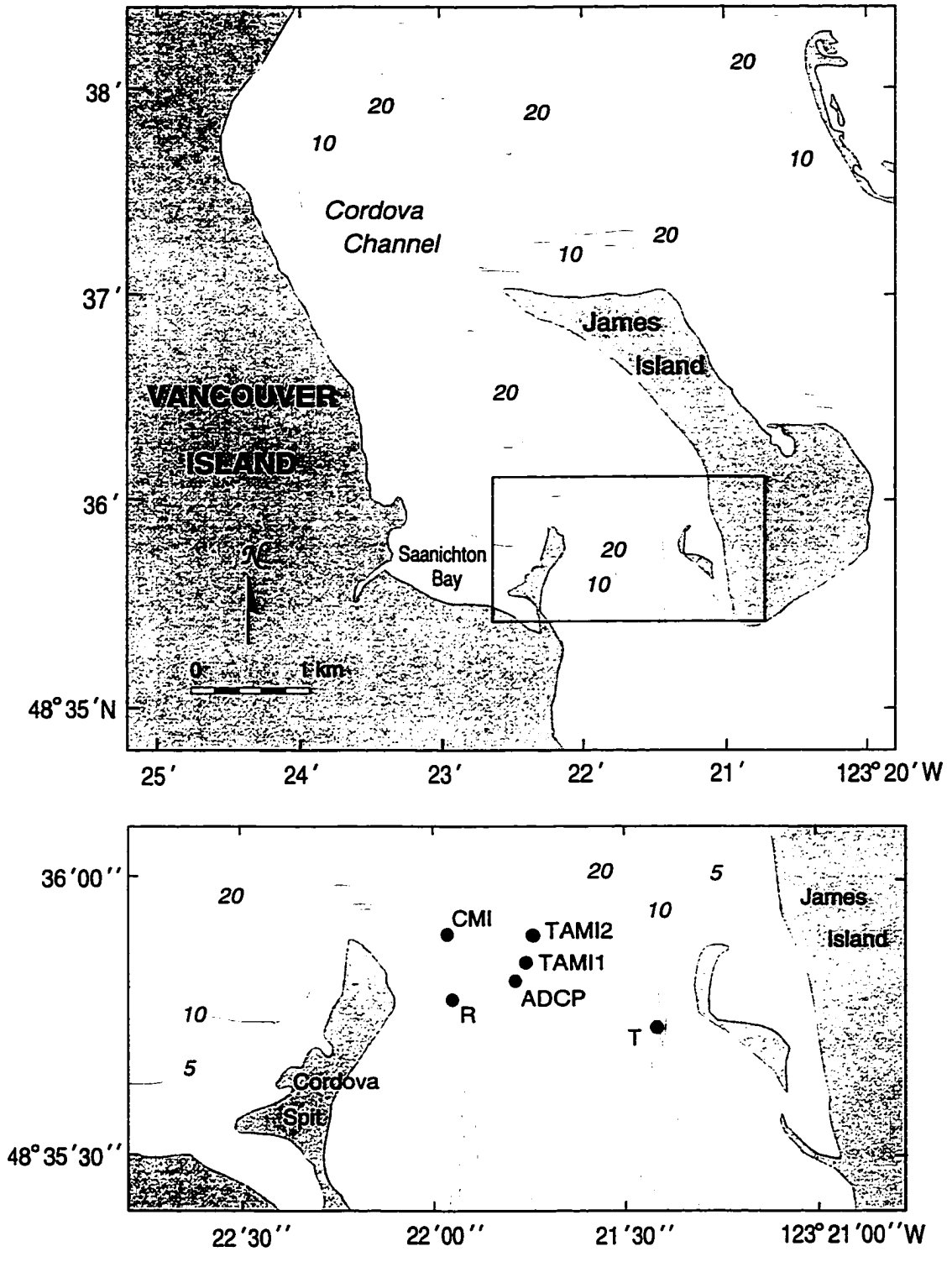

Figure 2.1: Area map showing bathymetry (depth in metres) of Cordova Channel and location of the ADCP. The positions of two deployments of the moored microstructure instrument (TAMI1 and TAMI2) are shown. A current meter (CMI), transmitter (T) and receiver (R) of an acoustic scintillation system were also deployed during the experiment.

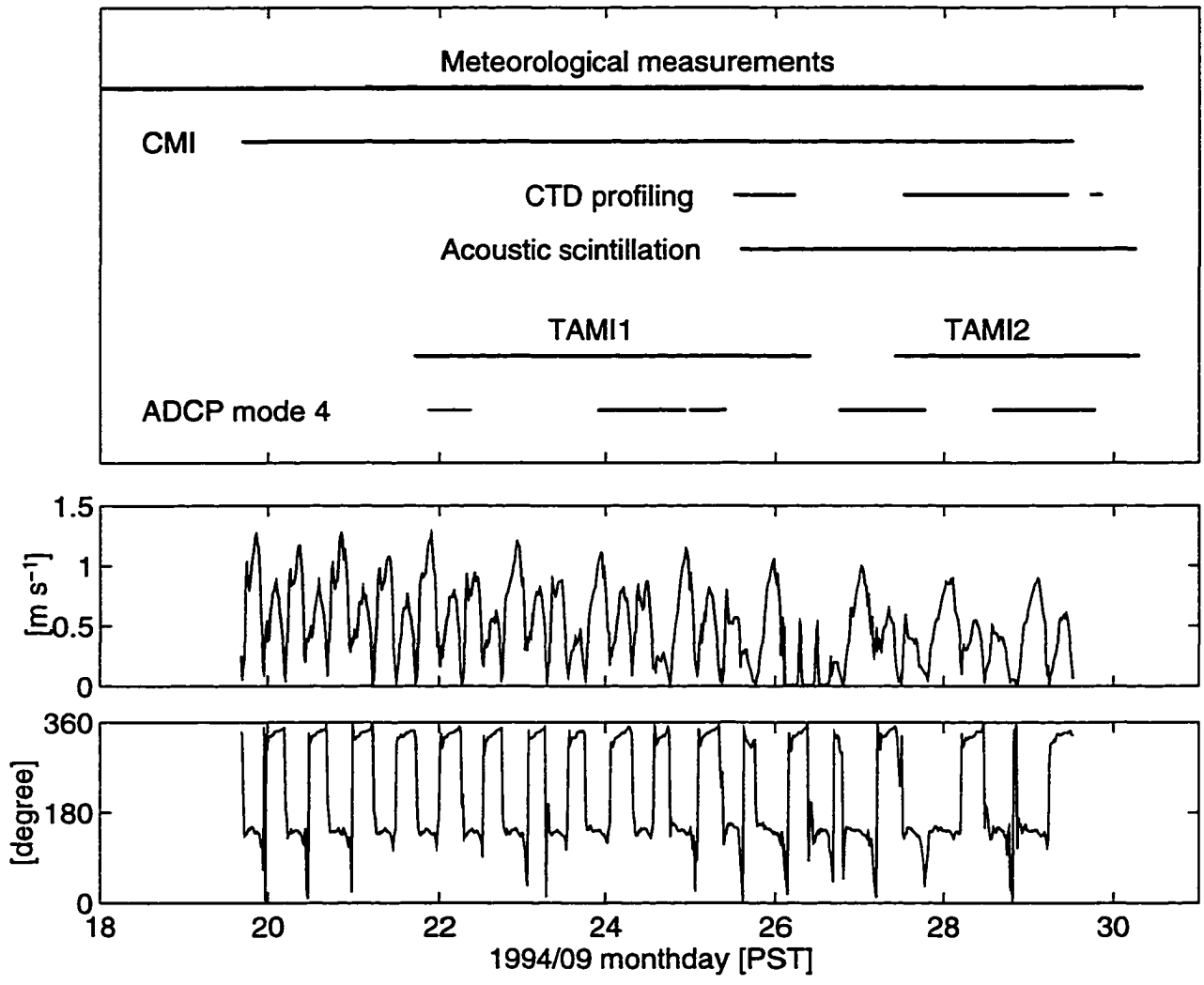

Figure 2.2: Durations of measurements made by some of the instruments deployed in the Cordova Channel experiment (top panel). The two lower panels show the magnitude and direction of the 20-min mean flow at mid-depth, measured by the moored current meter (CMI). During the first interval the ADCP only measured the mean flow profiles.

of TAMI, along with the measurements taken by the Acoustic Oceanography Group from the Institute of Ocean Sciences (IOS) at Patricia Bay.

2.2 Background Measurements

A meteorological station was set up at Cordova Spit and took measurements throughout the experiment. The recorded wind speed was typically less than 3 m s^{-1}, and only reached 5 m s^{-1} occasionally. The wind stress on the sea surface was negligible compared to the frictional stress at the bottom. The water surface was calm and, according to our visual observation, the wave heights did not exceed 0.2 m during the experiment. No systematic observation on the seabed condition was made, but divers reported that the bed was composed mainly of fine gravel with diameters ranging from 2 to 8 $\times$ 10^{-3} m, and that the bed contained neither mud nor silt.

The two lower panels in Fig. 2.2 show the magnitude and direction of the flow measured with the moored current meter (CMI) at mid-depth. The flow in the channel was mainly tidal, directed northward during the flood and southward during the ebb. During the experiment the tide changed from spring to neap, and the diurnal constituents became increasingly dominant.

Time variations of temperature and salinity at mid-depth were measured with a CTD attached to the CMI mooring and by 3 sensor pairs mounted on TAMI. The measurements showed a general warming trend of 1°C coupled with a decrease in salinity of 1.5 psu over 9 days. A close look at the time series (Fig. 2.3) revealed variations in temperature and salinity over several hours. Decreasing salinity correlated well with the increasing temperature.

CTD profiles were taken nominally every 20 min during the period shown in Fig. 2.2, from *CSS VECTOR* anchored near the south entrance of the channel, about 1.5 km to the south of the ADCP. Fig. 2.4 shows 17 consecutive density (σ_t) profiles over one-half semidiurnal tidal period from day 29.1–29.4. A fairly well mixed layer

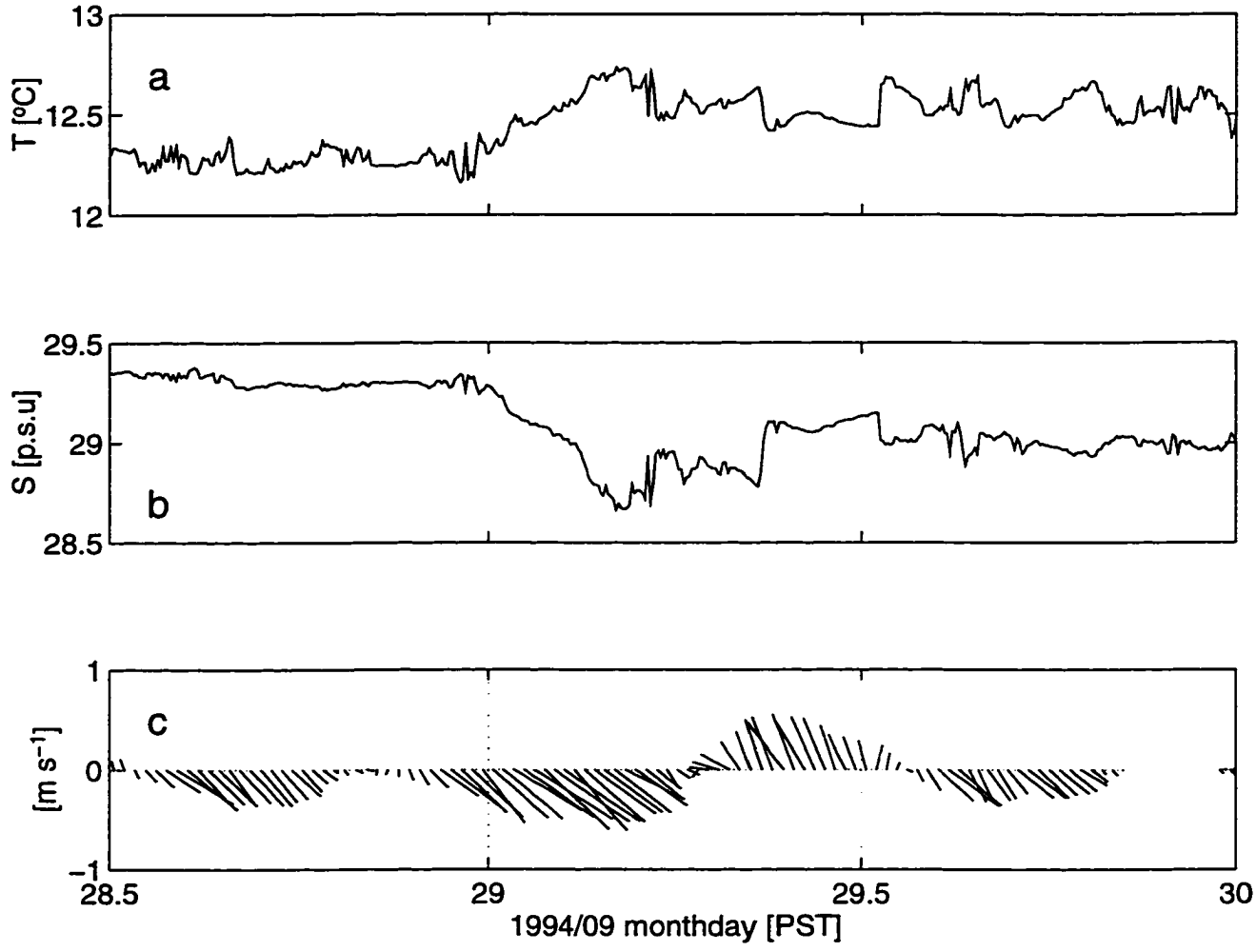

Figure 2.3: Water temperature (a), salinity (b), and 20-min mean flow (c) measured by TAMI at mid-depth.

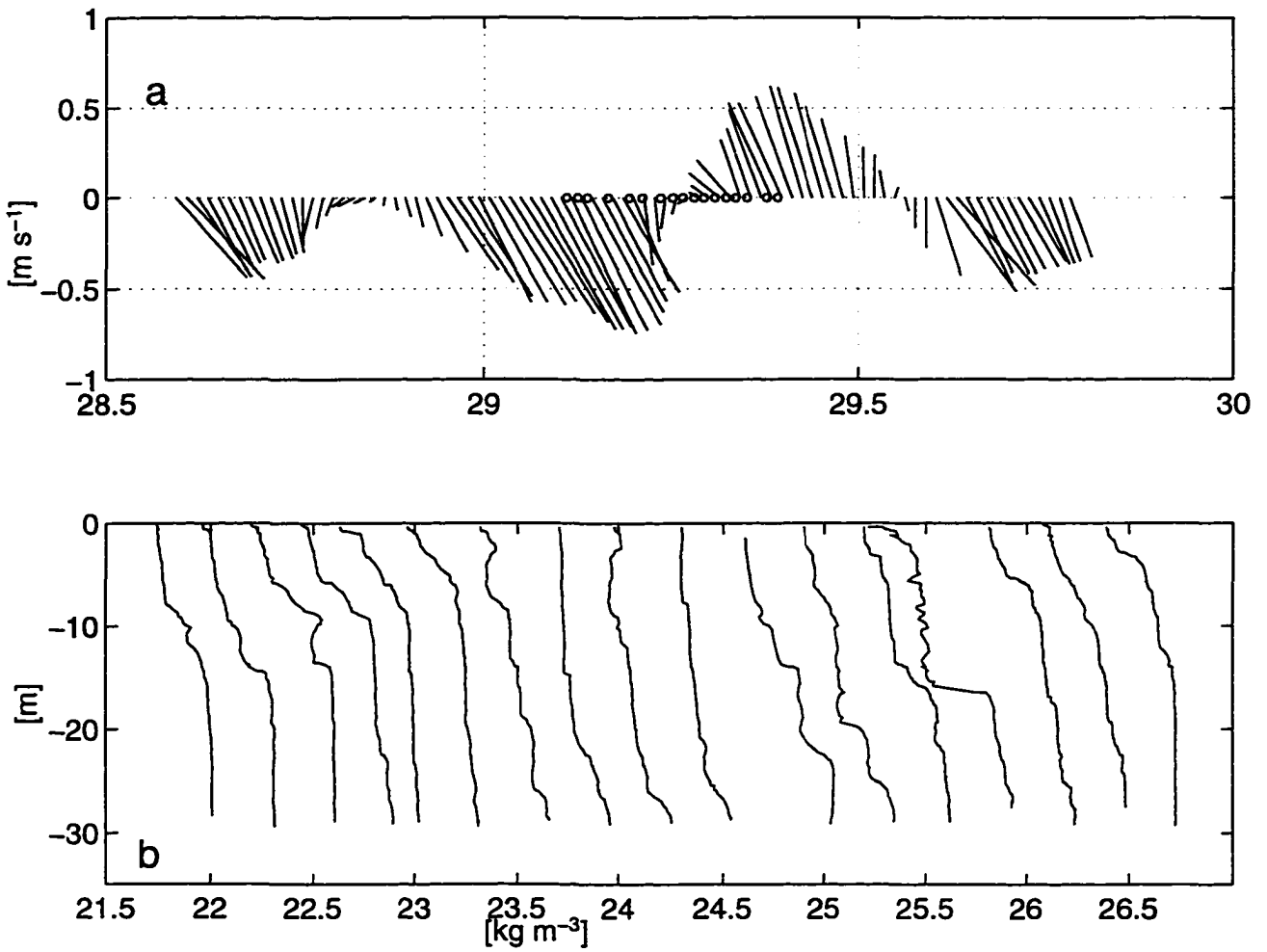

Figure 2.4: (a) 20-min depth mean flow measured by the ADCP and (b) consecutive profiles of seawater density (σ_t) collected by *CSS VECTOR* over one-half of the tidal period shown by open circles in (a).

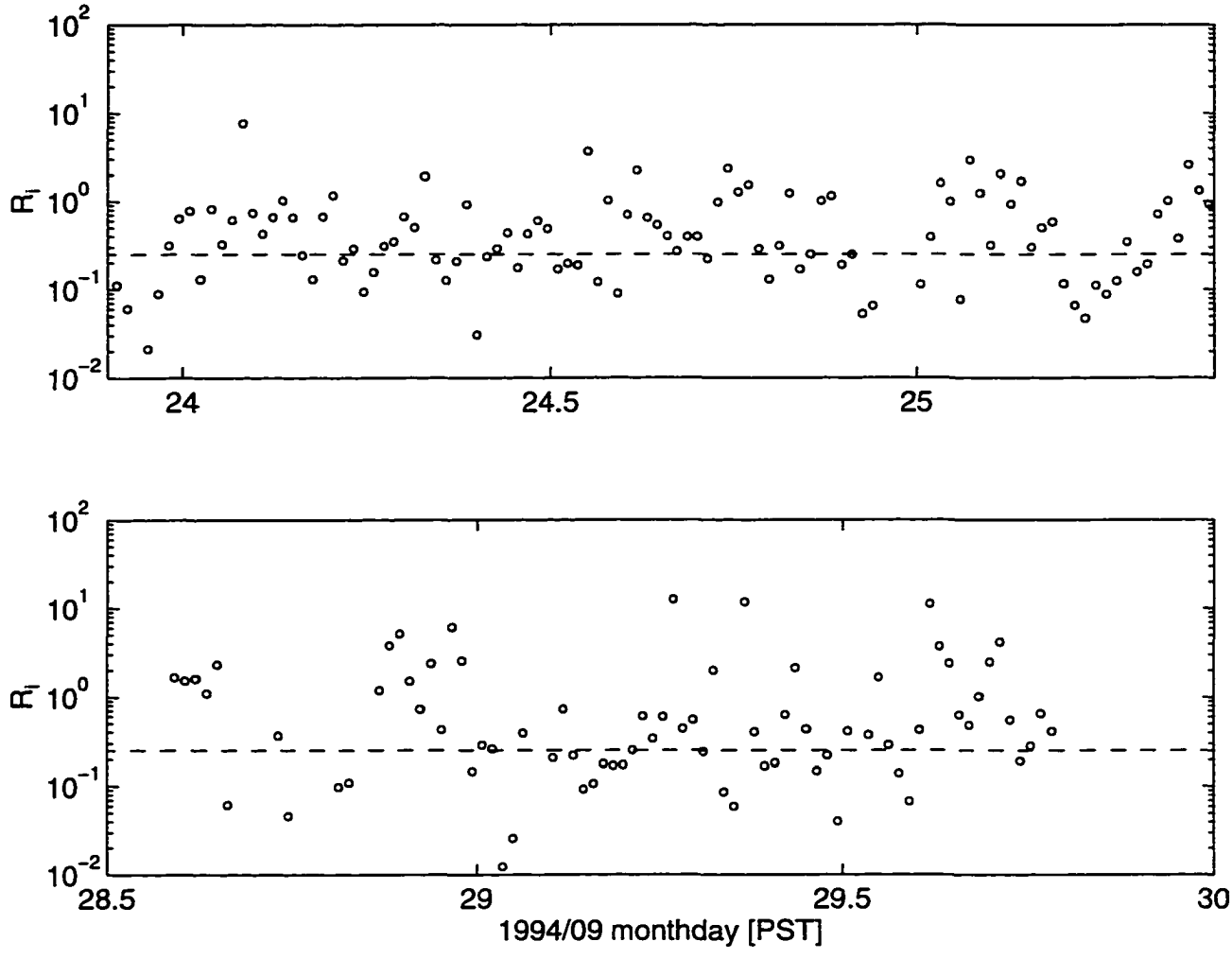

Figure 2.5: Estimates of the gradient Richardson number (R_i) at mid-depth using N^2 measured with TAMI, and shear measured with the ADCP. Each open circle represents a 20-min mean.

above the bottom can be identified. The height of this mixed layer varied with tidal flow, and reached mid-depth during strong flows. During slack current the mixed layer was not evident, and the whole water column was stratified. A sharp density gradient occured above the bottom mixed layer, and unstable overturns were observed during the ebb.

CTDs on the moored instrument TAMI provided estimates of density difference over a vertical distance of 3 m at mid-depth. The buoyancy frequency squared, N^2, was derived from the density gradient. No shear estimates were available at the site of

TAMI. Estimates of the gradient Richardson number, Ri, were calculated by dividing the estimates of N^2 from TAMI, and the shear squared from the ADCP averaged over 3 m at mid-depth. Note that TAMI and the ADCP were apart by about 50 and 100 m during the first and second deployments, respectively. A total of 3.2 days of Ri, each value representing a 20-min mean, were obtained. The time series of Ri (Fig. 2.5) did not show a clear tidal variation. During the flood, 66% (31%) of the Ri values were greater (less) than 1/4, and 3% were negative (indicating overturns). During the ebb, 56% (34%) of the Ri values were greater (less) than 1/4, and 10% were negative. Hence, at mid-depth, the water column was stable more often than it was unstable during the flood, whereas the chances of shear stability and instability were roughly equal during the ebb. The frequency of occurrence of $Ri < 1/4$ must increase towards the bottom due to the combined effects of increasing shear and decreasing stratification.

2.3 Deployment of the ADCP

The ADCP was deployed by mounting it in a metal quadripod sitting on the sea floor. The tilt sensors of the ADCP measured heading, pitch, and roll angles with 0.01° resolution, and the readings remained steady throughout the experiment because the instrument was rigidly mounted. The metal stand, however, distorted the magnetic field, and the true heading angle was determined through a post-experimental calibration. A shore cable 800 m long connected the ADCP to the power supply and a computer in the shore station, and the data were directly transfered to the computer via the cable.

About 4.5 days of data were collected with the standard working mode (mode 4) of the ADCP, among which 3.8 days of data were recorded at rapid sampling rates (Fig. 2.2). The profiling range was broken up into uniform segments (depth cells) with 1 m vertical spacing. Because of the metal stand's size and a 1.5 m blanking

distance in transmitting acoustic echoes, the center of the first velocity cell was 3.6 m high. Limited by the side lobes reflected from the surface, the uppermost cell was centered at 27.6 m height. The ADCP pinged at the fastest rate possible, about 0.75 s per ping or at a frequency of 1.3 Hz. The velocity was recorded in beam coordinates, and the number of pings, that averaged into ensembles by the ADCP, ranged from 2 to 4.

Prior to the Cordova Channel experiment, an *in situ* test of the instrument was conducted to obtain estimates of the noise levels of the ADCP. Velocity data were collected by mounting the ADCP on a boat drifting in the almost slack water of Saanich Inlet. The signal associated with the motion of the boat was removed by subtracting a second-order polynomial fit from each along-beam velocity profile, and the remaining signals are taken as Doppler noise. Fig. 2.6 shows that the noise standard deviation of the beam velocity is 0.01-0.015 m s^{-1} up to a profiling range of 40 m, for 4-ping averaged ensembles with 1 m cell size. Assuming that the consecutive pings are uncorrelated then the single-ping standard deviation is 0.02-0.03 m s^{-1}, which is close to the value claimed by the manufacturer.

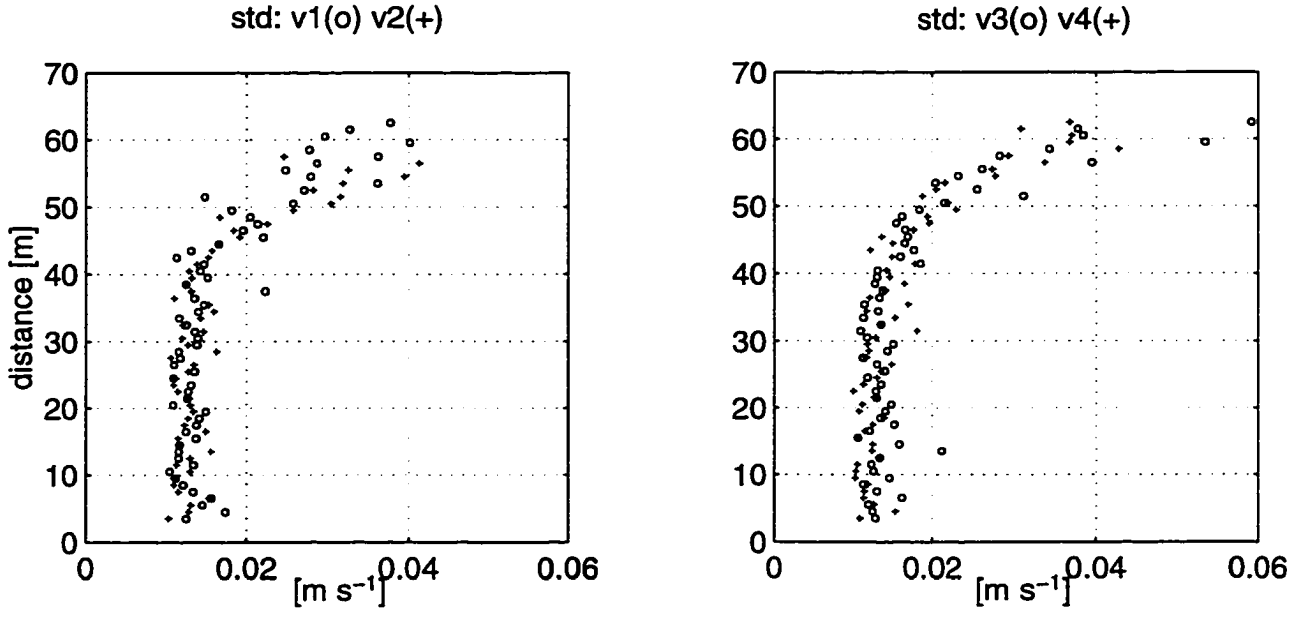

Figure 2.6: Standard deviation of the 4-ping averaged, 1-m cell size velocities along the four-beams, and its variation with the distance from the transducer. The data was collected from a test in an inlet with almost slack water.

Chapter 3

Mean Flow and Shear Estimates

3.1 Introduction

In this chapter we study the use of an ADCP in a turbulent flow to estimate mean velocity and shear profiles and examine the bias and statistical uncertainty of these estimates. We shall also describe the space-time variations of mean flow and shear in Cordova Channel which provide the background for the forthcoming chapters.

Accurate estimates of mean velocity and shear are essential for a study of the flow structure, e.g., resolving the log-layer and deriving parameters of the turbulence such as the shear production and gradient Richardson number. However, there is a significant difference between the measurement principle of an ADCP and that of a current meter. A current meter measures the "instantaneous" velocity vector at its position. For an ADCP, the directly measured velocities are the radial speed of the flow along its inclined acoustic beams, and the "true" velocity vector is derived from these along-beam velocities. The derivation assumes that the flow is homogeneous in the horizontal plane over the distances separating the beams (e.g., Lohrmann et al., 1990). At best, this assumption holds only statistically in a turbulent environment, and only the time-mean velocity vector can be derived. A test of statistical homogeneity is required to justify its assumption and to determine the bias of the estimated mean velocity vector. Flows that have a Reynolds stress are anisotropic, and the variances of the velocity along the beams are different and cannot be used to test statistical homogeneity. A comparison of the "error" velocity against either the horizontal or vertical velocity provides a test for statistical homogeneity in the

horizontal plane. Because the vertical and error velocities are small compared to the horizontal current, their measurement requires careful attention to bias in the tilt sensors, platform motions and turbulent fluctuations.

3.2 Deriving velocity vector from along-beam velocities

a. Calculation algorithm

For the beam configuration of an upward-looking ADCP (Fig. 3.7), we use $\varphi_1, \varphi_2, \varphi_3$ to represent the heading, pitch and roll angles, respectively. We denote the velocity along the ith (i =1, ..., 4) beam by b_i, and the horizontal and vertical components at the position of b_i by u_i, v_i, w_i. For small pitch and roll angles, correct to the first order in φ_2 and φ_3, the relationship between b_i and u_i, v_i, w_i is (Lohrmann et al., 1990)

$$\begin{aligned} b_1 &= -u_1(\sin\theta + \varphi_3\cos\theta) - w_1(\cos\theta - \varphi_3\sin\theta) + v_1\varphi_2\cos\theta \\ b_2 &= u_2(\sin\theta - \varphi_3\cos\theta) - w_2(\cos\theta + \varphi_3\sin\theta) + v_2\varphi_2\cos\theta \\ b_3 &= -v_3(\sin\theta - \varphi_2\cos\theta) - w_3(\cos\theta + \varphi_2\sin\theta) - u_3\varphi_3\cos\theta \\ b_4 &= v_4(\sin\theta + \varphi_2\cos\theta) - w_4(\cos\theta - \varphi_2\sin\theta) - u_4\varphi_3\cos\theta, \end{aligned} \tag{3.1}$$

where $\theta = 30°$ is the beam inclination angle with respect to the centerline of the ADCP, and the rotation with the heading angle φ_1 should be added in (3.1) when u_i and v_i are defined as the eastward and northward components, respectively.

The along-beam velocities b_i are directly measured by the ADCP. When the ADCP operates in the "earth coordinates" mode, the beam velocities are transformed to the "velocity vector" and the "error" velocity by

$$\begin{aligned} \hat{u} &= \frac{b_2 - b_1}{2\sin\theta} - \varphi_3\frac{b_1 + b_2}{2\cos\theta} \\ \hat{v} &= \frac{b_4 - b_3}{2\sin\theta} + \varphi_2\frac{b_3 + b_4}{2\cos\theta} \\ \hat{w} &= -\frac{b_1 + b_2 + b_3 + b_4}{4\cos\theta} - \varphi_3\frac{b_2 - b_1}{2\sin\theta} + \varphi_2\frac{b_4 - b_3}{2\sin\theta} \end{aligned} \tag{3.2}$$

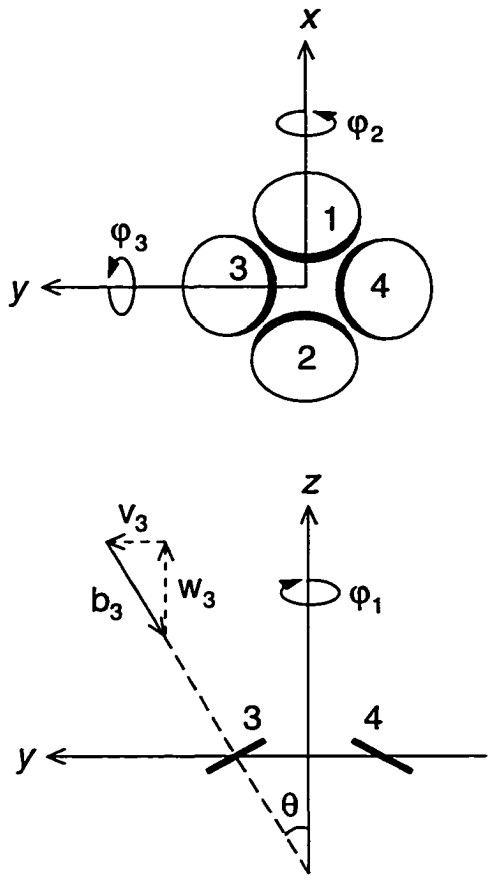

Figure 3.7: Transducer geometry and beam orientation of the ADCP. The beams are nominally inclined by $\theta = 30°$ from the vertical. φ_1,φ_2 and φ_3 are heading, pitch and roll angles.

$$\hat{e} = -\frac{(b_1 + b_2) - (b_3 + b_4)}{4\cos\theta}$$

and an additional compass rotation. The next subsection shows that $u, \hat{v}, \hat{w}$ can not be regarded as a true velocity vector for a single ping.

b. The assumption of homogeneity

From (3.1) and (3.2), the relationship between $\hat{u}, \hat{v}, \hat{w}, \hat{e}$ and u_i, v_i, w_i, correct to the first order in φ_2 and φ_3, can be derived to read

$$\begin{aligned}
\hat{u} &= \frac{u_1 + u_2}{2} - \frac{w_2 - w_1}{2\tan\theta} - \varphi_3\frac{u_2 - u_1}{\sin 2\theta} + \varphi_2\frac{v_2 - v_1}{2\tan\theta} \\
\hat{v} &= \frac{v_3 + v_4}{2} - \frac{w_4 - w_3}{2\tan\theta} + \varphi_2\frac{v_4 - v_3}{\sin 2\theta} - \varphi_3\frac{u_4 - u_3}{2\tan\theta} \\
\hat{w} &= \frac{w_1 + w_2 + w_3 + w_4}{4} - \frac{(u_2 - u_1) + (v_4 - v_3)}{4}\tan\theta \\
&\quad + \varphi_3\frac{(u_3 + u_4) - (u_1 + u_2)}{4} - \varphi_2\frac{(v_3 + v_4) - (v_1 + v_2)}{4} \\
&\quad + (\varphi_3\frac{w_2 - w_1}{2} - \varphi_2\frac{w_4 - w_3}{2})\frac{1 + \cos^2\theta}{\sin 2\theta} \\
\hat{e} &= \frac{(w_1 + w_2) - (w_3 + w_4)}{4} - \frac{(u_2 - u_1) - (v_4 - v_3)}{4}\tan\theta \\
&\quad + \varphi_3\frac{(u_1 + u_2) - (u_3 + u_4)}{4} - \varphi_2\frac{(v_1 + v_2) - (v_3 + v_4)}{4} \\
&\quad + (\varphi_3\frac{w_2 - w_1}{4} + \varphi_2\frac{w_4 - w_3}{4})\tan\theta.
\end{aligned} \tag{3.3}$$

For $\hat{u}, \hat{v}, \hat{w}$ to form a true velocity vector, each velocity component at different beams must be identical, i.e., the velocity field must be instantaneously homogeneous in the horizontal plane over the distances separating the beams. In a turbulent flow, this requirement is not satisfied if eddies exist with scales comparable to and smaller than the beam separation. We may assume, however, that the statistical properties of the flow are horizontally homogeneous. In particular, we assume that the mean flow components, denoted by $\bar{u}, \bar{v}, \bar{w}$, are horizontally homogeneous over the spatial domain of the beams and that the fluctuations average to zero. Then from (3.3), we

have

$$\begin{aligned} \bar{u} &= \overline{\hat{u}} \\ \bar{v} &= \overline{\hat{v}} \\ \bar{w} &= \overline{\hat{w}} \\ \bar{e} &= \overline{\hat{e}} = 0. \end{aligned} \tag{3.4}$$

We note that, under the assumption of statistical homogeneity, the expected error velocity $\bar{\hat{e}}$ is zero. In fact, a comparison of the magnitudes of $\bar{\hat{e}}$ against the magnitude of the vertical (or horizontal) velocity provides the only explicit test of the assumption of homogeneity. For example, the estimated mean vertical flow $\bar{w}$ is unreliable if its magnitude is not significantly larger than that of $\bar{\hat{e}}$.

The amount of averaging required to give a satisfactory estimate of the mean velocity vector depends upon the distribution of eddy scales and the energy of the eddies. For example, if all eddies have scales much larger than the beam separations, then the field *is* instantaneously homogeneous, and the statistical uncertainty of the estimates of the mean is determined solely by the probability distribution of the fluctuations and the degrees of freedom in the estimate. For such eddies, the vertical velocity must be small compared to the horizontal components owing to its bottom boundary condition. The most intense vertical velocities will come from eddies with scales comparable to the distance of these eddies above the bottom, which is similar to the distance separating the pairs of beams. The averaging will have to span many such eddies which is realized with an averaging time $\tau \gg L/U$, where L is the beam separation and U is the mean speed. The relevant parameter is $N = U\tau/L$, the ratio of horizontal averaging scale to the beam separation.

c. Rigid v. non-rigid deployments

In practical deployments, an ADCP can be mounted either rigidly or non-rigidly. For a rigidly mounted ADCP, the tilt angles $\varphi_i (i = 1, 2, 3)$ are constant, and the mean velocity components are the linear combinations of the averaged beam velocities:

$$\begin{aligned} \bar{\hat{u}} &= \frac{\bar{b}_2 - \bar{b}_1}{2\sin\theta} - \varphi_3 \frac{\bar{b}_1 + \bar{b}_2}{2\cos\theta} \\ \bar{\hat{v}} &= \frac{\bar{b}_4 - \bar{b}_3}{2\sin\theta} + \varphi_2 \frac{\bar{b}_3 + \bar{b}_4}{2\cos\theta} \\ \bar{\hat{w}} &= -\frac{\bar{b}_1 + \bar{b}_2 + \bar{b}_3 + \bar{b}_4}{4\cos\theta} - \varphi_3 \frac{\bar{b}_2 - \bar{b}_1}{2\sin\theta} + \varphi_2 \frac{\bar{b}_4 - \bar{b}_3}{2\sin\theta} \\ \bar{\hat{e}} &= -\frac{(\bar{b}_1 + \bar{b}_2) - (\bar{b}_3 + \bar{b}_4)}{4\cos\theta}. \end{aligned} \tag{3.5}$$

For a non-rigidly mounted instrument, there are changes in the transducer orientation (reflected by the variations in tilt angles) and translational movements of the instrument (which are not monitored). Changes in beam orientation lead to changes of velocity along each beam even in a steady flow field, hence averaging a beam velocity time series is meaningless. Instead of using (3.5), the transformation from beam velocity to "velocity vector" must be done ping by ping using (3.2), and then taking the average of $\hat{u}, \hat{v}, \hat{w}$ to derive the mean velocity components.

Would the motions of a non-rigidly mounted instrument influence the mean velocity estimates? Translational motions bias the Doppler shift of individual samples but not the estimated mean velocity. For the estimated mean velocity, as can be seen from (3.3), the contributions of zero-mean translational motions either cancel identically (e.g., the term $\varphi_3(u_2 - u_1)$ in the first line of (3.3)) or vanish through averaging (e.g., the term $u_1 + u_2$). Variations in tilt angles, however, may correlate with velocity variations (e.g. the term $\overline{\varphi_3'(u_2' - u_1')}$) and bias the velocity estimates. For eddies with a very large spatial scale compared to the beam separation, $\overline{\varphi_3'(u_2' - u_1')} = 0$ because the correlations cancel identically. For eddies with a very small scale compared to the beam separation, the correlation at points 1 and 2 will be small, and the velocity fluctuations at either point are unlikely to correlate with the tilt of the instrument.

Intermediate scale eddies, those with scales comparable to the beam separation, may well have fluctuations of velocity difference $(u_2' - u_1')$ correlated with tilting motions. A 2° rms tilt angle fluctuation and a 0.1 m s^{-1} rms velocity fluctuation difference would produce a bias of 4×10^{-3} m s^{-1} if the two fluctuations are perfectly correlated. Hence this effect is not likely to be important for the estimated horizontal current, but may be significant for the estimated mean vertical velocity which has a typical magnitude of 0.01 m s^{-1}.

Bias in the tilt sensors introduces another difficulty for a non-rigidly mounted ADCP. Inaccuracy in the measurement of φ_2 or φ_3, as can be seen from (3.2), can contaminate the transformation from beam velocity to "velocity vector." Again, the bias is of little practical consequence for the horizontal velocity estimates but will affect the estimated vertical velocity. To eliminate this contamination, one needs to determine the bias in tilt angles and recalculate the beam-to-earth coordinate transformation. The re-processing of data can be conducted, using (3.2), if data are recorded ping by ping. If only the ensemble-average of a large number of pings are recorded (which is usually the case), the estimates can still be corrected for tilt-angle bias using (3.5). This correction can only be done if the instrument is rigidly mounted, because the horizontal direction of the plane of tilt can rotate during the averaging interval for a non-rigidly mounted instrument.

Thus, for a non-rigidly mounted instrument, the variances of the measured vertical and error velocities will be large and an explicit test of the assumption of statistical homogeneity will be more difficult. More significantly, a rigidly mounted ADCP permits the estimation of turbulent quantities with the "variance method," whereas this is impossible with a non-rigidly mounted instrument.

3.3 Analysis of data from a rigidly mounted ADCP

a. Correction of tilt angle bias

The measured values of φ_2 and φ_3 are 0.00° and −3.00°, respectively, throughout the experiment. However, the vertical velocity calculated with these tilt angles has a tidally varying signal (Fig. 3.8, thin lines). This signal must be a contamination from the horizontal velocity because it greatly exceeds the vertical velocity attributable to the tide. By choosing combinations of different values of φ_2 and φ_3, we found that the vertical velocity bias is minimized by changing only the roll angle from −3.0° to −2.0° (thick lines, Fig. 3.8). Hence the values of $\varphi_1, \varphi_2, \varphi_3$ used in the transformation from beam to earth coordinates are 150.3°, 0.0°, −2.0°, respectively.

b. Measurement uncertainties

Fig. 3.9 shows a sample of a 1-day long, 4-ping averaged beam velocity at mid-depth from beam 1, which is projected into the downstream direction during ebb tide. (The flow is southward during the ebb and northward during the flood.) The low- and high-frequency variations are separated with a zero-phase, low-pass and 4th order Butterworth filter with a cut-off period of 20 min. The measured velocity contains uncertainties due to both Doppler noise and turbulence. The standard deviation of the beam velocity noise, for 4-ping averaged ensembles with 1 m bin size, was estimated to be 0.01 to 0.015 m s^{-1} (Chapter 2). Hence the influence of Doppler noise is only significant during the weak flood between day 24.6 and 24.8. During the other segments of this 1-day long data, the high-frequency beam velocity fluctuations are dominated by turbulence.

Velocity variations due to Doppler noise are uncorrelated, hence, by averaging N ensembles, the noise standard deviation is reduced by a factor of $N^{1/2}$. For 20-min averages, the uncertainty in beam velocity due to Doppler noise is 5 to 7 $\times 10^{-4}$ m s^{-1}.

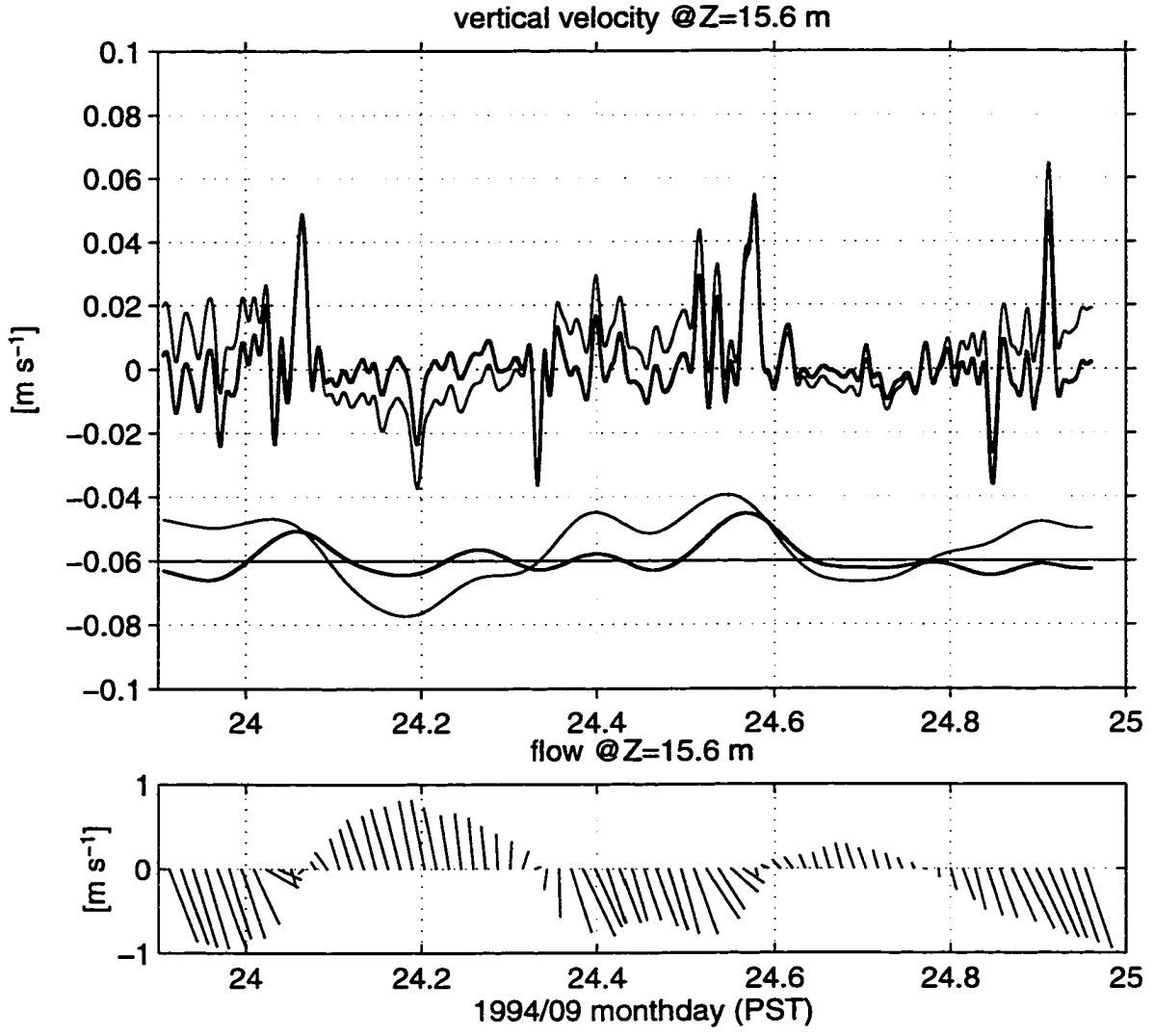

Figure 3.8: One-day long vertical velocity at mid-depth (z=15.6 m), calculated for roll angle $\varphi_3 = -2°$ (thick lines) and $\varphi_3 = -3°$ (thin lines). The two upper curves are calculated from 20-min smoothed beam velocities and the lower curves are 3-h smoothed. The lower panel is a stick diagram of the horizontal flow at mid-depth.

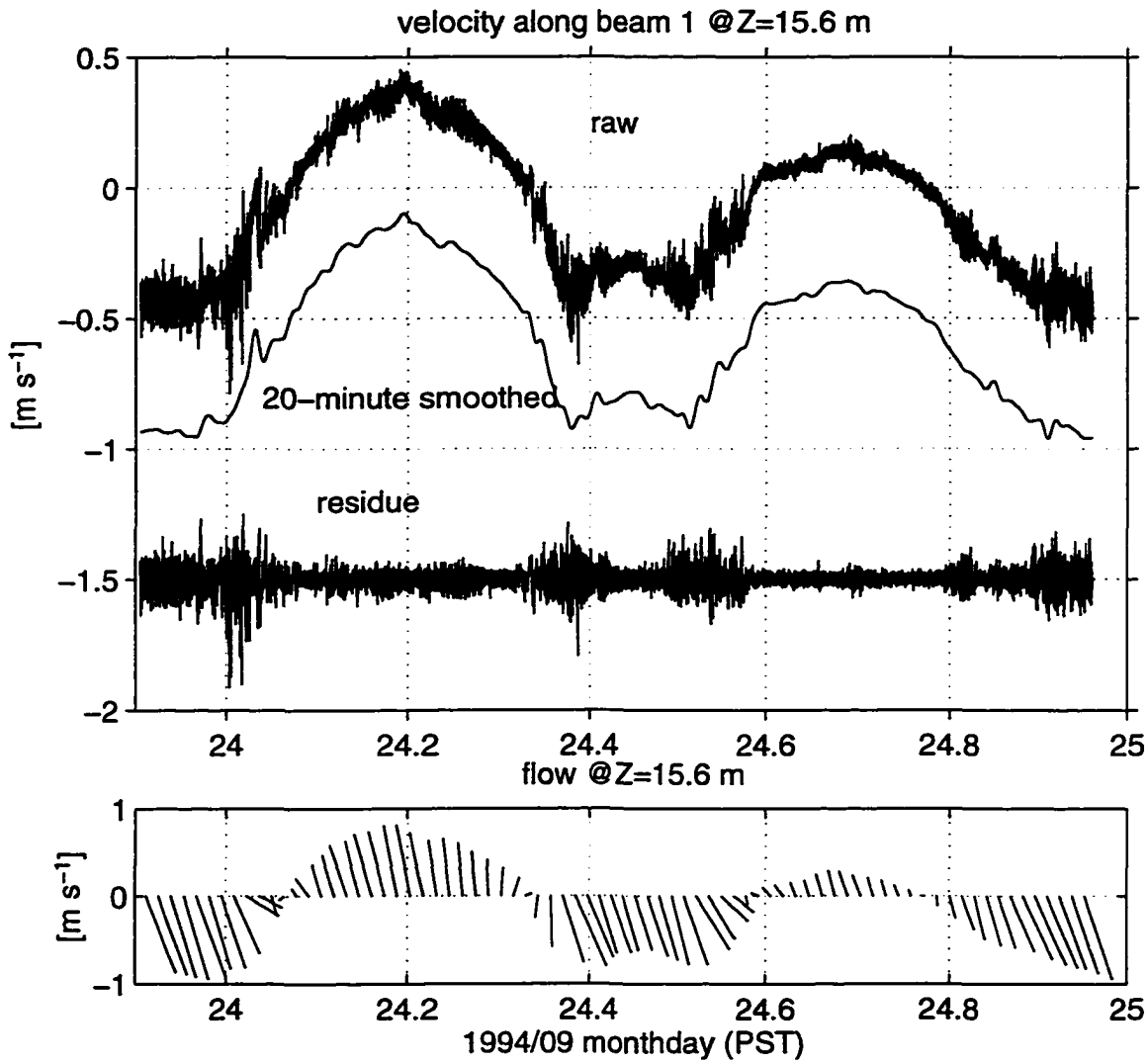

Figure 3.9: Sample of 1-day velocity data at mid-depth (z=15.6 m) from the beam oriented in the downstream direction during ebb tide. The sampling interval is 3.05 s and each sample is the average of 4 pings. The 20-min smoothed velocity and the residual high-frequency component are plotted. The stick diagram in the lower panel is the 20-min mean horizontal velocity at mid-depth.

Turbulent fluctuations, however, are not fully uncorrelated. In order to determine how much the statistical uncertainty is reduced by time averaging, we need to know the de-correlation time scale of the turbulent fluctuations. The auto-correlation functions (acf) of beam velocity fluctuations for two 20-min intervals, one during strong ebb and one during weak flood, are shown in Fig. 3.10. During the strong ebb, both at mid-depth and near bottom (Figs. 3.10a, b), the acf's are unlike those for white noise. By comparison, the acf's of the velocity fluctuations during the weak flood look more like those for white noise (Figs. 3.10c, d), possibly because the Doppler noise is comparable to the turbulent intensity during this interval.

We define the de-correlation time scale as the lag at which the acf is reduced to the upper band of its uncertainty level (0.1). From an examination of all beams and various phases of the tide, we find that 15 s is the typical de-correlation time during strong flow. Thus, a 20-min average has 80 degrees of freedom and the standard deviation of the estimated mean along-beam velocity is typically 5.5×10^{-3} m s^{-1} during strong flow. During the weak flood between day 24.6 and 24.8, the standard deviation of the 20-min mean is 1.7×10^{-3} m s^{-1} and still larger than the Doppler noise.

By including terms representing the uncertainty in the mean beam velocity in (3.5), we deduce that the standard deviations of the horizontal and vertical velocity components are $\sqrt{2}$ times larger and $\sqrt{3}$ times smaller, respectively, than that of the beam velocity. Thus, the uncertainty due to turbulence of the 20-min mean velocities is typically about 8×10^{-3} m s^{-1} for $\bar{u}, \bar{v}$ and 3×10^{-3} m s^{-1} for $\bar{w}$ at strong flow, and the level of uncertainty during the weak flood between day 24.6 and 24.8 is three times smaller.

The acf's do not always fall to zero at very long lags (Fig. 3.10), which indicates the presence of eddies with large scales. We have also noticed some distinct events lasting up to 100 s during the turning of the flow direction. Furthermore, Fig. 3.9

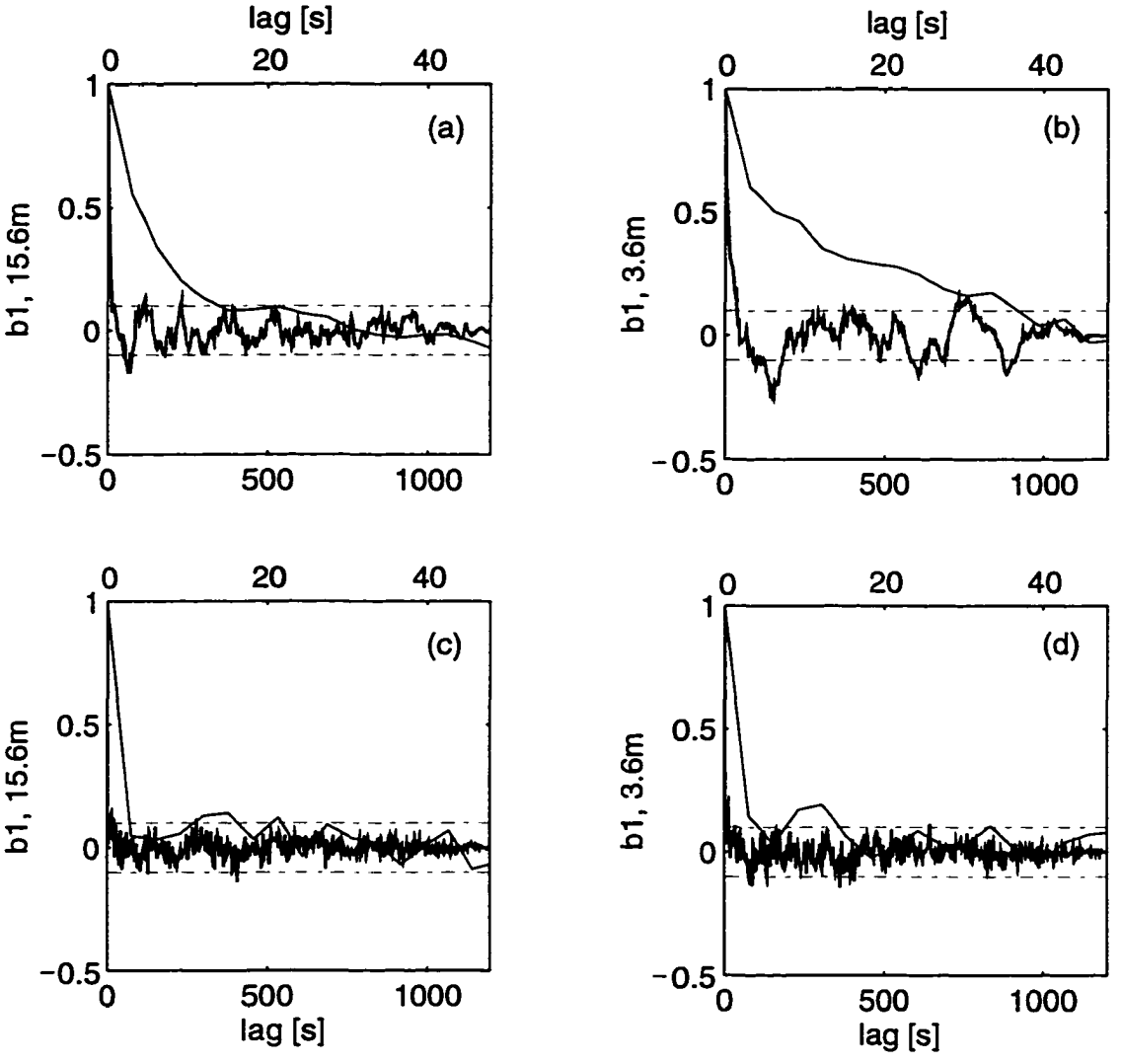

Figure 3.10: Auto-correlation coefficients as functions of lag for the high-pass beam velocities along beam 1 at 15.6 m and 3.6 m above the seabed. (a) and (b) are from 20-min data taken during the strong ebb starting at day 23.91; (c) and (d) are from the 20-min data taken during the weak flood starting at day 24.6. Note that two different scales of lag are used in each panel.

shows that a smoothing of beam velocity at the 20-min cutoff period not only keeps the tidal signal, but some eddy fluctuations with periods longer than 20 min as well.

c. The choice of averaging period and test of homogeneity

For unsteady tidal flow, the choice of an appropriate averaging time is usually hard to make. This is because the "spectral gap" separating turbulence from the tidal fluctuations is "something which *a priori* may not be known to exist or physically needs to exist" (Gross and Nowell 1983). A compromise is always needed in choosing between an averaging time short enough to retain tidal variations and one that is long enough to reduce the fluctuations induced by turbulent eddies. For measurements using the ADCP, there is another constraint; the test of statistical homogeneity may also require considerable averaging.

The above analyses show that a 20-min averaging period reduces the rms velocity fluctuations to low levels compared to the mean velocity magnitude. The major tidal components in Cordova Channel are semi-diurnal and diurnal constituents, and 20-min averages resolve approximately 10° phase changes for the semi-diurnal tide and about 5° for the diurnal tide, respectively. Fig. 3.11a compares the 20-min vertical velocity $\overline{w}$ and the error velocity $\overline{\hat{e}}$ at three depths. The magnitude of $\overline{\hat{e}}$ increases with increasing height. At the lowest level, $\overline{\hat{e}}$ is generally smaller than $\overline{w}$. At mid-depth, $\overline{\hat{e}}$ is relatively small during most of the strong vertical flow events. At the uppermost level, the error velocity is frequently large except for the event shortly before day 24.6. The ratio of the horizontal averaging scale to the beam separation, defined as $N = U\tau/L$ in section 2.b, decreases with range and increases with current speed (Fig. 3.11b). For 20-min averages, N is 300–400 at the bottom cell, 40–70 at mid-depth, and 20-40 at the top cell.

The justification for the assumption of statistical homogeneity in the horizontal plane is that the error velocity (which has an expectation of zero) is small compared

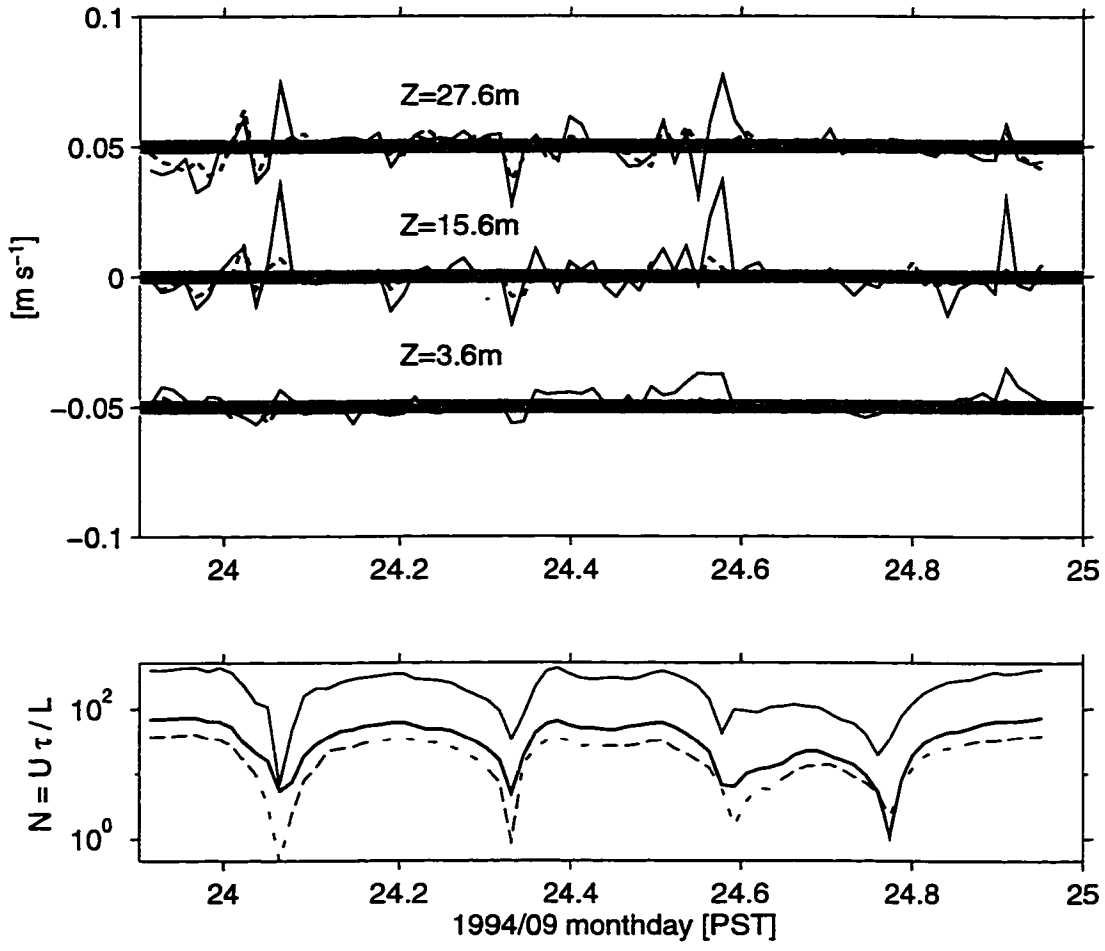

Figure 3.11: Upper panel: 20-min mean vertical (solid lines) and error velocities (dashed lines) at the heights of 15.6 m, 3.6 m (offset by -0.05 m s^{-1}) and 27.6 m (offset by 0.05 m s^{-1}). The sign of the error velocity is made identical to the sign of the vertical velocity to facilitate comparison. The shading spans ± 1 standard deviation of 3×10^{-3} m s^{-1}. Lower panel: The ratio of horizontal averaging length to beam separation at 3.6 m (thinner solid line), 15.6 m (thicker solid line) and 27.6 m (dashed line), respectively.

to the velocity component of interest. The standard deviation of a 20-min average of horizontal velocity due to turbulence and Doppler noise is typically 8×10^{-3} m s^{-1} (section 3.2c) or about 1%. Thus, we would like the error velocity to be at least 100 times smaller than the horizontal velocity estimate. A scatter plot of $|\overline{U}/\overline{\tilde{e}}|$ against N, the ratio of horizontal averaging length to beam separation, indicates that most samples have a ratio exceeding 100 (Fig. 3.12a). Nearly all ratios smaller than 100 come from $N < 50$. Can N be used to predict the likelihood of having the error velocity below a given threshold? The fraction of samples that exceed our threshold of $|\overline{U}/\overline{\tilde{e}}| = 100$ increases rapidly with increasing non-dimensional averaging length N, and passes 95% at $N = 55$ (Fig. 3.12b). Thus, averaging over more than 55 beam separations produces error velocities small enough to be consistent with the assumption of horizontal statistical homogeneity. A few 20-min averages have N larger than 300 but still have velocity ratios smaller than 100 which may be a statistical artifact. However, horizontal eddies were visually observed and, if such eddies had passed near the ADCP, the flow field would have been inhomogeneous and the error velocity large.

Although the standard deviation of the vertical velocity due to turbulence and Doppler noise is only typically 3×10^{-3} m s^{-1}, the mean and variance of this component are small compared to horizontal velocity, and the above threshold of 100:1 is unrealistic. The distribution of the mean vertical-to-error velocity ratio (Fig. 3.13a) indicates that many samples do not even exceed a ratio of 3. For this analysis, we ignored all samples with vertical velocities smaller than 3×10^{-3} m s^{-1}. The number of samples exceeding the threshold of 3 increases slowly with N and reaches 75% at $N = 90$ (Fig. 3.13b). Thus, for many 20-min averages, the estimated vertical velocity is not distinguishable from the error velocity and, therefore, it is indistinguishable from zero. This is true even when the magnitude of the vertical velocity greatly exceeds its standard deviation of 3×10^{-3} m s^{-1} determined from beam statistics. Unlike the

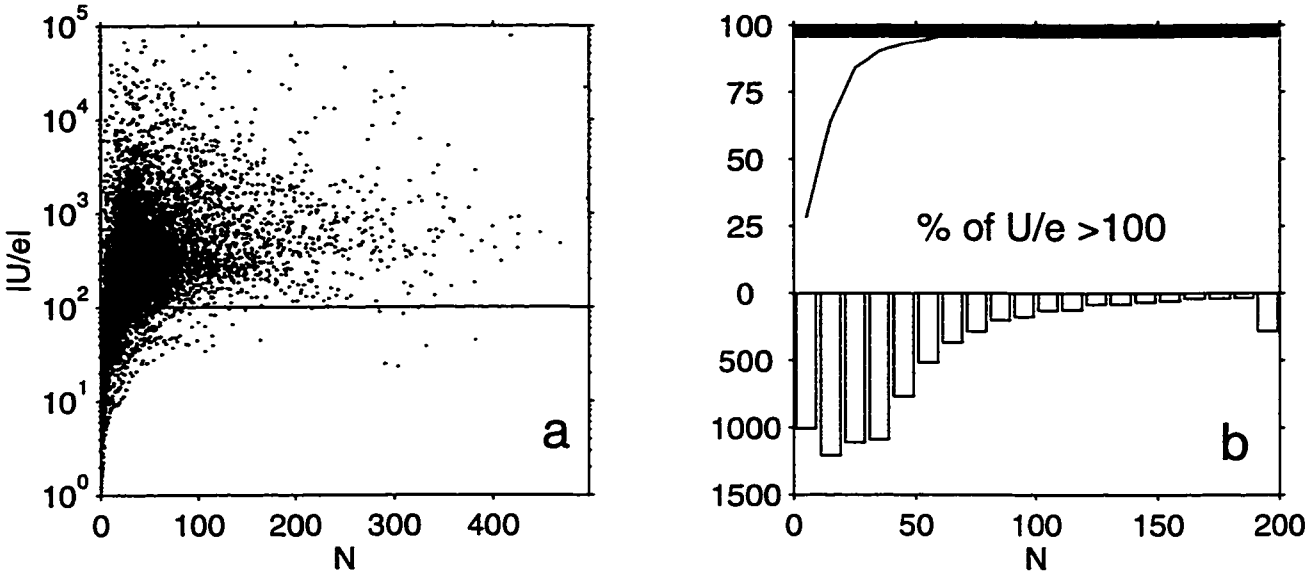

Figure 3.12: (a) A scatter plot of the magnitude of the ratio of horizontal to error velocity versus non-dimensional averaging length N. (b) Upper panel: The percentage of samples with velocity ratios exceeding 100 as a function of N. The 95 to 100% range is shaded. Lower panel: histogram of N.

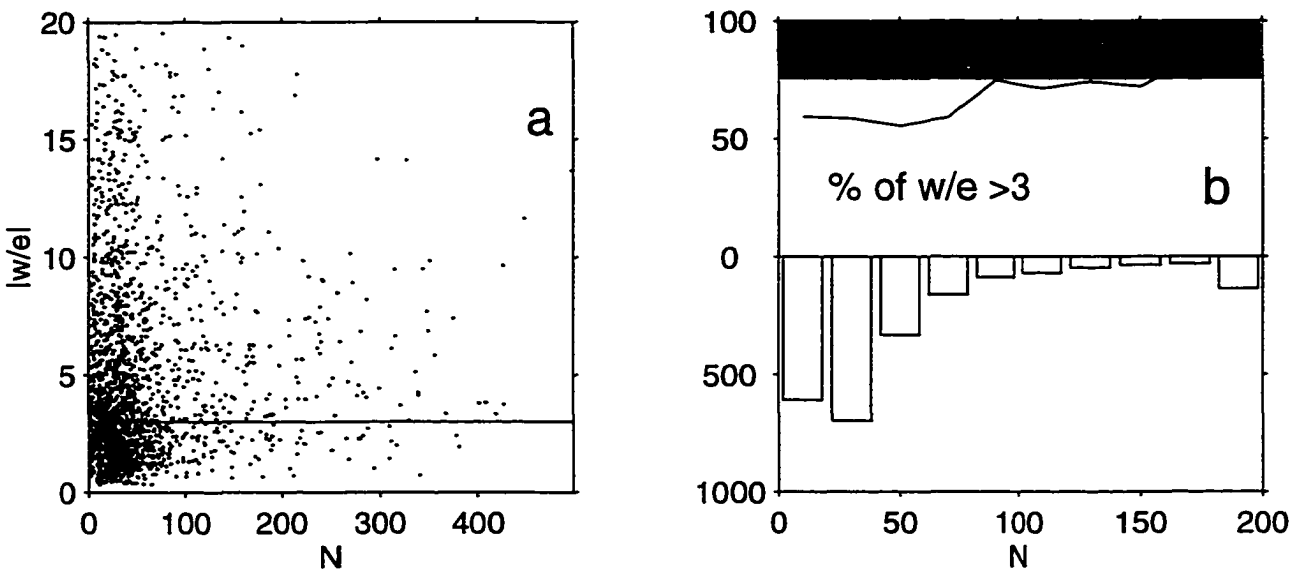

Figure 3.13: Same as Fig. 3.12 except for vertical velocity and a velocity ratio of 3. The 75 to 100% range is shaded.

case for the horizontal velocity, the non-dimensional averaging length N is a poor indicator of when the vertical velocity samples pass a test for horizontal homogeneity.

3.4 Mean flow and shear estimates in Cordova Channel

a. Results

The 4.5 days of velocity data collected using mode 4 spanned over a period of 8 days. By choosing an averaging period of 20 min, we obtained a total of 306 mean velocity

profiles, each consisting of 25 depth cells. A harmonic fit, composed of the four major tidal constituents (M_2, S_2, K_1 and O_1) and the zero-frequency residue, explains more than 91% of the variances of the velocity time series at each cell. Thus, the flow in Cordova Channel during this experiment was mainly tidal.

The depth averaged velocities (for each 20-min average) are asymmetric with respect to the flood and ebb (Fig. 3.14). The ebb is stronger than the flood and their directions are not exactly opposite (they differed by 170°). The current direction difference between bottom and top layers is typically about 15°, both for flood and ebb. The veering with height during the flood (Fig. 3.15a) is in the same direction as for a bottom Ekman layer, but the backing during the ebb (Fig. 3.15b) is in the opposite sense. The vertical rotation of the shear (Figs. 3.15c, d) is about 90°, much larger than it is for the flow. At 3.6 m above the seabed, the directions of the shear and the flow are quite close during the flood, whereas the shear is about 30° counter-clockwise from the flow during the ebb (top panel, Fig. 3.15). The large transverse shear in the lower layer during the ebb provides a transverse stress directed offshore from the headland.

The direction of the depth-mean flow is unsteady. We define the streamwise s-direction to be aligned with the depth-mean flow, and make the streamwise velocity u_s positive during the flood and negative during the ebb. The transverse n-direction is normal to s and points away from the headland. Fig. 3.16 shows the depth-time sections of 1-day-long streamwise (u_s) and transverse (u_n) flow, their shears ($\partial u_s/\partial z, \partial u_n/\partial z$) and vertical velocity ($\bar{w}$). The uncertainty owing to turbulence in the mean shear estimate is 8×10^{-3} s^{-1}.

The streamwise flow (Fig. 3.16a) shows a strong tidal signal, with the flow in the lower layer diminished by bottom drag. The non-tidal variations can be strong enough to distort the tidal variations. For example, the strong ebb between days 24.3 and 24.6 has two peaks with weaker flow in between. The (slight) slanting of the

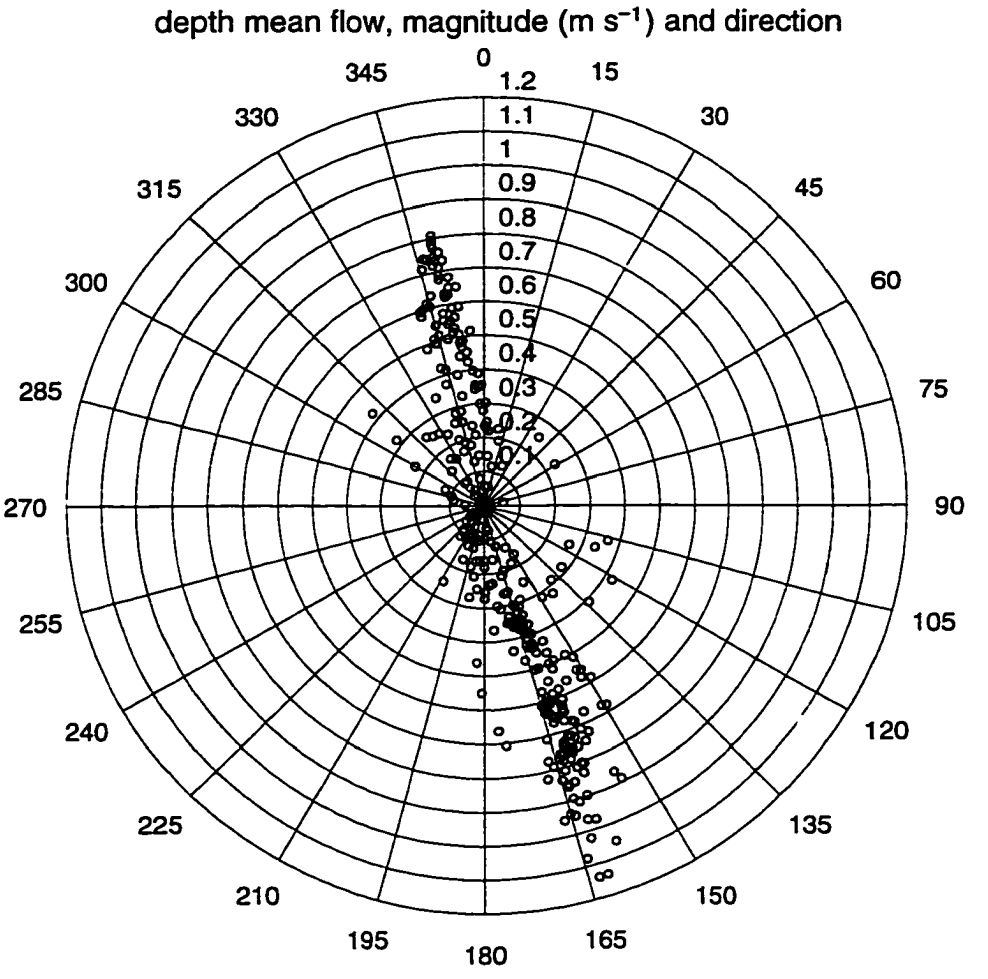

Figure 3.14: Polar coordinate diagrams of the depth mean flow for all 4.5 days of data.

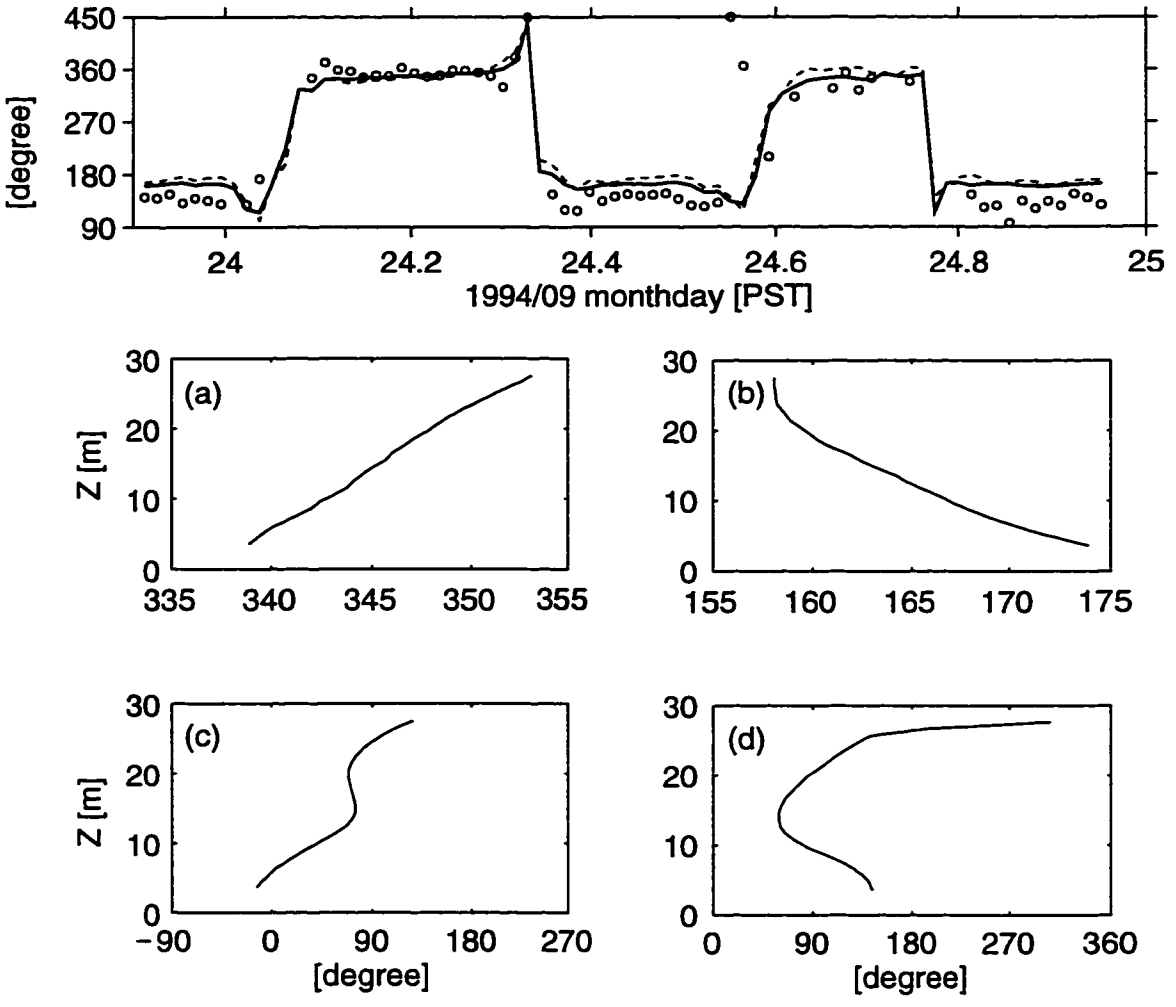

Figure 3.15: Upper panel: Time series of the direction of the 20-min mean velocity at 3.6 m (solid line) and 27.6 m (dashed line) and the shear at 3.6 m (circles). Lower panels: typical profiles of flow direction during flood (a) and ebb (b) and of the shear direction during the flood (c) and ebb (d).

isotachs indicates that the upper layer leads the lower layer in the decelerating stage, whereas it lags during the accelerating phase. The maximum speeds of streamwise flow are frequently found at heights below the uppermost bin.

The transverse flow is strongest in the near surface and near bottom layers, and weakest at mid-depth (Fig. 3.16b), with magnitudes reaching $O(0.15\ \mathrm{m\ s^{-1}})$ at the lowest cell during the ebb, and about $O(0.05\ \mathrm{m\ s^{-1}})$ in both the upper and the lower layers during the flood. The transverse flow is usually directed towards the headland in the lower layer, and in the opposite direction in the upper layer, with exceptions around the reversal of the tidal and the weak flood between days 24.6 and 24.8. The transverse velocity profiles usually vary linearly with height up to mid-depth but are more complex in the upper half of the water column. During the ebb near day 23.9 and between days 24.85 and 25, the transverse flow has a three-layer structure.

Both the streamwise and the transverse shear are bottom-enhanced (Figs. 3.16d, e). The streamwise shear reaches a magnitude of $O(0.05\ \mathrm{s^{-1}})$ in the lower layer, and contains a strong tidal signal. During the ebb, the transverse shear reaches about half the magnitude of the streamwise shear near the bottom, but it is small during the flood. The streamwise shear frequently reverses sign near mid-depth, corresponding to the occurrence of maximum velocity at that height. Reversals of the shear profile are also found in the transverse direction during the ebb when the transverse flow has three layers.

The mean vertical flow (Fig. 3.16c) is generally less than $0.02\ \mathrm{m\ s^{-1}}$ in magnitude but several significant up- and down-welling events can be identified with some occurring during flow turning and some during strong currents. These intensified vertical flow intervals generally occur over the entire profiling range, and the maximum velocity is at mid-depth, reaching $O(0.05\ \mathrm{m\ s^{-1}})$ at times. The comparison of vertical against error velocity shows that, at least at levels up to mid-depth, these events of vertical flow are real (Fig. 3.11). Note that an $O(0.05\ \mathrm{m\ s^{-1}})$ vertical flow lasting 20

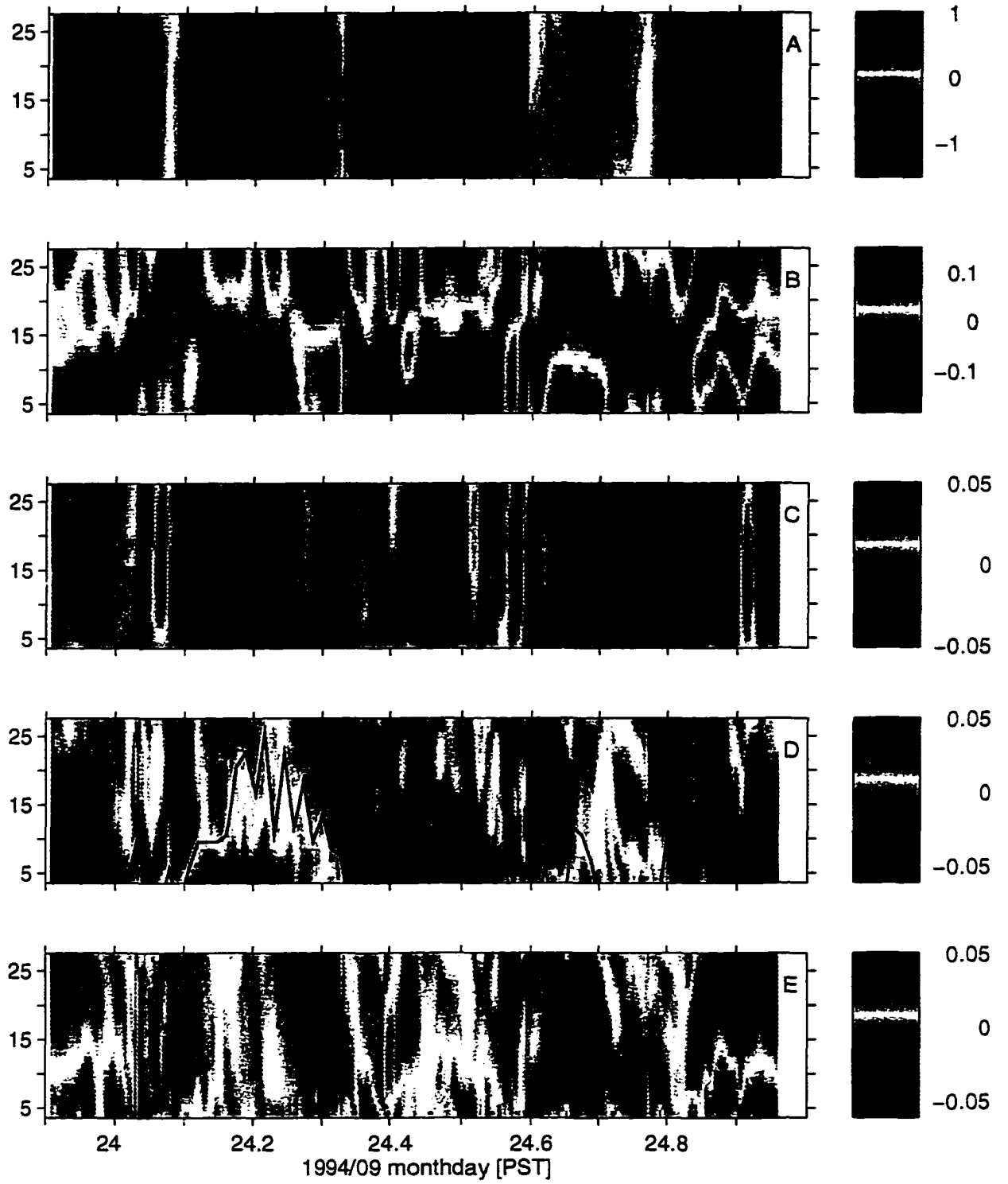

Figure 3.16: Cordova Channel depth-time sections of 20-min mean (a) streamwise, (b) transverse, and (c) vertical velocities (m s^{-1}); (d) streamwise shear (s^{-1}) and (e) transverse shear (s^{-1}). The solid line marks the log-layer height (m).

min is enough to bring the bottom water to the surface and vice versa, invoking a significant vertical exchange of water.

b. Discussions

The measurement results reveal a complicated picture of tidal flow in this natural channel. The occurrence of strong transverse flow can be attributed to the coastal curvature of the channel, especially the presence of a headland at the western side boundary (Fig. 2.1). The forms of transverse velocity profiles are derived theoretically by Kalkwijk and Booij (1986) as

$$u_{nc} = -\text{sign}(\bar{u}_s)\frac{fh}{\kappa^2} f_c(\frac{z}{h}, \alpha) \tag{3.6}$$

$$u_{nb} = 2\frac{|\bar{u}_s|h}{\kappa^2 R} f_b(\frac{z}{h}, \alpha), \tag{3.7}$$

where u_{nc} denotes the contribution from Coriolis forcing and u_{nb} from the effect of curvature (bending), f is the Coriolis parameter, h is water depth, R is the local radius of streamline curvature, $\bar{u}_s$ is the depth-mean of u_s and $\alpha = C_D^{1/2}/\kappa$ (C_D is the bottom drag coefficient referred to the depth-mean flow and $\kappa = 0.4$ is von Kármán's constant). The two profile functions, f_c and f_b, are nearly linear in z except very close to bottom. In deriving (3.6) and (3.7), Kalkwijk and Booij assumed that a log-layer exists in the streamwise direction and extends to the surface. A log-layer extending to large heights above the seabed has not been convincingly observed in previous work. The streamwise velocity in Cordova Channel, however, has been accurately fitted to the logarithmic form to heights of over 20 m during peak flows (Chapter 5), and this analysis gives $C_D = 4 \times 10^{-3}$ with respect to the depth-mean flow. Hence, $\alpha \approx 0.15$. The functions f_c and f_b are both $O(0.5)$ in the near-surface and bottom layers. Using typical values of f, h and $\bar{u}_s$ in Cordova Channel, (3.6) predicts a transverse flow of only $u_{nc} \approx 0.01$ m s^{-1}. Thus, the Coriolis force makes only a small contribution to the transverse flow and the predicted direction is opposite to the observed direction during

the ebb. To reproduce the correct magnitude of u_n, which is approximately 0.05 and 0.15 m s^{-1} during the flood and ebb, respectively, one requires a radius of curvature of 4 and 1.5 km. Both radii are reasonable considering the topography of the channel near the ADCP. The headland and Saanichton Bay provide an expansion/contraction that is asymmetric in the cross-channel direction (Fig. 2.1). During the ebb, the water must turn sharply around the headland while passing the ADCP. During the flood, the flow curvature is weaker because the channel is fairly straight south of the ADCP and the flow can separate from the western shore just north of the ADCP.

The shear reversals may be due to the inertia of the oscillatory flow. However, the greater abundance of shear reversals during the ebb, as compared to the flood, suggests that these reversals are produced by the entrainment of shallow water from Saanichton Bay. This entrainment would slow down the water above mid-depth in the mainstream.

The occurrence of intense up- and down-welling events lasting longer than 20 minutes is surprising and difficult to explain without some measure of the horizontal distribution of the flow. Flow separation and the production of eddies by a headland are possible (Geyer 1993) and were visually observed in Cordova Channel (D'Asaro, personal communication, 1995). Vertical flow can be induced by transverse flow and flow separation via the mechanism proposed by Garrett and Loucks (1976) and Wolanski et al. (1984).

3.5 Summary

This chapter discusses the measurement principles of an ADCP, and the data processing required to apply this instrument to velocity profiling in a turbulent environment. The ADCP was rigidly mounted to the bottom of Cordova Channel where the flow is mainly tidal with peak currents of 1 m s^{-1} and rms turbulent fluctuations of $O(0.05)$ m s^{-1}.

An ADCP is not equivalent to a chain of point current meters in the sense that only the time-mean velocity vectors, rather than the "instantaneous" ones, can be obtained with ADCP. Turbulence was separated from the "mean" using 20-min averages.

The statistical uncertainty of the velocity estimates stems predominantly from turbulence rather than Doppler noise and is typically about 8×10^{-3} m s^{-1} for the horizontal components and 3×10^{-3} m s^{-1} for $\bar{w}$ during strong flow and less for weaker flows. Because the uncertainty depends on the characteristics of the turbulence rather than the instrument, its evaluation requires rapid sampling (and recording) to resolve the velocity fluctuations. That is, simply recording the ensemble means is not sufficient.

An explicit test for horizontal statistical homogeneity, an assumption made in calculating the mean flow components, was made by comparing the magnitude of an estimated velocity component against the error velocity. The ratio of averaging length to beam separation, N, can be used to predict the reliability of the horizontal velocity estimates. For more than 95% of our observations, the magnitude of the error velocity is less than the statistical uncertainty of the horizontal velocity for $N > 55$. However, N is not a good indicator of the statistical significance of vertical velocity estimates. Using only vertical velocity estimates that exceed the statistical uncertainty of 0.003 m s^{-1}, we find that only 75% of these velocity estimates are more than 3 times larger than the error velocity for $N = 90$. For a 20-min averaging interval, N exceeds 90 only below mid-depth and longer intervals are required to smooth out the instantaneous inhomogeneity over the beam separations.

Bias in the measurement of tilt angles (1° in our case) can easily contaminate the weak vertical flow signals. The effect of this bias can be removed for rigidly mounted deployments by re-processing the data with the correct tilt angles, but this is not possible for a non-rigidly mounted instrument that records only the mean velocity vector. Another source of bias to the vertical velocity estimates for a non-rigidly

mounted ADCP may come from the correlation of tilt and horizontal velocity due to eddies with scales comparable to the beam separation.

The depth-time variations of flow and shear observed in this natural tidal channel are complicated. The flow is asymmetric between the ebb and flood phases of the tide at the site of the ADCP, both in magnitude and direction. Strong transverse flow is observed, and is attributed mainly to the curvature effect produced by a headland at the western side of the channel. The streamwise shear is bottom-enhanced and strong transverse shear is only observed during the ebb. The shear frequently reverses sign at mid-depth during the ebb, this being attributed to the entrainment of water from a shallow bay to the north of the experiment site into the mainstream of the channel. Intensified up/down-welling intervals occur with vertical flow magnitude reaching 0.05 m s^{-1} at mid-depth.

Chapter 4

Turbulence Estimates

4.1 Introduction

Turbulent velocity fluctuations in the ocean are conventionally measured by two types of instruments: shear probes (e.g. Osborn and Crawford, 1980) and point current-meters (e.g. Gross and Nowell, 1983, 1985; McPhee, 1994). Turbulent measurement with acoustic Doppler current profilers (ADCP) is a relatively new technique and possesses the advantages of remote sensing.

Several approaches have been developed to estimate turbulent quantities with an ADCP by taking advantage of the rapid sampling of this instrument. Gargett (1988, 1994) reported on a "large-eddy" approach that provides one estimate of the turbulent kinetic energy (TKE) dissipation rate, by using a narrowband ADCP with a true vertical beam. Van Haren et al. (1994) applied a "direct-correlation" approach to estimate the velocity covariance (Reynolds stress) in the internal wave frequency band, by using a moored narrowband ADCP with standard beam configuration. The third method is the "variance technique" that derives Reynolds stress and TKE density from the auto-covariances of along-beam velocities. This method was first explored by Lohrmann et al. (1990) with a pulse-to-pulse coherent sonar, and was recently applied by Stacey (1996) with a broadband ADCP. The advantage of using a broadband ADCP is that the noise level in velocity profiling is lower than that of a narrowband unit, and the profiling range is much larger than that of a pulse-to-pulse coherent sonar.

In this chapter, we address the issue of obtaining reliable estimates of turbulent

quantities with the "variance technique" and, thereby, extend the work on first order moments presented in the previous chapter.

4.2 Deriving turbulent products from variances of along-beam velocities

As shown in Eq. (3.1), the measured velocity along the ith (i =1, ..., 4) beam, b_i, is the sum of the horizontal and vertical components, u_i, v_i, w_i, at the position of b_i. Each of these velocities is decomposed into a mean part and a turbulent fluctuating part, i.e., $b_i = \bar{b_i} + b_i'$,$u_i = \bar{u_i} + u_i'$, etc. To derive the mean velocity vector, we need to assume that the mean flow is statistically homogeneous in horizontal space over the distances separating the beams, i.e., $\bar{u_1} = \bar{u_2}$, etc. (Chapter 3). To derive the Reynolds stress and the TKE density, we must further assume that all the second-order moments of turbulent velocity fluctuations are horizontally homogeneous, i.e., $\overline{u_1'^2} = \overline{u_2'^2}$, $\overline{u_1'w_1'} = \overline{u_2'w_2'}$, etc.

The assumption of the horizontal homogeneity of the mean flow can be explicitly tested by comparing the magnitudes of either the horizontal or vertical velocity components against that of the "error" velocity (half of the difference between the two vertical velocity estimates from two beam pairs). In Chapter 3, we showed that for the magnitude of the error velocity to be less than 1% of the mean horizontal speed at the 95% confidence level, the averaging length scale (speed multiplied by averaging time interval) needs to be 55 times larger than the beam separating distances. There are no explicit tests for the homogeneity of the second-order moments. We anticipate that at least a similar amount of averaging is required for turbulent products (the second-order moments).

From the variances of along beam velocities, i.e., $\overline{b_i'^2}$, one can derive two components of the Reynolds stress

$$-\overline{u'w'} = \frac{\overline{b_2'^2} - \overline{b_1'^2}}{2\sin 2\theta} + \varphi_3(\overline{u'^2} - \overline{w'^2}) - \varphi_2\overline{u'v'}, \tag{4.8}$$

$$-\overline{v'w'} = \frac{\overline{b_4'^2} - \overline{b_3'^2}}{2\sin 2\theta} - \varphi_2(\overline{v'^2} - \overline{w'^2}) + \varphi_3\overline{u'v'}, \tag{4.9}$$

and a quantity

$$S = \frac{1}{4\sin^2\theta}(\overline{b_1'^2} + \overline{b_2'^2} + \overline{b_3'^2} + \overline{b_4'^2}) - (\varphi_3\overline{u'w'} - \varphi_2\overline{v'w'})(\frac{2}{\tan^2\theta} - 1). \tag{4.10}$$

The quantity S is related to the TKE density $q^2/2 = (\overline{u'^2} + \overline{v'^2} + \overline{w'^2})/2$ by

$$S = \frac{1}{1+\alpha}\Big(1 + \frac{2\alpha}{\tan^2\theta}\Big)q^2/2, \tag{4.11}$$

where $\alpha = \overline{w'^2}/(\overline{u'^2} + \overline{v'^2})$ is a measure of turbulence anisotropy.

The anisotropy ratio α cannot be determined from an ADCP with only four beams. For extremely anisotropic turbulence $\alpha = 0$ hence $S = q^2/2$; whereas in the limit of isotropic turbulence $\alpha = 0.5$, and $S = 2.7q^2/2$ for $\theta = 30°$. Assuming $\alpha = 0.2$ (consistent with the measurement results of Stacey (1996) in unstratified flow), $S = 1.8q^2/2$, so that the data can be used to estimate q^2.

Apart from the neglected second and higher order terms in φ_2 and φ_3, (4.8) and (4.9) also contain undetermined terms $\overline{u'^2} - \overline{w'^2}$, $\overline{v'^2} - \overline{w'^2}$, and $\overline{u'v'}$. Neglecting these terms brings a bias to the estimates of stress, which is examined in section 3.a. To eliminate this bias we need a fifth beam directed along the instrument axis (Lohrmann et al. 1990).

Calculating the Reynolds stress and the quantity S with (4.8)-(4.10) requires that the tilt angles φ_2 and φ_3, as well as the heading angle φ_1, are time invariant. In other words, the instrument needs to be rigidly mounted. For a non-rigidly mounted deployment, the decomposition of along-beam velocity b_i is meaningless, because its variations can be caused by changes in the three angles.

To illustrate the problem with tilt-eddy correlation in estimating turbulent products, we examine the case when only the roll angle φ_3 changes with time, the heading angle is constant, and the pitch angle $\varphi_2 = 0$. By assuming that $\overline{u_1'\varphi_3} = \overline{u_2'\varphi_3} = \overline{u'\varphi_3}$,

etc., (4.8) changes to

$$-\overline{u'w'} \approx \frac{\overline{b_2'^2} - \overline{b_1'^2}}{2\sin 2\theta} + (\overline{\bar{u}u'\varphi_3} - \overline{\bar{w}w'\varphi_3}) + (\overline{u'^2\varphi_3} - \overline{w'^2\varphi_3}), \tag{4.12}$$

where the terms with magnitudes of $O(\varphi_3^2)$ have been dropped. The term which is most likely to introduce a large error is $\overline{\bar{u}u'\varphi_3}$, i.e, the product of eddy-tilt correlation and the mean horizontal velocity. A 2° rms tilt angle fluctuation and a 0.1 m s^{-1} rms turbulent velocity fluctuation will produce a bias of 4×10^{-3} m s^{-1} if the two fluctuations are perfectly correlated. In a mean current of 1 m s^{-1}, the term $\overline{\bar{u}u'\varphi_3}$ will cause a bias of 4×10^{-3} m^2 s^{-2}, which is larger than the typical magnitude of Reynolds stress. Even if the tilt-eddy correlation is as low as 0.1, the Reynolds stress contamination is still 4×10^{-4} m^2 s^{-2}, too large for most practical flows.

The only case that turbulence can be possibly measured with a non-rigidly mounted unit is where dominant energy-containing eddies are much larger than the beam separating distances. In that case the velocity field is instantaneously homogeneous over the beam separating distances, hence a ping-by-ping transformation gives the true velocity vector. The turbulent velocity fluctuations can be obtained by applying Reynolds decomposition to the time series of velocity vector, and the products of turbulent fluctuations can then be calculated. This "direct correlation" approach was adopted by van Haren et al. (1994) to measure the Reynolds stress in the internal wave band over a sloping bottom on the continental shelf.

4.3 Error analyses

In this and the two subsequent sections, we present detailed analyses of a 1-day long, 4-ping averaged data. A sample of this data is shown in Fig. 3.9.

a. Bias in turbulence estimates

The measurement of beam velocity contains an uncertainty, referred to as Doppler noise. Denoting the measured value of along-beam velocity as b_i^*, its true signal as

b_i, and noise as N_i, one has

$$b_i^* = b_i + N_i. \tag{4.13}$$

As described in Chapter 2, the noise standard deviation was determined to be 0.01 to 0.015 m s^{-1} up to a profiling range of 40 m, for 4-ping averaged ensembles with 1 m cell size, from an *in situ* test conducted in an inlet with almost slack water. This noise standard deviation is used in the following analyses, although the noise level may vary slightly with changes in flow and water properties, e.g., the size and abundance of sound scatters in the water.

Doppler noise systematically biases the estimate of S to a higher level S^*, i.e.,

$$S^* = S + \frac{1}{\sin^2\theta} var(N). \tag{4.14}$$

For $\theta = 30°$ this bias amounts to 4 times of the variance of N_i, and equals to $4-9\times10^{-4}$ m^2 s^{-2} for 4-ping averaged data. In the remaining analyses, a bias of 5×10^{-4} m^2 s^{-2} is removed from the estimates of S. Doppler noise may introduce a bias in the Reynolds stress estimates if $var(N_i)$ varies among the different beams. If the noise levels of the two beams in a pair are identical, then by subtracting the beam velocity variances the biases are canceled out, hence

$$-\overline{u'w'}^* = -\overline{u'w'}. \tag{4.15}$$

In this optimal case, the estimates of Reynolds stress contain no bias due to Doppler noise.

In section 4.2, we have noticed that neglecting the terms associated with tilt angles introduces another type of bias to the Reynolds stress estimates. From (4.8) and (4.9), this bias is proportional to the magnitudes of the tilt angles and the undetermined terms $\overline{u'^2} - \overline{w'^2}$, $\overline{v'^2} - \overline{w'^2}$, and $\overline{u'v'}$. If turbulence tends to be isotropic, $\overline{u'^2} - \overline{w'^2}$ and $\overline{v'^2} - \overline{w'^2}$ are small. For anisotropic turbulence, $\varphi_3(\overline{u'^2} - \overline{w'^2}) = O(\varphi_3\overline{q^2}/2)$. The magnitude of $\overline{q^2}/2$ is approximately 5 times larger than the Reynolds stress (e.g., Gross and Nowell, 1983). Hence, at most, the bias due to $\varphi_3(\overline{u'^2} - \overline{w'^2})$ amounts to

17% of the magnitude of $-\overline{u'w'}$ for $\varphi_3 = -2.0°$ as in this experiment. Similarly, if the magnitude of $-\overline{u'v'}$ is not significantly larger than that of $-\overline{u'w'}$ or $-\overline{v'w'}$, then neglecting $\varphi_2\overline{u'v'}$ and $\varphi_3\overline{u'v'}$ will not cause a significant bias. For pitch and roll angles exceeding a few degrees, this bias may be significant.

b. Statistical uncertainties

In this analysis, we choose 20 mins as the ensemble averaging time to calculate the turbulent quantities. The low- and high-frequency velocity components are separated by a low-pass 4-th order butterworth filter at zero-phase. Variances of beam velocity fluctuations are then calculated and smoothed with the same filter, and averaged over 20-min intervals to give estimates of Reynolds stress and the quantity S.

To test if a stress estimate is statistically different from zero, we apply a non-parametric approach that follows a suggestion by B. Ruddick (see, Fleury and Lueck, 1994). Differences of the beam velocity variances in (4.8) and (4.9) are rearranged into a "covariance" form, e.g.,

$$\overline{b_2'^2} - \overline{b_1'^2} = \overline{(b_2' + b_1')(b_2' - b_1')}. \tag{4.16}$$

Hence, the Reynolds stress $-\overline{u'w'}$ is proportional to the covariance of the two time series $(b_2' + b_1')$ and $(b_2' - b_1')$ at zero lag. The de-correlation time scales of the beam velocities are typically 15 s during strong flows and 6 s during weak flows (see Fig. 3.10 in Chapter 3). If we shift one time series, say $(b_2' + b_1')$, by a lag larger than 30 s, then its statistical nature is unchanged, but it will have no correlation with the other time series, $(b_2' - b_1')$, on average. A histogram of the zero covariances is obtained by randomly choosing the lag many times (e.g., 1000) and then computing the covariances. If the zero-lag covariance, i.e., the estimated stress, is outside of the 95% confidence levels of the zero covariance, then this estimate is accepted as statistically different from zero. Fig. 4.17 illustrates the examples of applying this method to two 20-min intervals of data, one during the strong ebb around day 23.91, and one during the

weak flood around day 24.65. For each interval we calculate the 95% significance levels (denoted as Δ_{95}) for both the along- and cross-channel components of the stress, separately. During the strong ebb, the along-channel stress is significantly different from zero, and the cross-channel stress is marginally different from zero, at the 95% significance levels. During the weak flood, the along-channel stress is comparable to the size of the 95% significance levels, whereas the cross-channel stress is not different from zero.

We have also applied a bootstrap method (Efron and Tibshirani 1993, Chapter 13) to determine the statistical uncertainties for both the stress and S estimates. For each 20-min interval, time sequences of the vectors (b_1', b_2', b_3', b_4') are randomly resampled at identical time indices to construct a new matrix of beam velocity fluctuations. In one calculation the new matrix has the same length with the original data, assuming that each ensemble of (b_1', b_2', b_3', b_4') to be an independent measurement. In the other calculation, the length of the resampled matrix is reduced by a factor corresponding to the de-correlation time lag of the original data: 15 s for the interval during the strong ebb and 6 s for the interval during the weak flood, respectively. The "stress" and "S" for the resampled data are calculated according to equations (4.8)-(4.10). By repeating the above calculations 1000 times, distributions of the "stress" and "S" are constructed. The 95% confidence intervals for the stress and the quantity S, denoted as $(\delta_{95})_1$ for the first calculation and $(\delta_{95})_2$ for the second calculation, respectively, are derived from the distributions.

Table 4.1 compares the 95% zero-stress significance levels (Δ_{95}) with the 95% confidence intervals ($(\delta_{95})_1$ and $(\delta_{95})_2$) for the two 20-min intervals of data chosen. For the Reynolds stress, $(\delta_{95})_2$ is larger than $(\delta_{95})_1$ by a factor of $1.5 \sim 2$, with Δ_{95} lying in between. The 95% confidence intervals for S, determined with the bootstrap method, amounts less than 20% of the estimates of S.

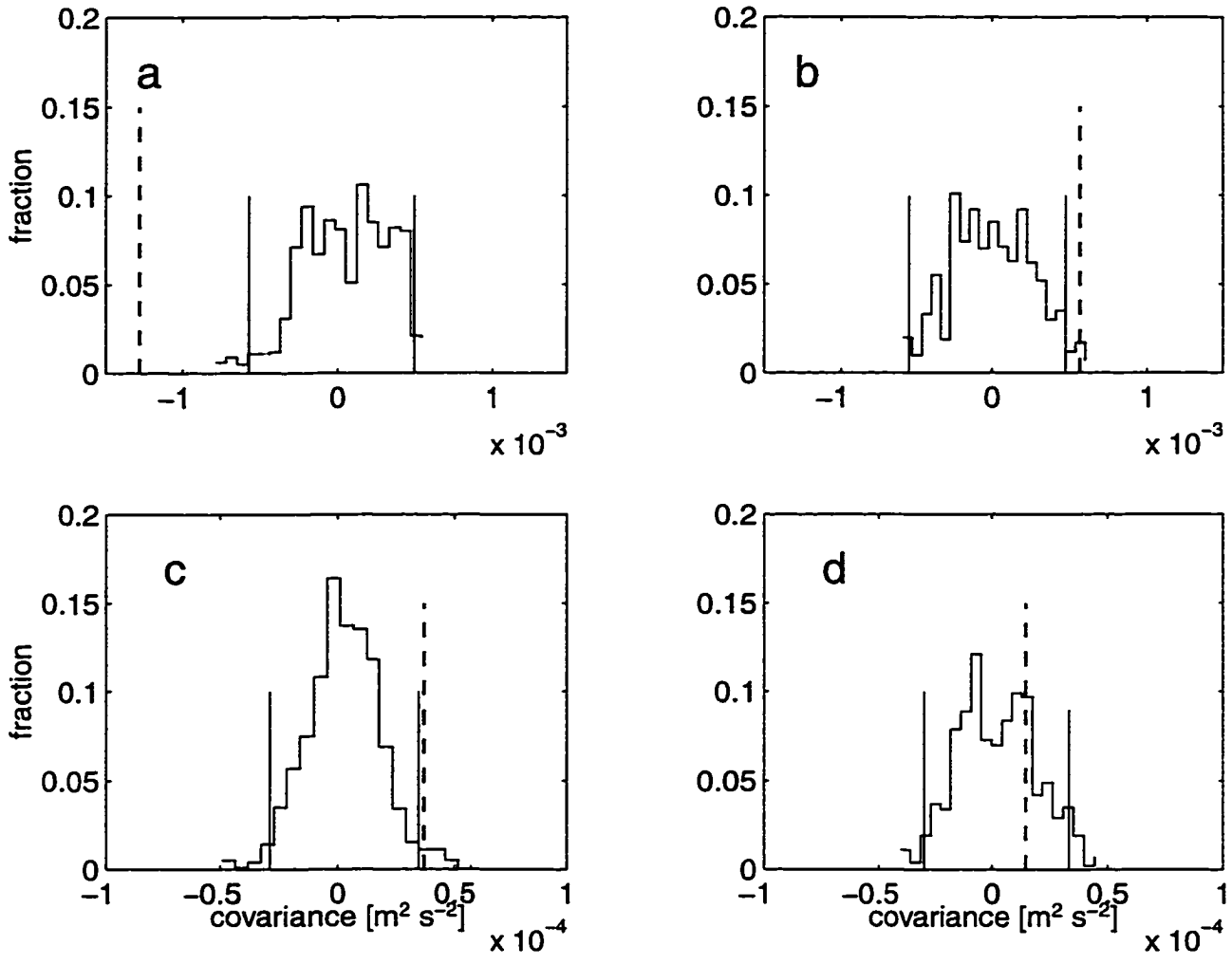

Figure 4.17: Examples of the measured stress estimates (heavy dashed lines) and the distribution (histogram) of the zero covariances obtained by computing the "covariances" (Eq. (4.16)) 1000 times at random lags larger than 30 s. The solid vertical lines denote the 95% significance levels for zero covariances. Panels (a) and (b) are for the along- and cross-channel components of the stress at a 20-min interval during the strong ebb; panels (c) and (d) are the respective stress estimates for a 20-min interval during the weak flood.

Table 4.1: Estimates of Reynolds stress and S, the 95% significance level (Δ_{95}) for stress and two estimates of the 95% confidence intervals (($\delta_{95})_1$ and $(\delta_{95})_2$) for both stress and S (all quantities are in units of 10^{-4} m^2 s^{-2}). The estimates are for two 20-min intervals at z=3.6 m.

		mean	Δ_{95}	$(\delta_{95})_1$	$(\delta_{95})_2$
strong ebb	$(-\overline{u'w'})_s$	-13.0	±5.72	±3.34	±8.32
	$(-\overline{v'w'})_n$	5.72	±5.44	±2.46	±5.66
	S	102		±8.12	±19.0
weak flood	$(-\overline{u'w'})_s$	0.367	±0.33	±0.27	±0.37
	$(-\overline{v'w'})_n$	0.148	±0.32	±0.25	±0.35
	S	4.08		±0.71	±0.96

In the following, we take the estimates of Δ_{95} as the indicator of statistical uncertainty for stress estimates. Time variations of the Reynolds stresses at z=3.6 m, as well as the corresponding estimates of Δ_{95}, are shown in Fig. 4.18. For clarity in linear coordinates, we plot the "local friction velocities"

$$u_{*s} = \frac{(\overline{-u'w'})_s}{|(\overline{-u'w'})_s|^{1/2}}, \tag{4.17}$$

$$u_{*n} = \frac{(\overline{-u'w'})_n}{|(\overline{-u'w'})_n|^{1/2}}, \tag{4.18}$$

where $(\overline{-u'w'})_s$ and $(\overline{-u'w'})_n$ are the along- and cross-channel components of the Reynolds stress (the along- and cross-channel directions are parallel and normal to the depth-mean flow, respectively). At z=3.6 m, estimates of the along-channel stress are generally significantly different from zero. The magnitudes of the cross-channel stress are marginally significant for half the time and not significant for the remainder.

Fig. 4.19 shows, at three heights (z=3.6, 15.6, and 27.6 m), the magnitudes of the Reynolds stress, $|\overline{u'w'}|$, the quantity S, and the 95% significance levels of the stress magnitude, denoted as $|\Delta_{95}|$. The three quantities vary with time, in accordance with the changes in beam velocity variances and the magnitude and direction changes of the time-mean flow (Fig. 3.9). There is a good correlation between the changes in the three quantities. At z=3.6 m and z=27.6 m, the magnitudes of the stress are generally larger than $|\Delta_{95}|$, but by less than a factor of 10. At mid-depth, where the

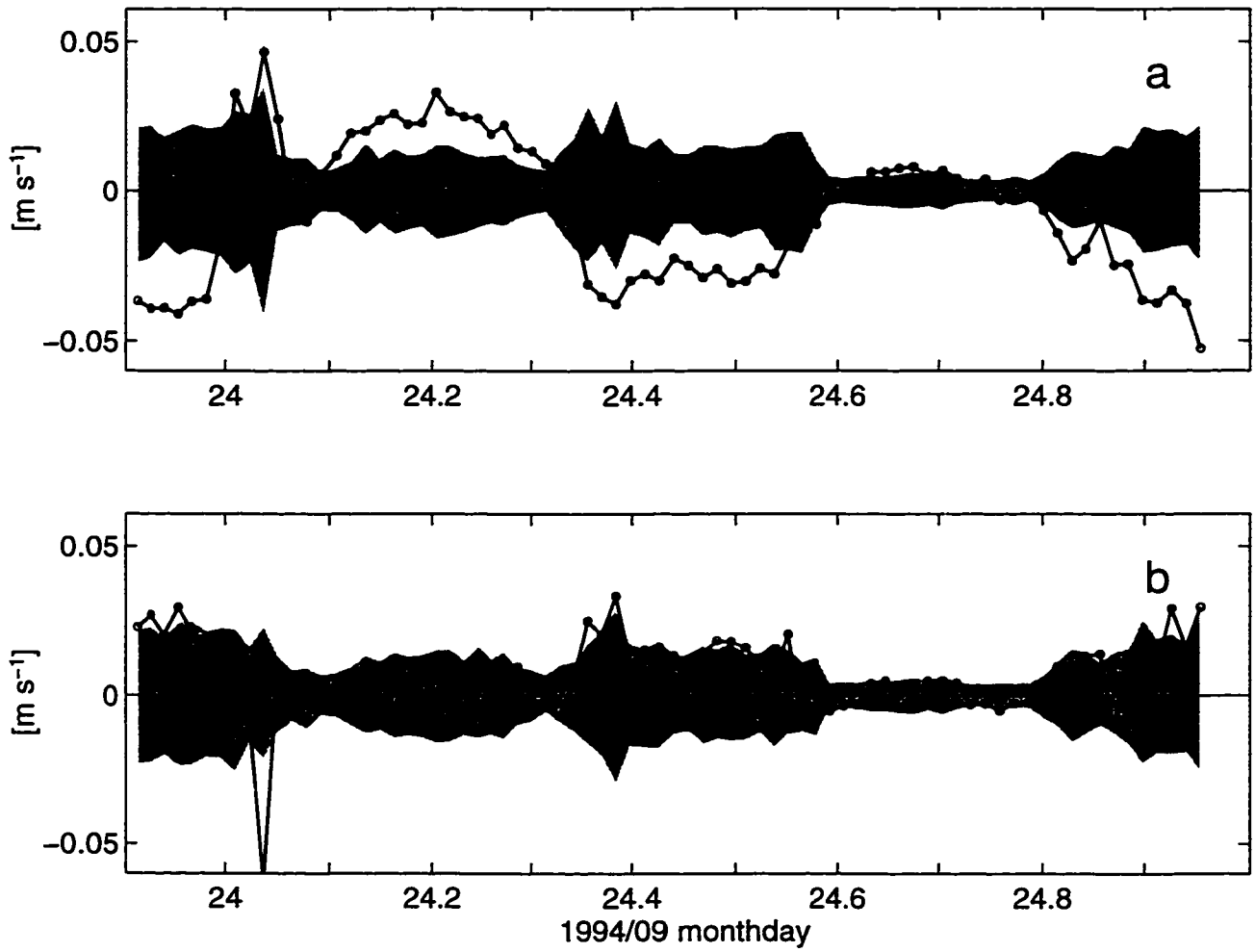

Figure 4.18: The variation of (a) along- and (b) cross-channel components of the local friction velocities u_{*s} and u_{*n} (solid lines with circles) and the 95% significance levels (shaded areas) at z=3.6 m.

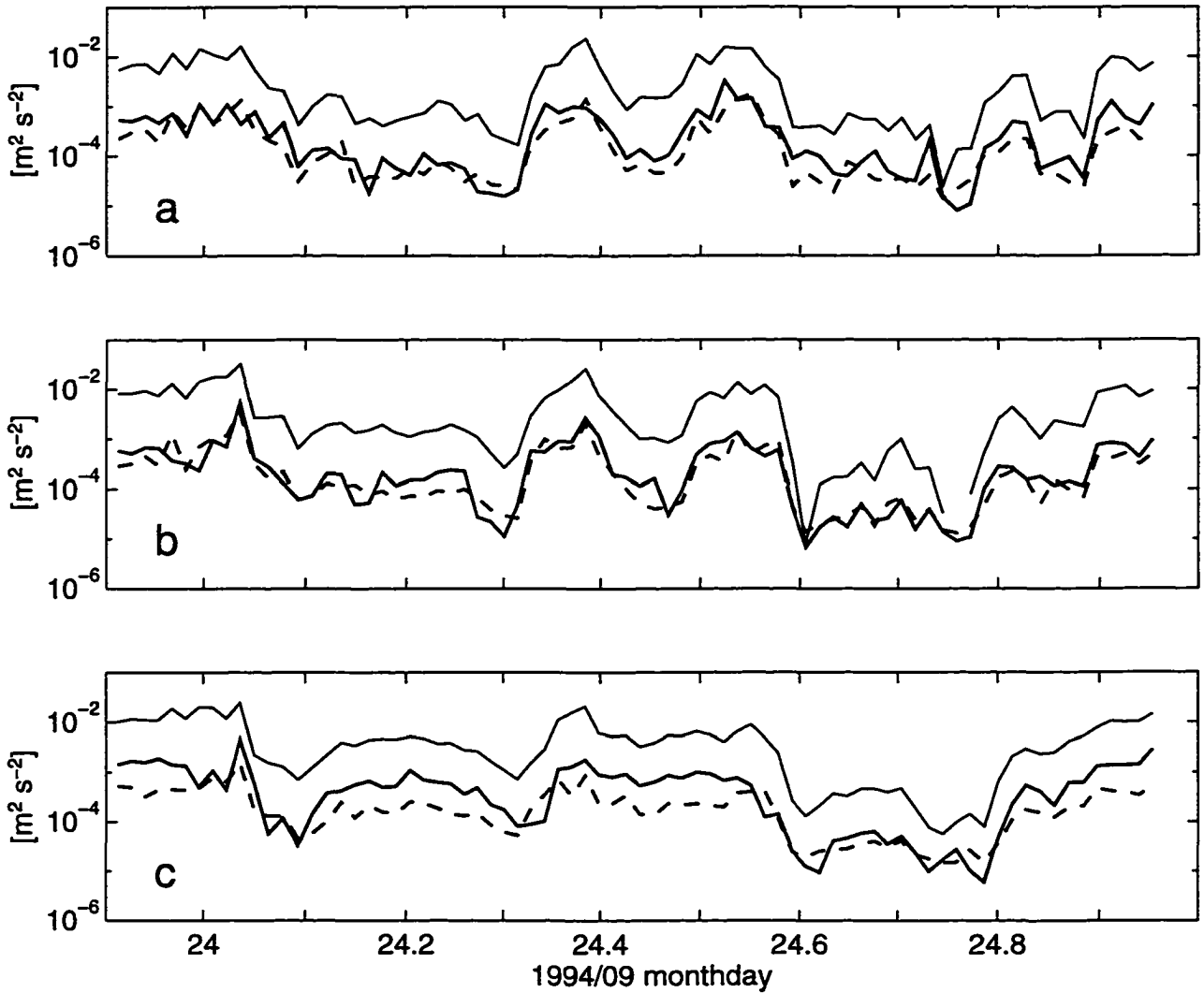

Figure 4.19: Variations of stress magnitude (heavy solid lines), the size of its 95% significance intervals (dashed lines), and TKE density S (thinner solid lines) at (a) z = 27.6 m, (b) z = 15.6 m, and (c) z = 3.6 m.

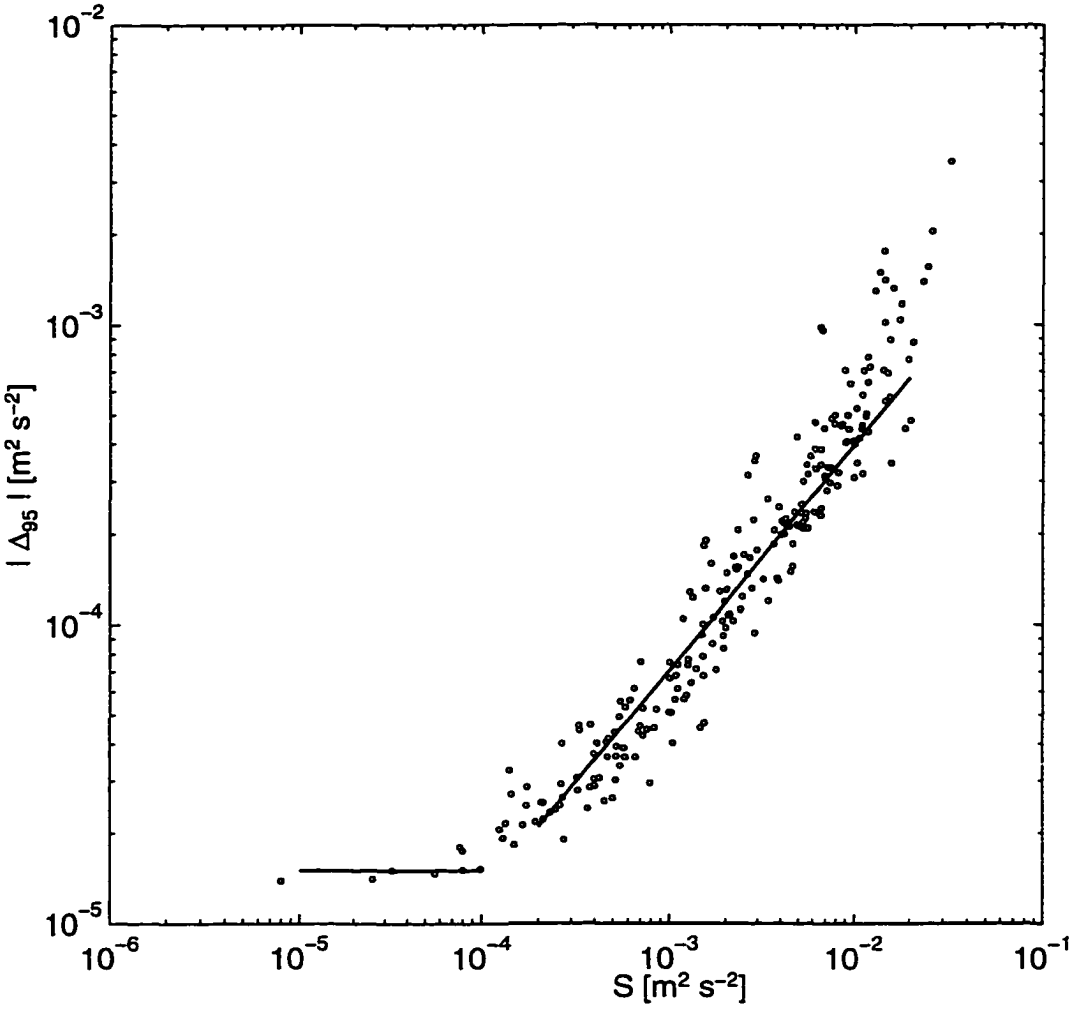

Figure 4.20: Scatter diagram (open circles) of $|\Delta_{95}|$ (y-axis) v. S (x-axis) at three levels (z = 3.6, 15.6, and 27.6 m). The two solid lines represent Eqs. (4.20) and (4.21).

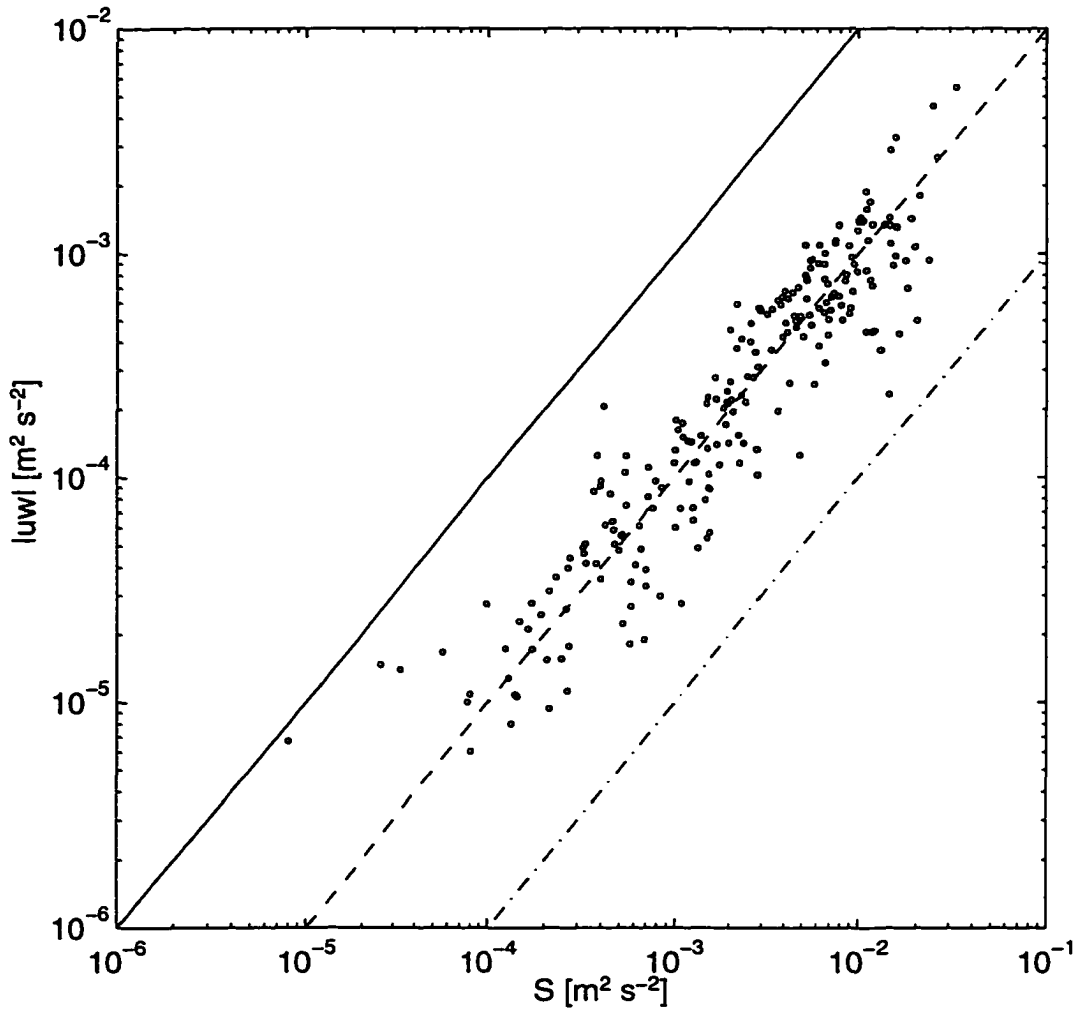

Figure 4.21: Scatter diagram of $|-\overline{u'w'}|$ (y-axis) v. S (x-axis) at three levels (z = 3.6, 15.6, and 27.6 m).

stress is the weakest, $|\Delta_{95}|$ and $|\overline{u'w'}|$ are comparable.

There are apparently two regimes in the $|\Delta_{95}|$ v. S diagram (Fig. 4.20). For $S > 10^{-4}$ m^{2}s^{-2}, $|\Delta_{95}|$ increases with S according to

$$|\Delta_{95}| = S^{3/4}/80, \tag{4.19}$$

whereas for $S < 10^{-4}$ m^{2}s^{-2},

$$|\Delta_{95}| = 1.5 \times 10^{-5} \text{ m}^2 \text{ s}^{-2}, \tag{4.20}$$

is almost a constant. Fig. 4.21 is the scatter diagram of $|\overline{u'w'}|$ v. S. Changes in $|\overline{u'w'}|$ are approximately proportional to S according to

$$|\overline{u'w'}| = 10^{-1} S. \tag{4.21}$$

The two-regime relationship of $|\Delta_{95}|$ v. S will be discussed in section 4.4. We notice here that for $S > 10^{-4}$ m^{2}s^{-2}, combining (4.19) with (4.21), one obtains

$$|\Delta_{95}| = 7.0 \times 10^{-2} (|\overline{u'w'}|)^{3/4}. \tag{4.22}$$

Equation (4.22) shows that $|\Delta_{95}|$ does not increase linearly with increasing $|\overline{u'w'}|$. The ratio of stress magnitude to its 95% significance level increases as the stress magnitude increases. For example, $|\overline{u'w'}|$ is 1, 2, and 3 times larger than $|\Delta_{95}|$ when stress magnitude is $(0.24, 3.84, 19.0) \times 10^{-4}$ m^{2}s^{-2}, respectively.

c. Contributions from low-frequency fluctuations

We have not fully justified the choice of 20 mins as the cutoff period to separate the high- and low-frequency variations. We notice from Fig. 3.9 that a filter at a 20-min cutoff period cannot fully separate the tidal signal and turbulence, because variations at periods longer than 20 mins but less than tidal periods still exist. We need to check if these low-frequency variations make contributions to the estimates of Reynolds stress and the quantity S.

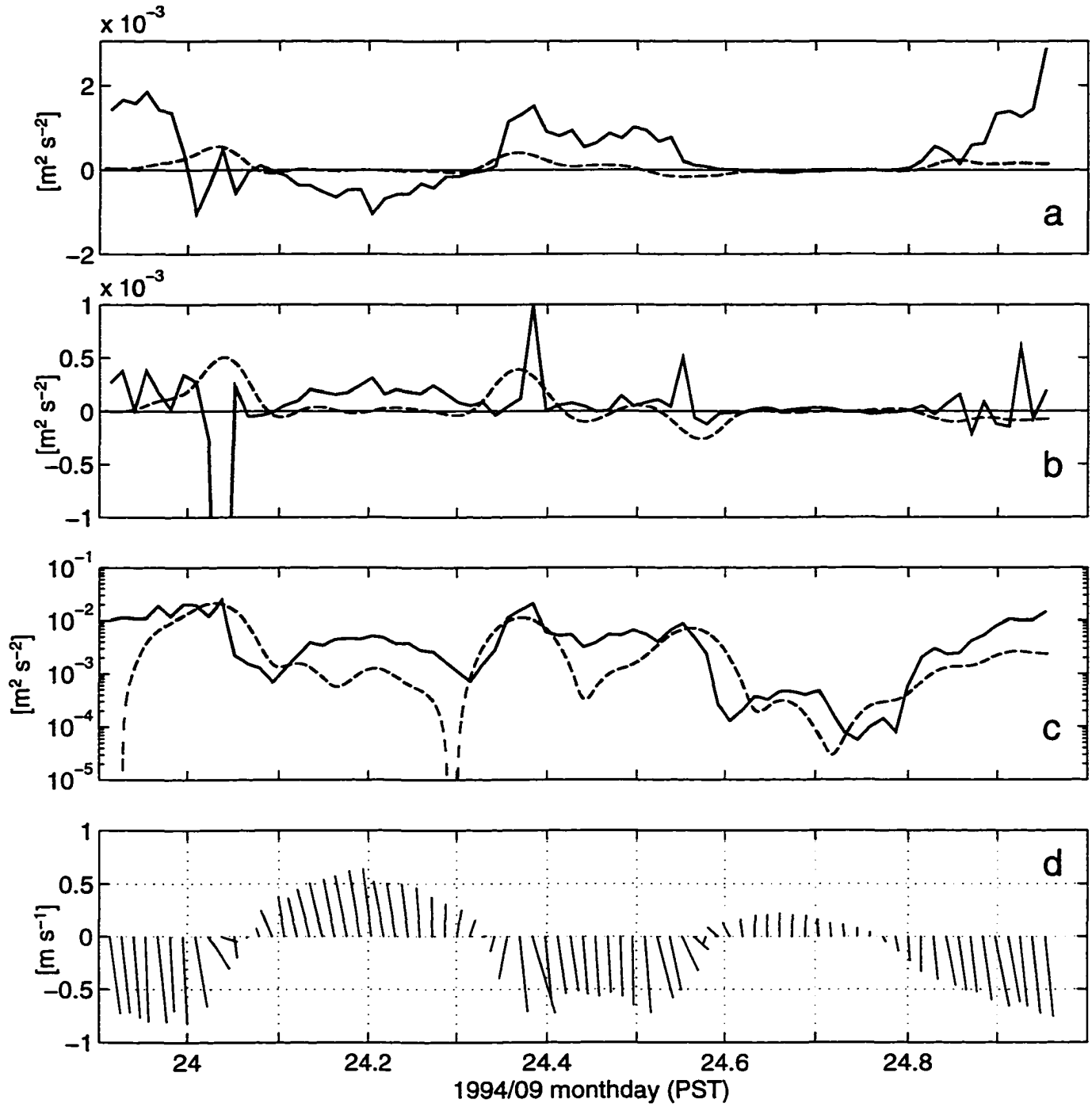

Figure 4.22: Two components of Reynolds stress (a) $(\overline{-u'w'})_s$, (b) $(\overline{-u'w'})_n$, and (c) S (all in $m^2\ s^{-2}$) calculated from fluctuations at < 20 min band (solid lines) and from $20 - 120$ min band (dashed lines) at $z = 3.6$ m. Panel (d) shows the stick diagram of the 20-min mean flow at the same height.

Fig. 4.22 compares, at z=3.6 m, the magnitudes of two components of Reynolds stress and S calculated from fluctuations with periods less than 20 mins and their counterparts calculated from fluctuations with periods between 20 and 120 mins. For Reynolds stress, the low-frequency contributions are in general less than 1×10^{-4} m^2 s^{-2} in magnitude. For S, the low-frequency contributions are an order of magnitude smaller than S calculated from fluctuations at periods less than 20 mins, except during the turning of the tide (e.g., near day 24.05) and the flow turning in direction during the ebb (e.g., the two events at day 24.4 and 24.5). During the flow turning in direction, however, both the high- and low-frequency fluctuations are not stationary, hence, the estimates of turbulent products are not reliable. We conclude that the contributions from low-frequency fluctuations are not important to the estimates of Reynolds stress and TKE density.

4.4 The causes of statistical uncertainty

The statistical uncertainty of an estimated quantity can be due to several causes. First of all, to get a statistical estimate for a stochastic process requires the process to be stationary. Fig. 3.9 shows that the intensity of the high-frequency fluctuations is not stationary throughout the tidal cycle. Our concern is on the stationarity of turbulence (and mean flow) over the time intervals for which we conduct statistical analysis. Fig. 4.23 shows four 20-min intervals of velocity data along beams 1 and 2 at the lowest cell (z=3.6 m). The four intervals are chosen from different phases of the tide, with interval (a) centered at day 23.91 during the strong ebb, (b) at day 24.04 during the turning of the tide, (c) at day 24.16 during the strong flood, and (d) at day 24.66 during the weak flood. By visual inspection, during intervals (a), (c), and (d), the low-frequency flow appeared to be nearly steady, and the intensity of high-frequency velocity fluctuations stationary. An extremely large velocity anomaly happened during interval (b) and lasted about 2 mins, and neither the flow nor the

high-frequency fluctuations were stationary.

The uncertainty in the estimate of the mean of a time series $x_i (i = 1, \cdots, N)$ can be examined by looking at the cumulative mean of this series, defined as $\Sigma_{i=1}^{n} x_i/n$ $(n = 1, \cdots, N)$. As pertinent to the estimates of Reynolds stress and S, we examine the cumulative means of $b_2'^2 - b_1'^2$, $b_4'^2 - b_3'^2$, and $b_1'^2 + b_2'^2 + b_3'^2 + b_4'^2 - 5 \times 10^{-4}$ m^2 s^{-2} (where 5×10^{-4} m^2 s^{-2} is the bias in S due to Doppler noise). Note that $\overline{b_2'^2} - \overline{b_1'^2}$ and $\overline{b_4'^2} - \overline{b_3'^2}$ are approximately proportional to the along- and cross-channel stress, respectively. Figs. 4.24 and 4.25 show the time series of $b_2'^2 - b_1'^2$ and $b_1'^2 + b_2'^2 + b_3'^2 + b_4'^2 - 5 \times 10^{-4}$ m^2 s^{-2}, as well as their cumulative means, at z=3.6 m, for the four 20-min intervals shown in Fig. 4.23. Each 20-min interval contains many events of different strength. During intervals of strong flow (Figs. 4.24 and 4.25, panels (a) and (c)), the cumulative means become nearly constant after averaging over 5 mins, and the averages between 5 and 20 mins only fluctuate at magnitudes less than 10% of the overall averages. During the weak flood (panels (d)), the cumulative mean of $b_1'^2 + b_2'^2 + b_3'^2 + b_4'^2 - 5 \times 10^{-4}$ m^2 s^{-2} becomes constant after 12 min averaging, whereas the cumulative mean of $b_2'^2 - b_1'^2$ varies over a range equal to the final mean. For the interval during the turning of tide (panels (b)) the cumulative means of both time series do not become independent of the averaging length, and the overall averages are dominated by the single strong event. The turning of the tide is not a stationary interval while the weak flood is stationary, and the variations in the cumulative mean of $b_2'^2 - b_1'^2$ is merely due to the small stress that is not significantly different from zero.

To illustrate the variations in uncertainty with height above the seabed, we show the cumulative means of $b_2'^2 - b_1'^2$, $b_4'^2 - b_3'^2$ and $b_1'^2 + b_2'^2 + b_3'^2 + b_4'^2 - 5 \times 10^{-4}$ m^2 s^{-2} at seven heights for the 20-min interval during the strong ebb (Fig. 4.26). It is seen that the cumulative means of $b_2'^2 - b_1'^2$ are nearly constant after 10-min averaging at all levels (panel (a)). The cumulative means of $b_4'^2 - b_3'^2$ are also nearly constant except at z = 11.6 m, where the means change sign at about 10 mins of averaging

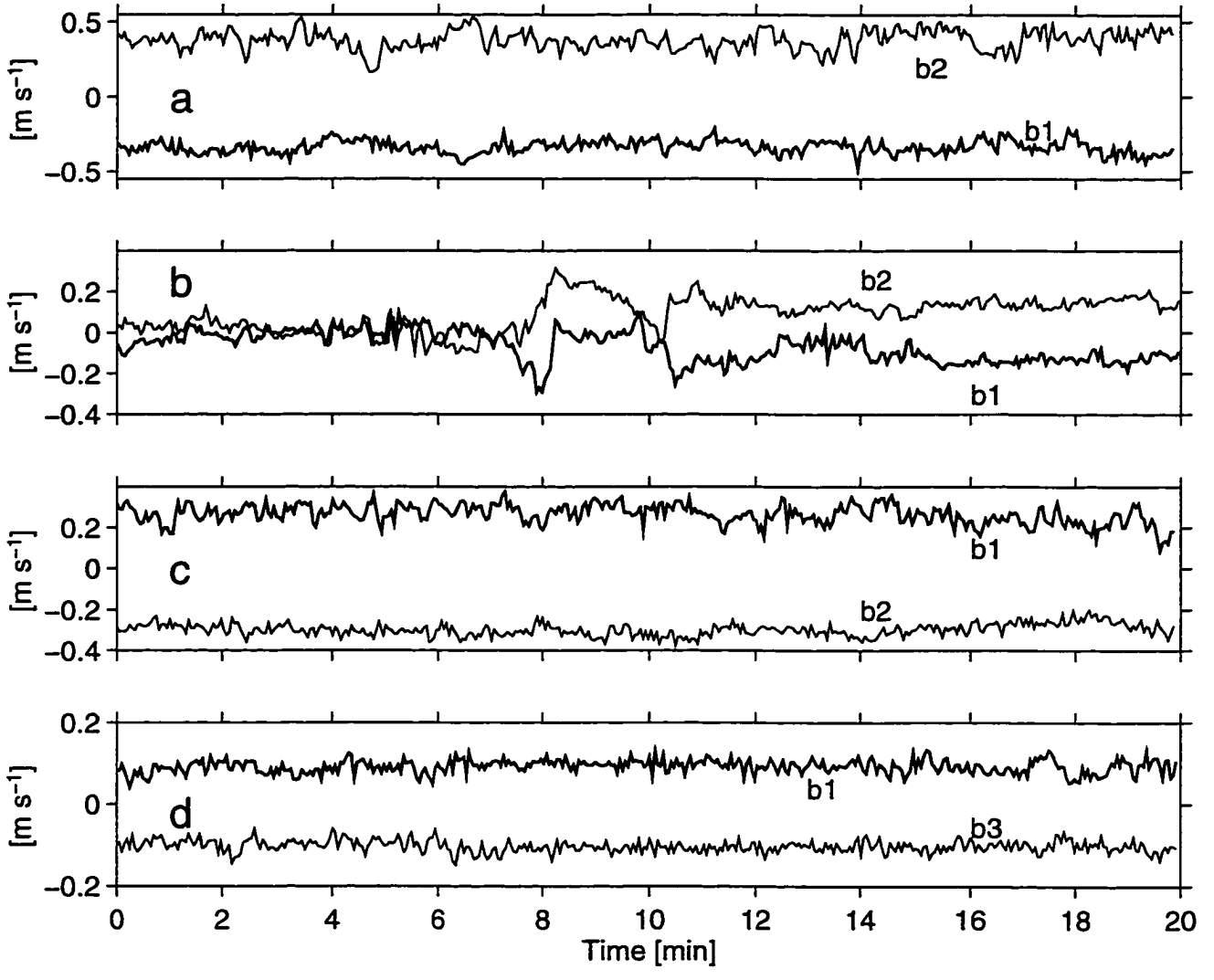

Figure 4.23: Four 20-min intervals of velocity data at z=3.6 m from beam 1 (b1) and beam 2 (b2). The four intervals are centered at (a) day 23.91, (b) day 24.03, (c) day 24.15, and (d) day 24.65.

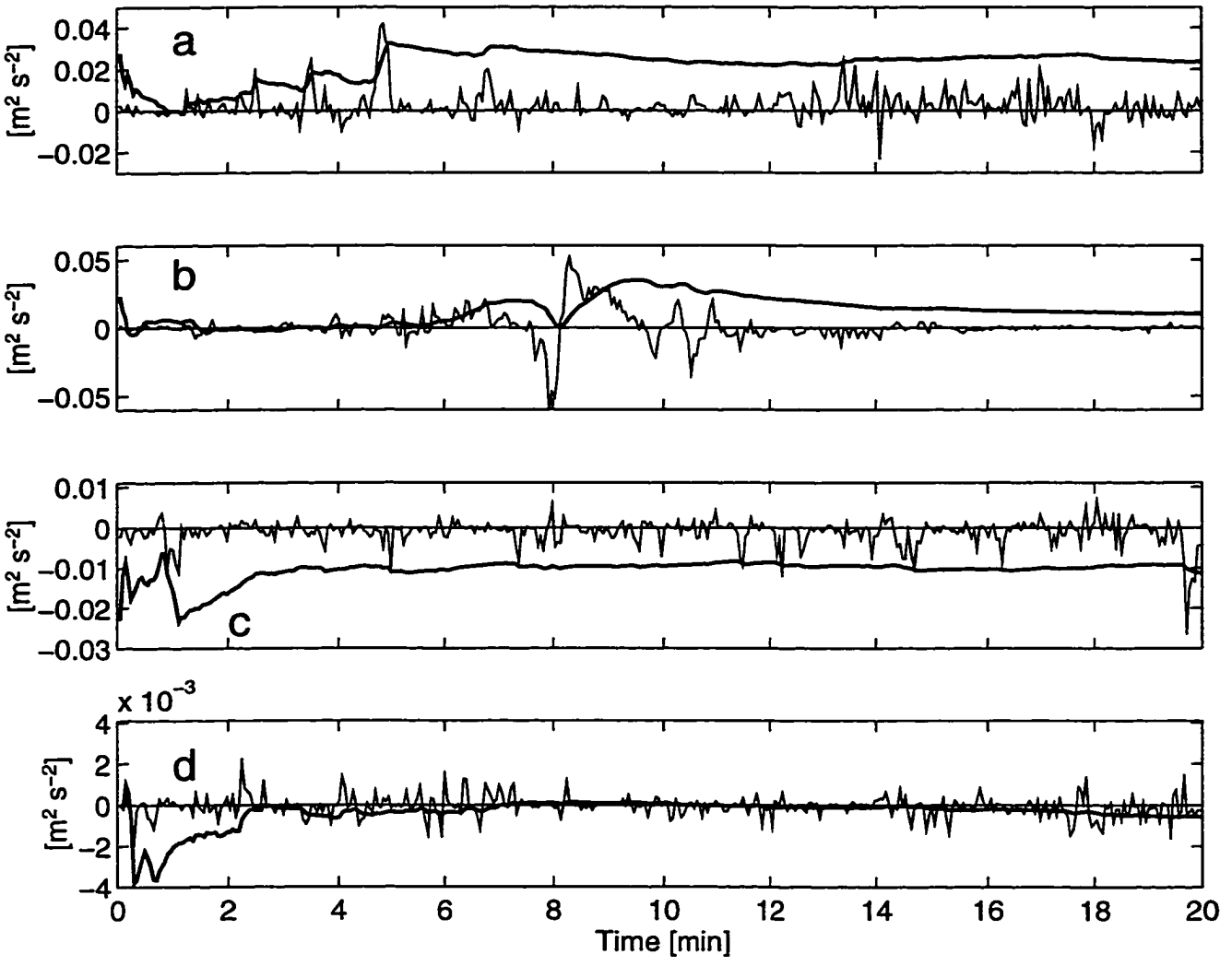

Figure 4.24: Variations of $b_2'^2 - b_1'^2$ (thinner lines) and 10 times its cumulative means (thicker lines) at z = 3.6 m. Each panel corresponds to one of the 20-min intervals shown in Fig. 4.23.

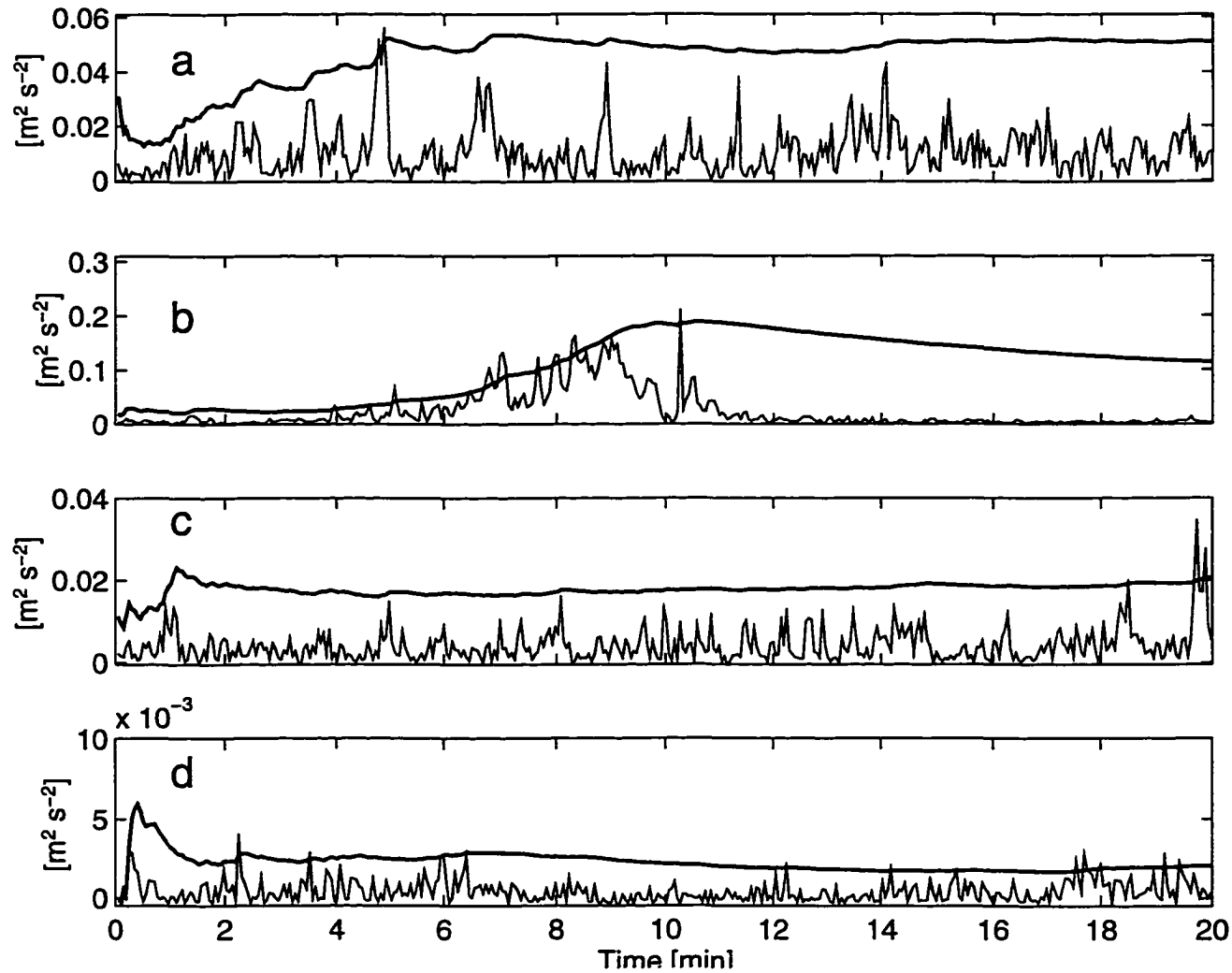

Figure 4.25: Variations of $b_1'^2 + b_2'^2 + b_3'^2 + b_4'^2 - 5 \times 10^{-4}$ m^2 s^{-2} (thinner lines) and 5 times its cumulative means (thicker lines) at z = 3.6 m. Each panel corresponds to one of the 20-min intervals shown in Fig. 4.23.

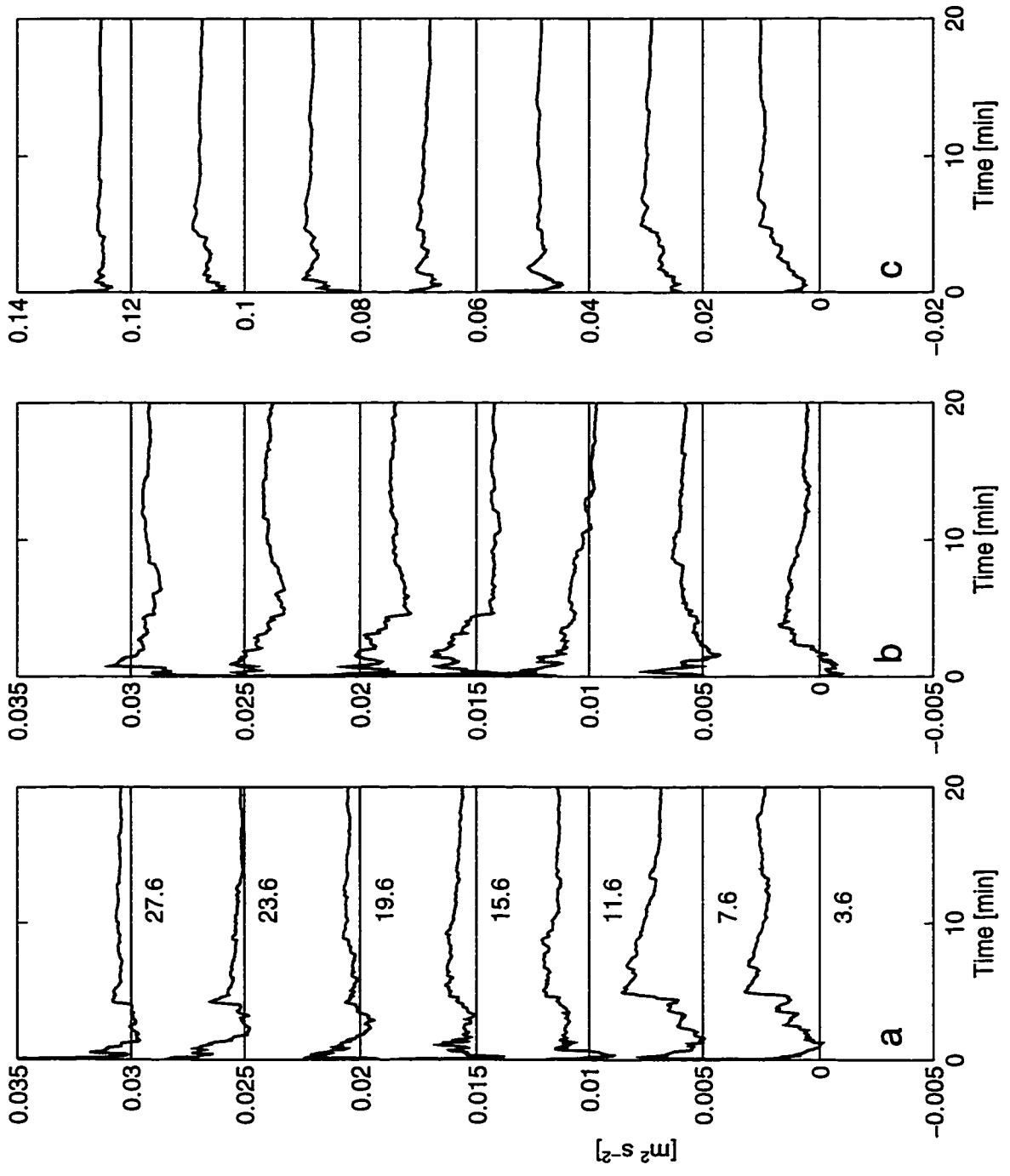

Figure 4.26: The cumulative means of (a) $b_2'^2 - b_1'^2$, (b) $b_4'^2 - b_3'^2$, and (c) $b_1'^2 + b_2'^2 + b_3'^2 + b_4'^2 - 5 \times 10^{-4}$ m^2 s^{-2} for the 20-min interval of data during the strong ebb. In each panel the lowest curve corresponds at z=3.6m and the upper curves at upper levels (indicated by the numbers below the horizontal lines) with the magnitudes of the quantities offset by uniform intervals.

(panel (b)). Note that z = 11.6 m is also the height at which the vertical profile of the cross-channel stress changes sign. For $b_1'^2 + b_2'^2 + b_3'^2 + b_4'^2 - 5 \times 10^{-4}$ m^2 s^{-2} , the cumulative means become constant after 5 mins of averaging at all levels (panel (c)). Note that during this interval $\overline{b_1'^2} + \overline{b_2'^2} + \overline{b_3'^2} + \overline{b_4'^2} - 5 \times 10^{-4}$ m^2 s^{-2} is nearly uniform throughout the profiling range.

Both Doppler noise and turbulent fluctuations contribute to the uncertainty in an estimated quantity. Assuming the level of Doppler noise to be constant, the statistical uncertainty should be constant in a weak turbulent environment. This case is reached for $S < 10^{-4}$ m^2 s^{-2}, as shown in Fig. 4.20 and Eq. (4.20). As turbulent intensity increases, turbulent fluctuations dominate over Doppler noise, the absolute fluctuating levels of the cumulative means increase with increasing turbulence intensity. Hence, the 95% significance levels of stress estimates grow with increasing S, but less rapidly than the stress itself. Thus, the relative uncertainty $|\Delta_{95}|/|\overline{u'w'}|$ decreases with increasing stress magnitude.

4.5 The spectra of turbulence

The spectra of the Reynolds stress and S are obtained by subtracting and adding the spectra of beam velocities, according to (4.8) - (4.10). A bias due to Doppler noise is contained in the spectra of S, but not in the spectra of the Reynolds stress, assuming that the noise levels of the two beams in a pair are the same.

We first choose an interval of 90-min data (starting at day 23.91 during the strong ebb) with nearly stationary turbulent fluctuations to compute the spectra. Fig. 4.27 shows the spectra of the along- and cross-channel components of the Reynolds stress and the spectra of S at 7 heights. The horizontal axis in this figure is the wavenumber k calculated with the streamwise velocity at each height using Taylor's frozen turbulence hypothesis. Each spectrum, calculated with an FFT length of 20 min and 50% overlap, is averaged over 20 evenly distributed intervals in the $\log_{10} k$ domain to

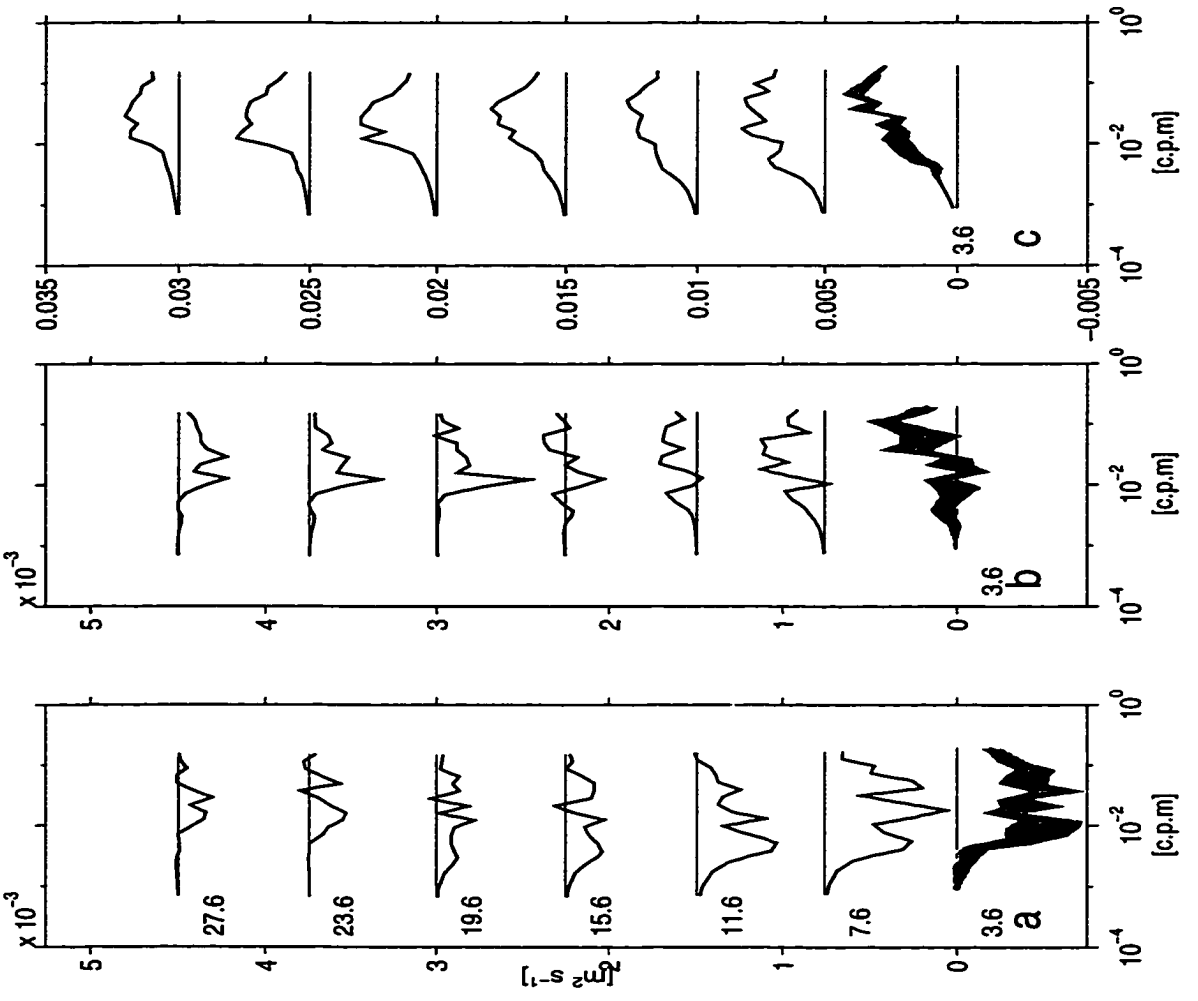

Figure 4.27: The spectra for (a) along- and (b) cross-channel components of Reynolds stress and (c) S, for a 90-min data during the strong ebb. The measurement heights corresponding to each curve are indicated by the numbers in panel (a). The shading areas around the lowest curve in each panel are 95% confidence intervals of the spectral estimates.

increase the statistical certainty of the spectral estimates. A uniform level of 3×10^{-3} $m^2\ s^{-1}$, corresponding to a bias of 5×10^{-4} $m^2\ s^{-2}$ in the estimates of S, is removed from the spectra of S.

The signs of both components of the Reynolds stress spectra do not change over the resolved wavenumber range, except only at one depth (z=15.6 m) for the cross-channel stress, where the the level of the stress spectra is low. The signs of the cross-channel stress spectra change from positive below mid-depth to negative above mid-depth, and this change corresponds to the change of sign of the transverse shear (Fig. 3.16). The wavenumber ranges contributing to the Reynolds stress spectra are fully resolved (panels (a) and (b)). The spectra of S are also resolved, except at the high-wavenumber end for heights less than 7.6 m. Below mid-depth, there is a noticeable shifting of the peak of the spectra toward the low-wavenumber end with increasing distance from the seabed. An analysis of the other 90-min data, starting at day 24.15 and during the strong flood, obtains similar spectra for the along-channel stress and S, as shown in Fig. 4.27. Whereas the spectra of the cross-channel stress are not significantly distinguishable from zero because the magnitudes of this stress component are small.

The turbulence spectra calculated for each 20-min interval are subject to larger uncertainties than those shown in Fig. 4.27 due to the smaller degrees of freedom. It is interesting to seek a scaling for the spectra and to examine the statistics. Measurements in the atmospheric boundary layer (e.g., Kaimal et al. 1972) have found that the proper scaling for wavenumber is the measurement height, z, and that for spectral level is the surface (or bottom) kinematic stress, i.e., the square of surface friction velocity u_*. Measurements in the oceanic boundary layer near the seabed, see Soulsby (1977, 1983), also supported the z-dependent scaling of wavenumber, but found that the spectral level is better scaled by the local magnitude of the stress. Following Soulsby, we introduce the non-dimensional wavenumber $k_* = kz$ (k in c.p.m.)

and the non-dimensional wavenumber-weighted spectra, $k(E_{wu})_s / \int (E_{wu})_s dk$, for the along-channel stress. We find that the scaling of wavenumber by z applies best to levels below the height of log-layer obtained from a fit to the streamwise velocity profiles (Chapter 5). Fig. 4.28 shows the average of the non-dimensional Reynolds stress spectra for 1-day data and the 95% confidence intervals of the mean spectrum obtained with a bootstrap method. We have excluded the spectra with total variances less than 2.25×10^{-4} m^2 s^{-2}, i.e, the local friction velocity less than 0.015 m s^{-1}, because the signal-to-noise ratios of these spectral estimates are small. The averaged non-dimensional spectrum is compared to that obtained from atmospheric boundary layer by Kaimal et al. (1972) under neutral stable conditions. The shapes of both spectra are quite similar, except that the peak of our spectrum is shifted to higher wavenumber by a factor of 2.5. The reason for this shifting in spectral peak is unknown. In contrast, the spectra obtained from near-bottom measurements peaked at the same wavenumber as those of Kaimal et al. (Soulsby 1977).

The spectral range contributing to Reynolds stress lies between 10^{-3} and 2 in terms of k_z, with the peak around 0.3 from our analysis. This means that in the frequency domain, the spectral range contributing to Reynolds stress is between $(0.01 \sim 2)U/z$, with U being the flow speed. Hence the sampling rate required to obtain estimates of Reynolds stress increases with increasing flow speed and decreasing height. The highest sampling rate of the ADCP used in this study is 1.3 Hz, which is sufficient to resolve the Reynolds stress spectra in flows of 1 m s^{-1} and at heights over 2 m above bottom. For 4-ping averaged data, the spectra at z=3.6 m are nearly resolved. In the regions closer to bottom, a higher sampling rate is required.

Kaimal et al.(1972) also established the scaling of TKE density by the bottom stress. However, we find that their scaling does not apply to the spectra of S, in fact the level of the averaged non-dimensional spectra of S is higher than that of Kaimal et al. by a factor of 5, which cannot be explained by even considering the difference

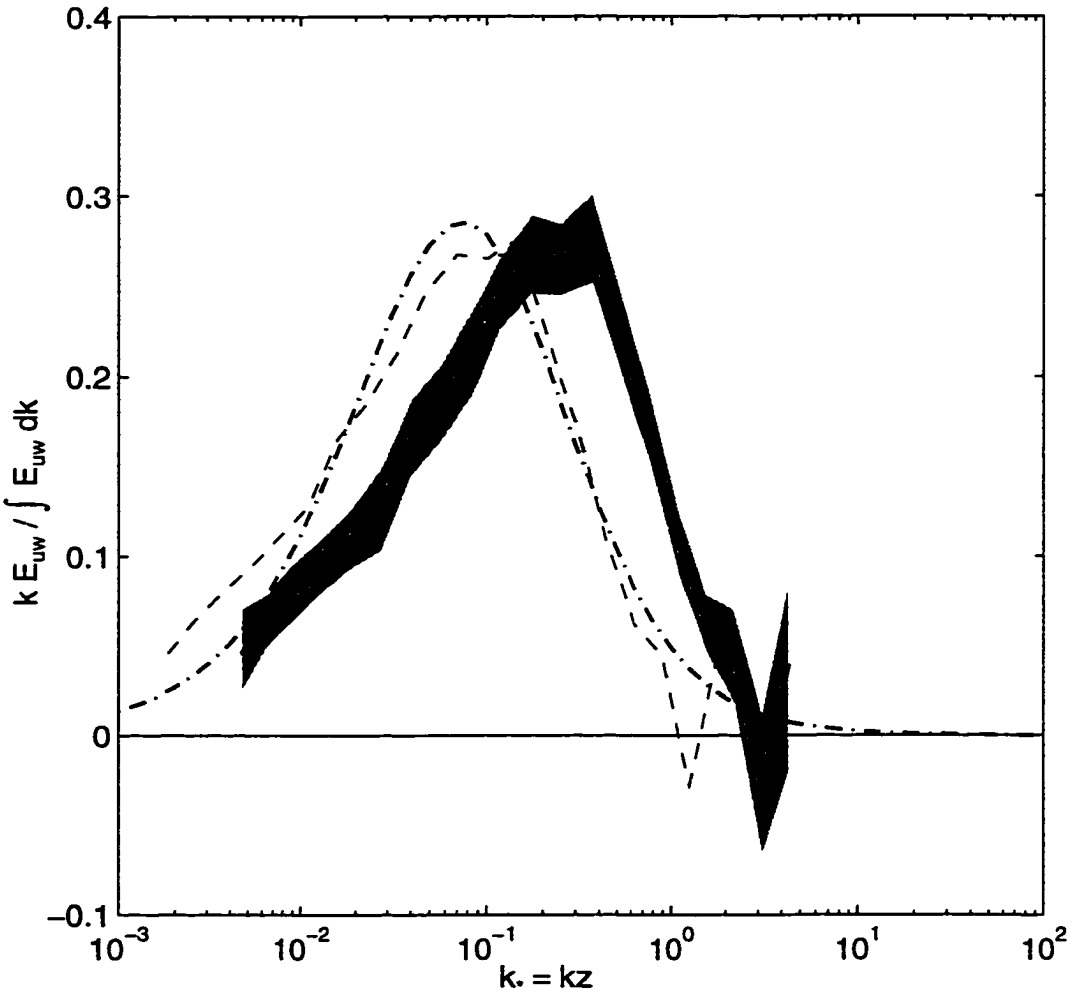

Figure 4.28: The wavenumber-weighted non-dimensional spectrum (solid line) for the along-channel Reynolds stress, $k(E_{wu})_s / \int (E_{wu})_s dk$, v. non-dimensional wavenumber $k_* = kz$ (k in c.p.m.), averaged for the spectra at levels within the log-layer. The individual spectra are calculated for each 20-min intervals, and those with total variances less than 2.25×10^{-4} m^2 s^{-2} are excluded. The shaded area is the 95% confidence interval of the mean spectrum. The dashed line is the averaged spectrum with k_* reduced by a factor of 2.5. The dot-dashed line is the non-dimensional spectrum of Kaimal et al. (1972) under neutral conditions.

between S and $q^2/2$. Obviously, more measurements are required to establish the similarity of the spectra from atmospheric and oceanic boundary layers.

4.6 Estimates of turbulent quantities

In this section, we present the estimates of Reynolds stress and TKE density (obtained with the variance technique) and two more quantities, the TKE production rate P and the vertical viscosity coefficient A_v (derived from stress and the mean flow shear). Fig. 4.29 shows the depth-time sections of these quantities over 1-day period, covering two cycles of the dominant tidal constituent, M_2. Changes in the direction of the tidal flow correspond to sign changes of the along-channel stress (panel (a)) at levels close to the bottom, positive $(-\overline{u'w'})_s$ during the flood and negative during the ebb.

a. Reynolds stress

The two upper panels in Fig. 4.29 show the local friction velocities u_{*s} and u_{*n}, which are related to the along- and cross-channel components of the Reynolds stress by (4.17) and (4.18). First of all, we note that the extremely large stresses obtained during the flow turning in direction, e.g., the events around day 24.05, 24.35, 24.55, are unreliable because neither the flow nor turbulence is stationary (section 4.4). In fact these large stresses usually have opposite signs to the shear, as indicated by the negative production rate (blank areas in panel (c)). During the weak flood between day 24.6 and 24.8, the magnitudes of both u_{*s} and u_{*n} are small, less than 0.01 m s^{-1} in general.

Excluding the extreme events during the tide turning in direction, the along-channel stress intensifies at levels close to the seabed, where the tidally-varying signal is evident. At z=3.6 m, u_{*s} reaches 0.04 m s^{-1} at peak flow during the ebb, and 0.03 m s^{-1} at peak flow during the flood. Away from the bottom, the magnitudes of the stress decrease. Panel (a) also shows the height of the log-layer obtained by a

least-squares fit to the streamwise velocity profiles (Chapter 5). It is seen that the signs of u_{*s} are uniform below the log-layer height, but may change at the top and above of the log-layer.

The cross-channel stress is small during the flood, with the magnitude of u_{*n} about 0.01 m s^{-1} in general throughout the water column. During the ebb, the magnitude of u_{*n} reaches 0.03 m s^{-1} at strong flows. The cross-channel stress changes sign at mid-depth during the ebb, pointing to the headland in the upper layer and away from it in the lower layer. This flood-ebb asymmetry in terms of cross-channel stress corresponds to the asymmetry we found for the transverse shear, which is related to variations in the strength of the transverse flow (Chapter 3).

b. TKE production rate

The TKE production rate is calculated from the two components of the Reynolds stress $(\overline{-u'w'})_s, (\overline{-u'w'})_n$ and the corresponding mean flow shear $\partial u_s/\partial z, \partial u_n/\partial z$, according to

$$P = (\overline{-u'w'})_s \frac{\partial u_s}{\partial z} + (\overline{-u'w'})_n \frac{\partial u_n}{\partial z}. \tag{4.23}$$

The depth and time variations of P are shown in Fig. 4.29c. Negative estimates of P are blank areas and occur mostly during flow turning and the weak flood when the stress estimates are unreliable. In general, the TKE production rate intensifies toward the seabed, bearing the character of wall-bounded turbulence. The major region of TKE production is within the log-layer. However, during the ebb, there are events of large production rate that occur at heights above the log-layer. These events correspond to the sign reversal of stress (and shear) above mid-depth. The magnitudes of P span about 3 decades, ranging from 10^{-4} m^2 s^{-3} (W kg^{-1}) at levels close to bottom and down to 10^{-7} m^2 s^{-3} (which may close to the noise level of P) during the weak flood. The variations with tidal flow is most evident at levels close to the seabed.

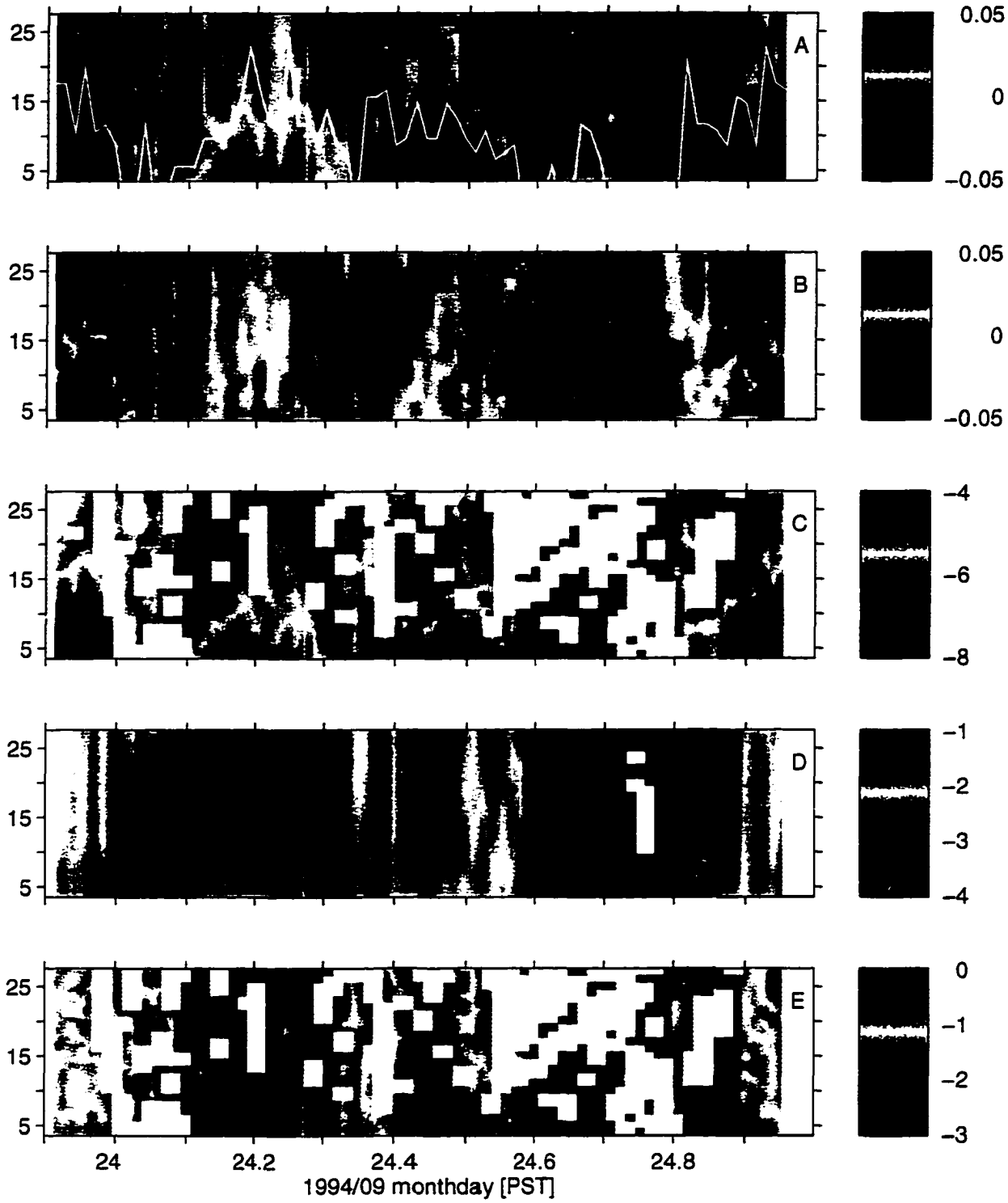

Figure 4.29: Depth-time sections of the 20-min mean local friction velocities (a) u_{*s}, (b) u_{*n} (m s^{-1}), (c) $\log_{10} P$ (m^2 s^{-3}), (d) $\log_{10} S$ (m^2 s^{-2}), and (e) $\log_{10} A_v$ (m^2 s^{-1}). The blank areas in (c), (d) and (e) are where negative values of the corresponding quantities are obtained. The white curve in panel (a) denotes the height of the log-layer (m).

c. TKE density

The quantity S, relating to the TKE density $q^2/2$ by (4.11), is illustrated by panel (d) in Fig. 4.29. A uniform bias of 5×10^{-3} m^2 s^{-2} (the level of bias for 4-ping averaged data) has been removed from S calculated with (4.10). The blank area around day 24.75, during the weak flood, corresponds to negative S, indicating that the bias may not have been as large as 5×10^{-3} m^2 s^{-2} at that time. S is smallest during the weak flood, about 1×10^{-4} m^2 s^{-2} (close to the 95% confidence interval of S, see Table 4.1). The largest estimates of S are obtained at the beginning and end of the ebb, reaching $10^{-2} \sim 10^{-1}$ m^2 s^{-2}. During the strong flood between day 24.1 and 24.3, and in the middle of the ebb around day 24.45, S is about $10^{-3} \sim 10^{-1}$ m^2 s^{-2}. The variation of S with depth for a single profile does not exceed 1 decade. The magnitude of S increases slightly toward the seabed between day 24.1 and 24.3 during the strong flood.

The magnitudes of S are proportional to those of the Reynolds stress by a factor of 10 (Eq. 4.21). From (4.11), we know that for a moderate level of isotropy $\alpha = 0.2$, S overestimates $q^2/2$ by a factor of 1.8. If this is the case, then from (4.21) we have $q^2/2 = 5.6|-\overline{u'w'}|$, which is close to what Gross and Nowell (1983) got from measurements in the near-bottom region of tidal boundary layer.

d. Turbulent viscosity

In principle, an estimate of the vertical viscosity coefficient A_v can be readily obtained from one component of Reynolds stress and the corresponding shear, i.e.,

$$A_v = (\overline{-u'w'})_s / (\frac{\partial u_s}{\partial z}), \tag{4.24}$$

or

$$A_v = (\overline{-u'w'})_n / (\frac{\partial u_n}{\partial z}). \tag{4.25}$$

Alternatively, A_v can be calculated from the TKE production rate and the magnitude of shear, i.e.

$$A_v = P/\left[(\frac{\partial u_n}{\partial z})^2 + (\frac{\partial u_s}{\partial z})^2\right]. \tag{4.26}$$

By using (4.26), the sign of A_v is the same as P. In the optimal case, the estimates from (4.24), (4.25) and (4.26) should be consistent, and this is found to hold statistically for the present dataset. The estimates of A_v are subject to large uncertainties, particularly when the magnitudes of the shear are small. Fig. 4.29e indicates a variation of A_v with tidal flow, ranging from about 10^{-3} m^2 s^{-1} during the weak flood to 0.1 - 0.3 m^2 s^{-1} during the ebb. During the strong flood between day 24.1 and 24.3, A_v is about 0.03 m^2 s^{-1}. The turbulent viscosity increases with increasing height in the lower half of the water column, and reaches a maximum near mid-depth.

4.7 Summary

The variances of the along-beam velocities from a standard ADCP with four beams provide estimates of two components of the Reynolds stress and a quantity proportional to the turbulent kinetic energy density. To apply this "variance technique" one needs to assume that the mean flow and the second-order moments of turbulent velocity fluctuations are statistically homogeneous in horizontal space over the distances separating the beams. The ADCP needs to be rigidly mounted for turbulence measurements to avoid contamination due to correlation of instrument motions and turbulent velocity fluctuations. Doppler noise brings a bias to the estimate of TKE density, but not to stress estimates if the noise standard deviations of the two beams in a pair are identical. For a four-beam unit, terms involving pitch and roll angles are dropped from the calculation algorithm and, thus, there is a bias that is only negligible for small tilt angles.

The uncertainty levels of the stress estimates are mainly due to turbulent fluctuations, and increase with increasing turbulent intensity. The influence of Doppler

noise emerges when turbulent intensities are low. The highest signal to noise ratio is obtained at levels close to the seabed, where the stress magnitudes are large. Velocity fluctuations at periods longer than 20 mins make little contributions to the estimates of Reynolds stress and TKE density. The spectral ranges of the Reynolds stress and TKE density are usually resolved. Within the log-layer, the spectral range of the Reynolds stress lies between $(0.01 \sim 2)$ in terms of the non-dimensional wavenumber $k_* = kz$ (k in c.p.m.), or $(0.01 \sim 2)U/z$ in frequency. domain. The average non-dimensional Reynolds stress spectrum takes the same shape as that from atmospheric boundary layer and near-bottom region in tidal boundary layer, except that the peak of our spectrum is shifted to higher wavenumber by a factor of 2.5.

The combination of the Reynolds stress and mean shear provides estimates of TKE production rate and the vertical eddy viscosity coefficient. Excluding intervals during the turning of the tide and flow separation from the headland, measurement results describe the depth and time variations of turbulence forced by a tidal flow in the channel. The Reynolds stress shows a clear tidal signal in the near-bottom layer for the along-channel component, and presents a clear ebb-flood asymmetry in the cross-channel component. The TKE production rate is bottom-enhanced, ranging from 10^{-4} m^2 s^{-3} (W kg^{-1}) during strong flows to 10^{-7} m^2 s^{-3} during weak flows. The TKE density is approximately proportional to the stress magnitude. The eddy viscosity increases with increasing flow speed, and also with increasing height in the lower half of the water column.

Chapter 5

The Logarithmic Layer

5.1 Introduction

The oceanic boundary layer above the seabed is where the flow shear is large and the frictional effect is enhanced. The structure of this boundary layer bears many similarities with that in the atmosphere and the laboratory. For example, it is generally believed that a log-layer occupies a portion of the boundary layer, where the velocity increases logarithmically with the height above the seabed. The log-layer lies below a height at which the effect of the earth's rotation begins to be important. At the same time, it lies above a thin "bed layer" within which the dynamics may vary depending on the relative importance of molecular viscosity and bottom roughness (Bowden, 1978; Soulsby, 1983).

Identifying the existence of a log-layer is important because it provides one way to estimate the bottom stress, τ, the drag exerted on the flow by the seabed. In a log-layer the expected velocity profile is

$$U(z) = \frac{u_*}{\kappa} \ln\left(\frac{z}{z_o}\right), \tag{5.27}$$

where U is the ensemble mean velocity (averaged sufficiently to eliminate turbulent fluctuations), z is the height above the seabed, κ is von Kármán's constant, z_o is a length scale reflecting the bottom roughness, and u_* is the friction velocity that scales the turbulent velocity fluctuations. The bottom stress is related to u_* by

$$\tau = \rho u_*^2, \tag{5.28}$$

where ρ is the density of seawater. Using (5.27) to estimate the bottom stress is

called the "profile method", which has the practical advantage of requiring only the mean velocity profiles. The laboratory technique of directly measuring the drag force by mounting force transducers to solid boundaries is usually not practical for geophysical flows. Other methods of estimating the bottom stress require measuring and recording the velocity fluctuations at turbulent scales. For example, the "eddy correlation" method (e.g. Heathershaw, 1976), which obtains estimates of the Reynolds stress, requires measurements of velocity fluctuations at the energy-containing scales of turbulence; while the "dissipation method" (e.g. Dewey and Crawford, 1988) derives the bottom stress from the dissipation rate of turbulent kinetic energy, which requires measurements at the dissipation scales. In using the dissipation method the existence of both a log-layer and a constant-stress-layer is assumed.

One determines a drag coefficient C_D from the measured flow and the estimated bottom stress. This coefficient is commonly used in numerical models to parameterize the bottom stress from a known reference velocity, U_r, via a quadratic relationship

$$\tau/\rho = C_D U_r^2. \tag{5.29}$$

The shape of the velocity profiles is related to the turbulent momentum transfer, which is also parameterized in numerical models in some fashion, e.g., by introducing the eddy viscosity coefficient. In particular, the eddy viscosity in the bottom layer is usually assumed to increase linearly with height (e.g. Foreman et al., 1995), consistent with the scaling arguments applied to the log-layer. Hence, verification of the actual existence of the log-layer and its height provides a necessary but not sufficient condition to justify the choice of a linearly increasing eddy viscosity profile.

The profile method has been extensively applied to different sites and conditions in oceanographic studies. However, the height of the log-layer and its variation with changes in flow are not well determined from previous measurements. Most of the previous studies were concerned with the near-bottom layer, and measurements using point current meters seldom reach more than 3 m above the bottom. There are a

few reports on using the expendable current profilers (e.g. Johnson et al., 1994a,b; Jones, 1989) or hydrosondes (e.g. Schumann, 1986) dropped from ships. The free-falling profilers are capable of taking measurements through almost the whole water column. However, the statistics of each individual profile is poor, and to reduce the standard deviation requires averaging over many profiles. It is also inconvenient to apply the free-falling profilers for long-term observations.

Measurements using the acoustic Doppler current profiler (ADCP) provides several advantages for the study of ocean boundary layer — it attains the precision of point meters and the vertical resolution of profilers for the mean velocity. The profiling range is sufficient to cover a large portion of the water column in coastal waters. However, the profiling can not cover the near-surface and near-bottom regions due to the size of the ADCP, its mount, a "blanking" distance, and the side-lobe contamination. For bottom-mounted deployments, even with a 90° adaptor, an ADCP cannot make measurements within 2 m of the bottom. The unit we used in this study does not use a 90° adaptor, hence the profiling started 3.1 m above the bottom and the first velocity bin is centered at 3.6 m height. The near-bottom layer has been extensively studied with point current meters, mostly below 3 m (e.g. Grant et al., 1984; Gross and Nowell, 1983, 1985). The objective of our ADCP measurements is to reveal the structure of the boundary layer beyond the near-bottom region. As suggested by scaling arguments, the log-layer height grows with increasing friction velocity and can reach many meters above the bottom. Bowden (1978), for example, gave 10 m as the typical height of log-layer in a flow of 0.4 m s^{-1} with u_* about 0.02 m s^{-1}.

5.2 Log-layer fitting

a. Least-squares fitting

The fitting of measured velocity profiles to the logarithmic form (5.27) is tried to the streamwise component, u_s, in a least-squares sense. The fitting is applied to the "orthogonal" form of (5.27) (cf. Jenkins and Watts, 1968, pp 114-116), i.e.,

$$u_{si} = \frac{u_*}{\kappa}(\ln z_i - \overline{\ln z_i}) + \frac{u_*}{\kappa}(\overline{\ln z_i} - \ln z_o), \tag{5.30}$$

where $i(= 1, \ldots, N)$ is the index of velocity bins involved in the fitting. For (5.30), the estimates of slope and intercept have zero covariance and their confidence intervals are independent. The "error" of the fitting is calculated as the maximum magnitude of the difference between the fitted values of u_s and the observed data at each velocity bin. For a fit to be acceptable we require that this error is less than 1% of the maximum streamwise speed of the bins involved. The "1%" criterion is compatible with the confidence intervals of the mean velocity estimates. The fitting starts by trying the lowest three velocity bins. If the error of the three-bin fit is within the 1% accuracy, then the fourth bin (counted from the lowest bin) is tried; and so on. Fits obtained with extremely large (larger than 0.2 m) z_o values are rejected. The height of the log-layer, h_l, is defined as the maximum height to which acceptable fits can be obtained. Hence the minimum value of h_l, if found, is 5.6 m (the height of the third bin) above the bottom.

Consecutive streamwise velocity profiles covering 12 h (from day 23.97 to 24.4) and the corresponding logarithmic fits are shown in Fig. 5.30. The log-layer can usually be found during strong flow; during weak flow, a fit is usually not possible. The log-layer embraces the layer close to the bottom where the streamwise shear is intensified. The log-layer height varies with tidal flow in accordance with the strong tidal signal in the streamwise shear, and reaches more than half the water depth during strong currents. During the ebb, the growth of the log-layer seems to be limited by the frequent shear

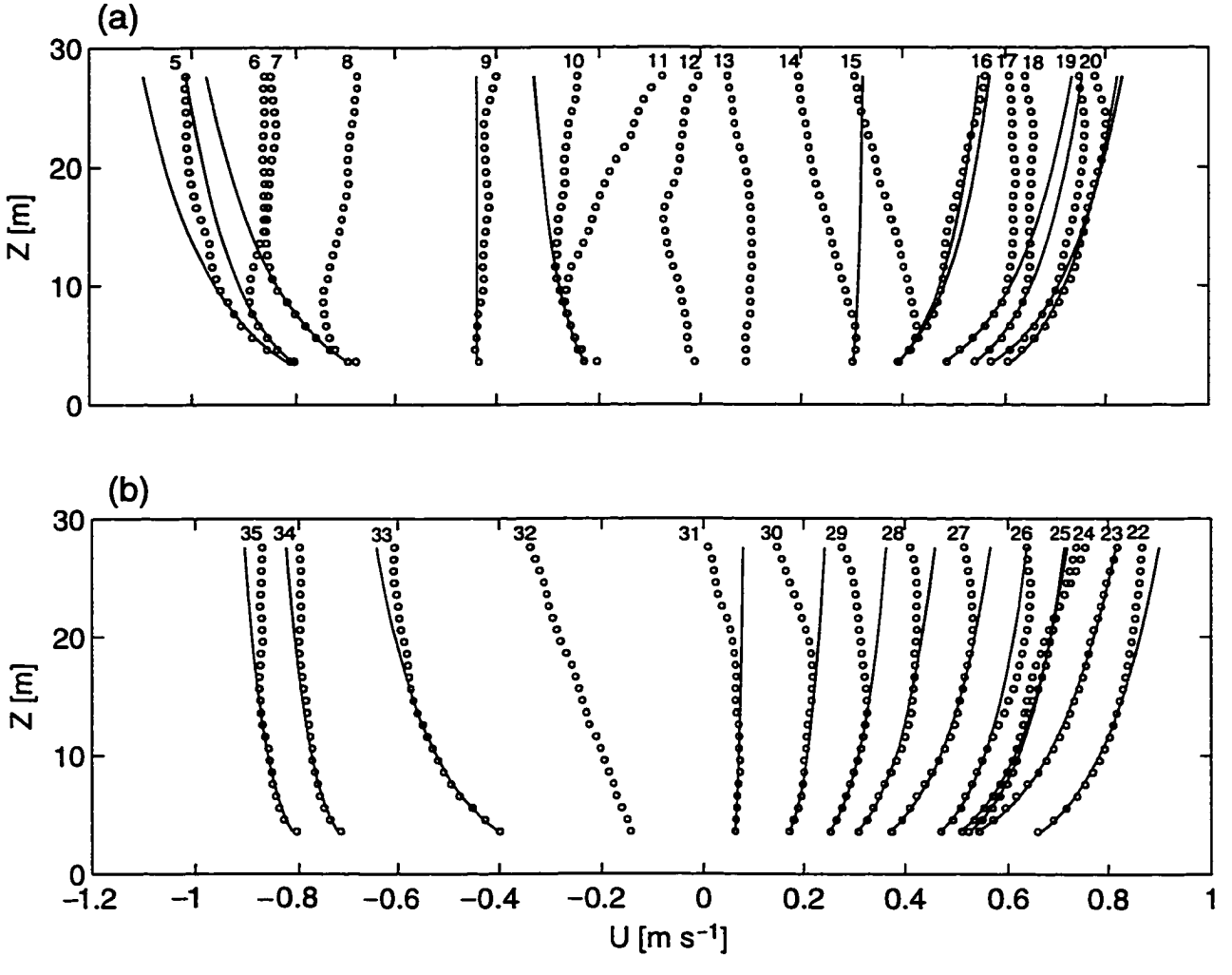

Figure 5.30: Consecutive (spaced by 20 min) profiles of observed streamwise velocity (circles), from (a) day 23.97 (index No. 5) to (b) day 24.40 (index No. 35). The logarithmic fits are plotted as solid lines.

reversals at mid-depth.

The friction velocity and roughness length obtained from the fitting, for 1-day-long data, are plotted in Fig. 5.31. The variation of u_* with the tidal current is obvious, and its magnitude reaches 0.05 m s^{-1} during peak flows. The values of z_o are scattered, but the majority are less than 0.02 m. From the scaling arguments for a boundary layer in a tidal channel flow (see section 5.4), the log-layer exists below a small portion of u_*/ω, where ω is the angular frequency of the dominant tidal constituent. Fig. 5.31(b) shows the comparison of the log-layer heights obtained from the fitting and the values of $0.04u_*/\omega$, where $\omega = 1.4 \times 10^{-4}\mathrm{s}^{-1}$ is the angular frequency of the lunar semidiurnal constituent, M_2. The agreement between the two heights is quite good.

Error bars on the estimates of friction velocity and roughness length are functions of N, the number of velocity bins involved in the fitting and the correlation coefficient, R. Following Jenkins and Watts (1968), the $(1-\alpha)\%$ confidence internals of u_* and z_o are

$$\frac{\delta u_*}{u_*} = \pm\left[\frac{2}{N-2} f_{2,N-2}(1-\alpha)\right]^{1/2}\left(\frac{1}{R^2}-1\right)^{1/2}, \tag{5.31}$$

$$\frac{\delta z_o}{z_o} = \frac{\delta u_*}{u_*}\left[\left(\frac{1}{N}\Sigma(\ln z_i - \overline{\ln z_i})^2\right)^{1/2} + \frac{\kappa\overline{u_{si}}}{u_*}\right], \tag{5.32}$$

respectively, where $f_{2,N-2}$ is the Fisher's F distribution with 2 and $N-2$ degrees of freedom, and R is defined by

$$R^2 = \frac{\left[\Sigma(u_{si} - \overline{u_{si}})(\ln z_i - \overline{\ln z_i})\right]^2}{\Sigma(u_{si} - \overline{u_{si}})^2 \Sigma(\ln z_i - \overline{\ln z_i})^2}, \tag{5.33}$$

where the summation and the means (denoted by overbars) of u_{si} and $\ln z_i$ are taken from $i = 1$ to N. The shaded area in Fig. 5.31(a) shows the 95% confidence intervals for the estimated values of u_*. With typical values of $R^2 = 0.995$, the uncertainty in u_* is $\pm 9\%$ if the log-layer reaches 10 m in height ($N = 8$), and $\pm 6\%$ if the layer is 15

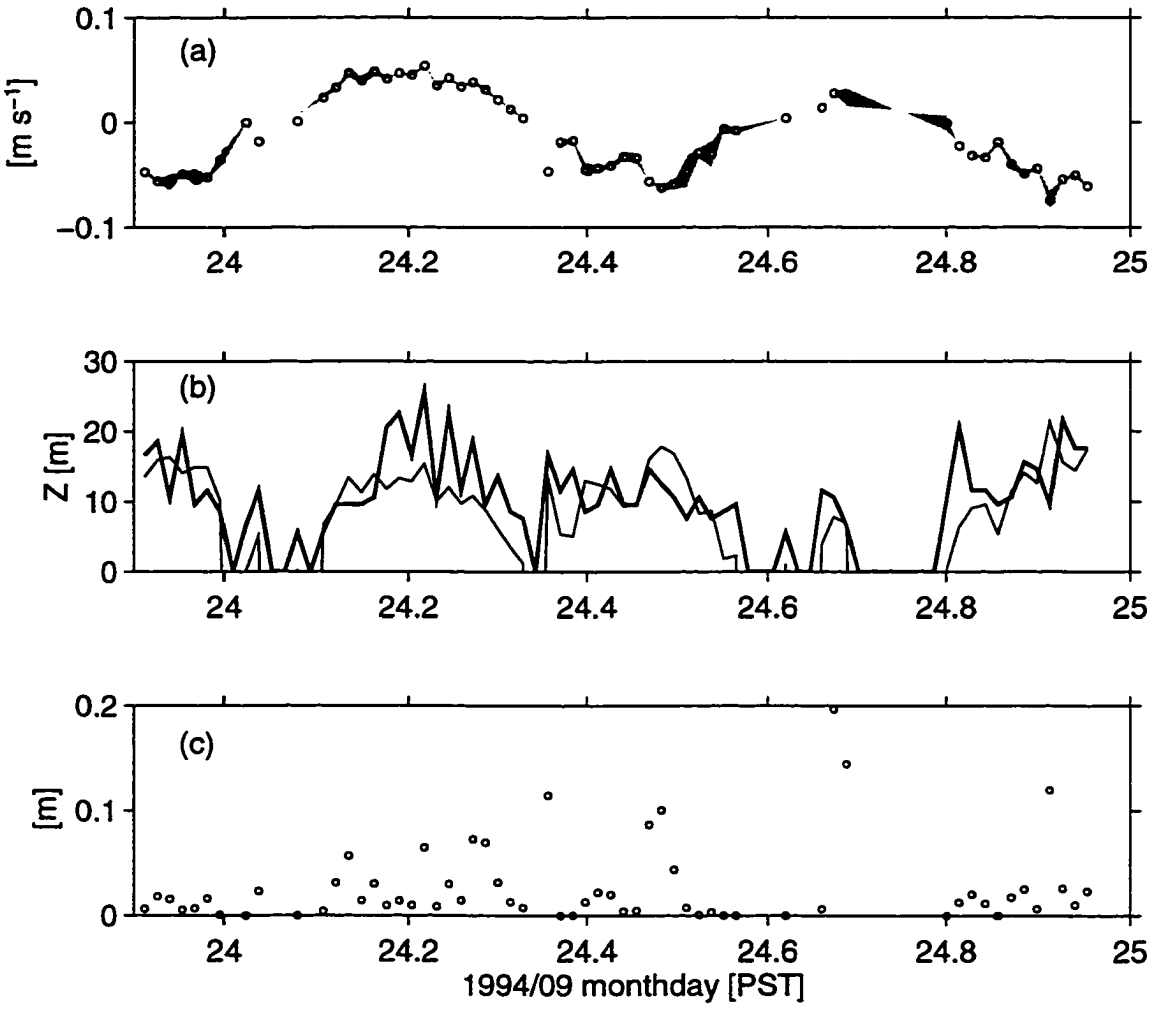

Figure 5.31: Twenty-minute mean velocity profiles showing time variations for (a) friction velocity; (b) log-layer heights from least-squares fits (thick line) v. $0.04u_*/\omega$ (thin line); and (c) roughness length. The shaded area in (a) indicates the 95% confidence interval for friction velocity.

m high ($N = 13$) (all at the 95% confidence level). The error bars for large u_* tend to be small because large friction velocities correspond to large log-layer heights.

As can be seen from (5.32), the confidence interval of z_o equals that of u_* multiplied by a factor $(\Sigma(\ln z_i - \overline{\ln z_i})^2/N)^{1/2} + \kappa\overline{u_{si}}/u_*$. The typical value of this factor is 7, hence the confidence interval of z_o is typically 7 times larger than that of u_*, i.e, $\pm 60\%$ for 10-m high and $\pm 40\%$ for 15-m high log-layers, respectively. The magnitude of this factor increases with increasing $\Sigma(\ln z_i - \overline{\ln z_i})^2$ and $\kappa\overline{u_{si}}/u_*$. Hence, accurate estimates of z_o require measurements close to the bottom.

The fitting was tried to all 306 velocity profiles covering 4.5 days (Fig. 5.32). The variations of the log-layer height and the friction velocity with tidal flow are consistent with the 1-day results of Fig. 5.30. The roughness length is considerably scattered. Unlike Schauer (1987), we do not observe any systematic decrease of z_o with increasing flow magnitude. Fig. 5.33 shows histograms for the log-layer height and z_o. Under the 1% criterion, 227 out of 306 (74%) velocity profiles can be fitted to a log-layer. The remaining 26% have a log-layer height less than 5.6 m, or no log-layer at all; 58% of the log-layers have a height between 5.6 and 15 m, and 16% are above 15 m. The majority (about 70%) of the z_o values obtained are less than 0.05 m, and 33% are less than 0.01 m.

We need to test if the results of log-layer fitting change with the choice of the averaging period used to calculate the mean velocity. Studies of the near-bottom tidal boundary layer tended to choose 10 min as an averaging time (e.g. Soulsby, 1980; Gross and Nowell, 1983). Grant et al. (1984) found that averaging intervals longer or shorter than 10 min tend to increase the scatter in u_* and z_o. The results of repeating the log-layer fitting with 10-min averaged velocity profiles show that both the friction velocity and the log-layer height are consistent with those obtained with 20-min means, and the scatter in z_o remains the same (Fig. 5.34).

Finally, the transverse velocity profiles are nearly linear and not logarithmic.

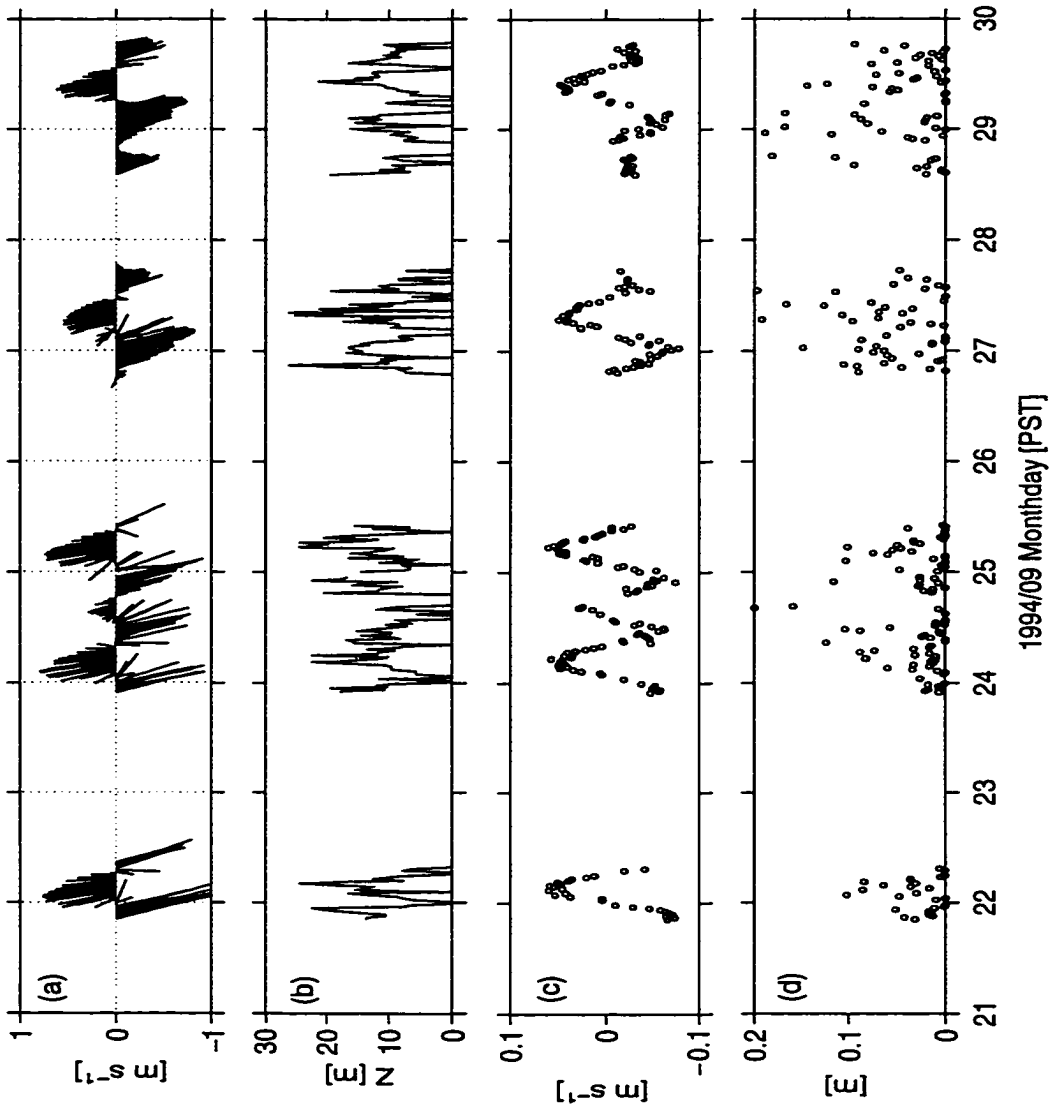

Figure 5.32: Data for 4.5-day showing (a) the depth-mean flow; (b) log-layer height; (c) friction velocity; and (d) roughness length.

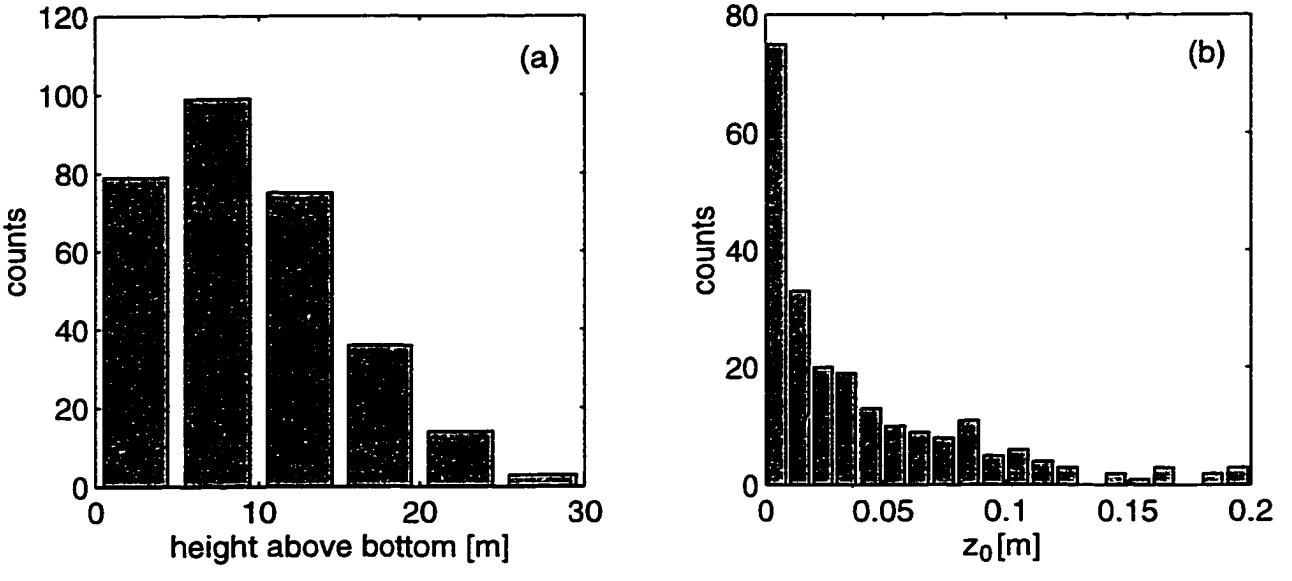

Figure 5.33: Histograms of (a) log-layer height for 306 profiles and (b) roughness length z_o for 227 log-layer fits obtained. The total data covers 4.5 days.

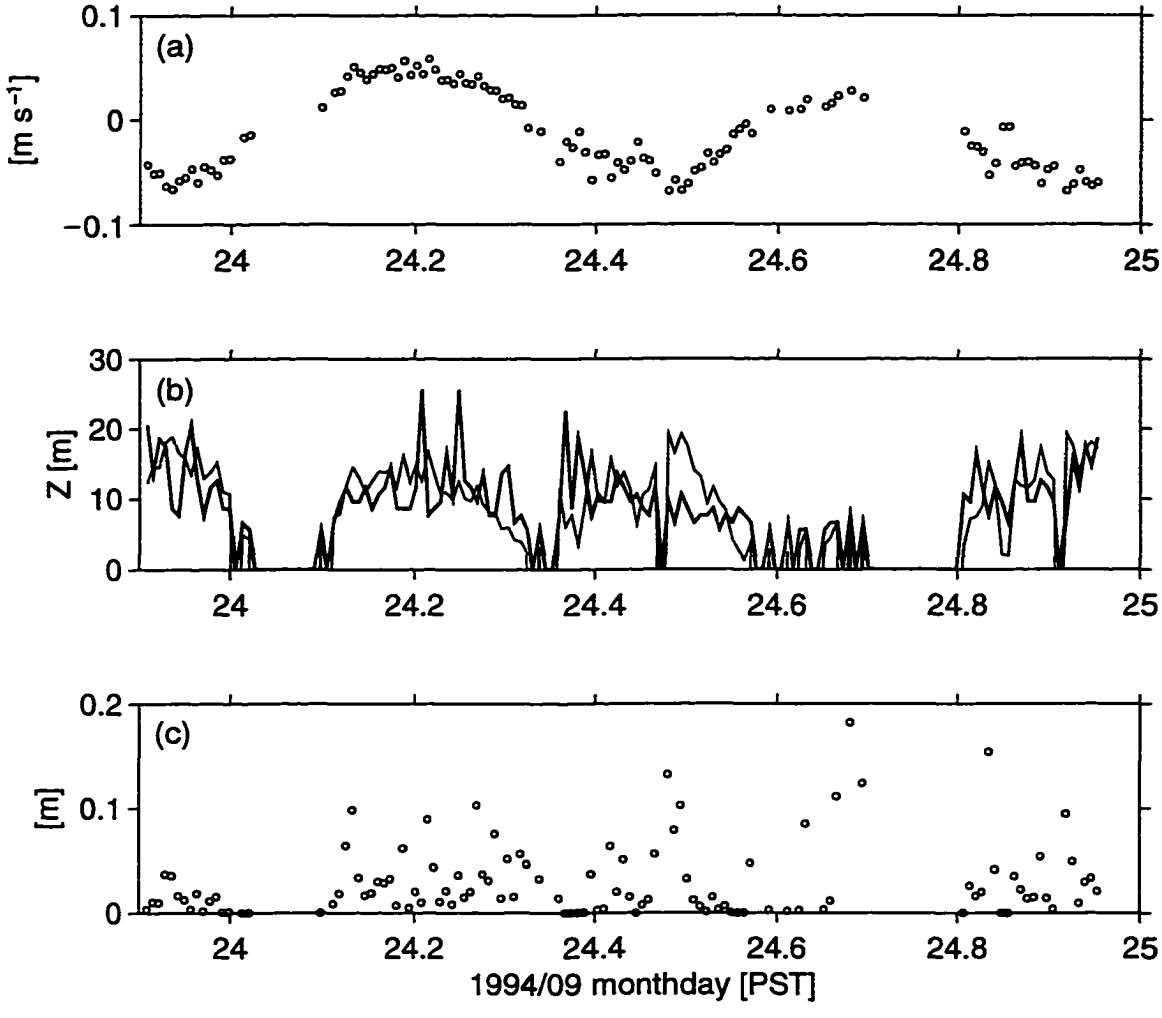

Figure 5.34: Same as Fig. 5.31 except for 10-min mean velocity profiles.

Hence, the transverse component of bottom stress cannot be estimated with the profile method.

b. Scaling of shear in the log-layer

The logarithmic velocity profile expressed by (5.27) and (5.30) is equivalent to

$$\frac{\partial u_s}{\partial z}\frac{\kappa z}{u_*} = 1, \tag{5.34}$$

which means that the streamwise shear can be scaled by $u_*/\kappa z$ and this non-dimensional shear equals unity within the log-layer. Because the statistical uncertainty is much poorer for shear than for velocity estimates, identifying the existence of a log-layer by fitting the shear to (5.34) for each individual profile is difficult. However, the relationship of (5.34) can be examined statistically. Fig. 5.35a shows, for all 227 log-layer fits, the estimates of the non-dimensional shear $(\partial u_s/\partial z)/(u_*/\kappa z)$ against z/h_l, the distance from the seabed scaled by the fitted log-layer height. Ebb and flood are distinguished by setting the ebb values of z/h_l to negative. The values of $(\partial u_s/\partial z)/(u_*/\kappa z)$ are averaged over eight segments of z/h_l for ebb and flood, respectively. These averaged values, with the corresponding 95% confidence intervals obtained using a bootstrap method (Efron and Tibshirani, 1993, Chapter 13), are shown in Fig. 5.35c. During the flood, the averaged non-dimensional shear is statistically indistinguishable from unity throughout the log-layer. In fact, averaging all the values of $(\partial u_s/\partial z)/(u_*/\kappa z)$ for $z/h_l < 1$ gives 0.998, with a 95% confidence interval of ± 0.014. During the ebb, the non-dimensional shear averaged over the segments of z/h_l is close to 1 for $|z/h_l| < 0.8$, but significantly less than 1 for $|z/h_l| > 0.8$. The mean of all the values of $(\partial u_s/\partial z)/(u_*/\kappa z)$ in the range of $|z/h_l| < 0.8$ is 1.012, with a 95% confidence interval of ± 0.016. An alternate way to obtain a profile of the mean non-dimensional shear is to fit a straight line to the points. The fit with the least absolute deviation is illustrated by the straight lines in Figs. 5.35a, b. A straight line of $(\partial u_s/\partial z)/(u_*/\kappa z) \approx 1$ is obtained for $z/h_l < 1$ during the flood, but

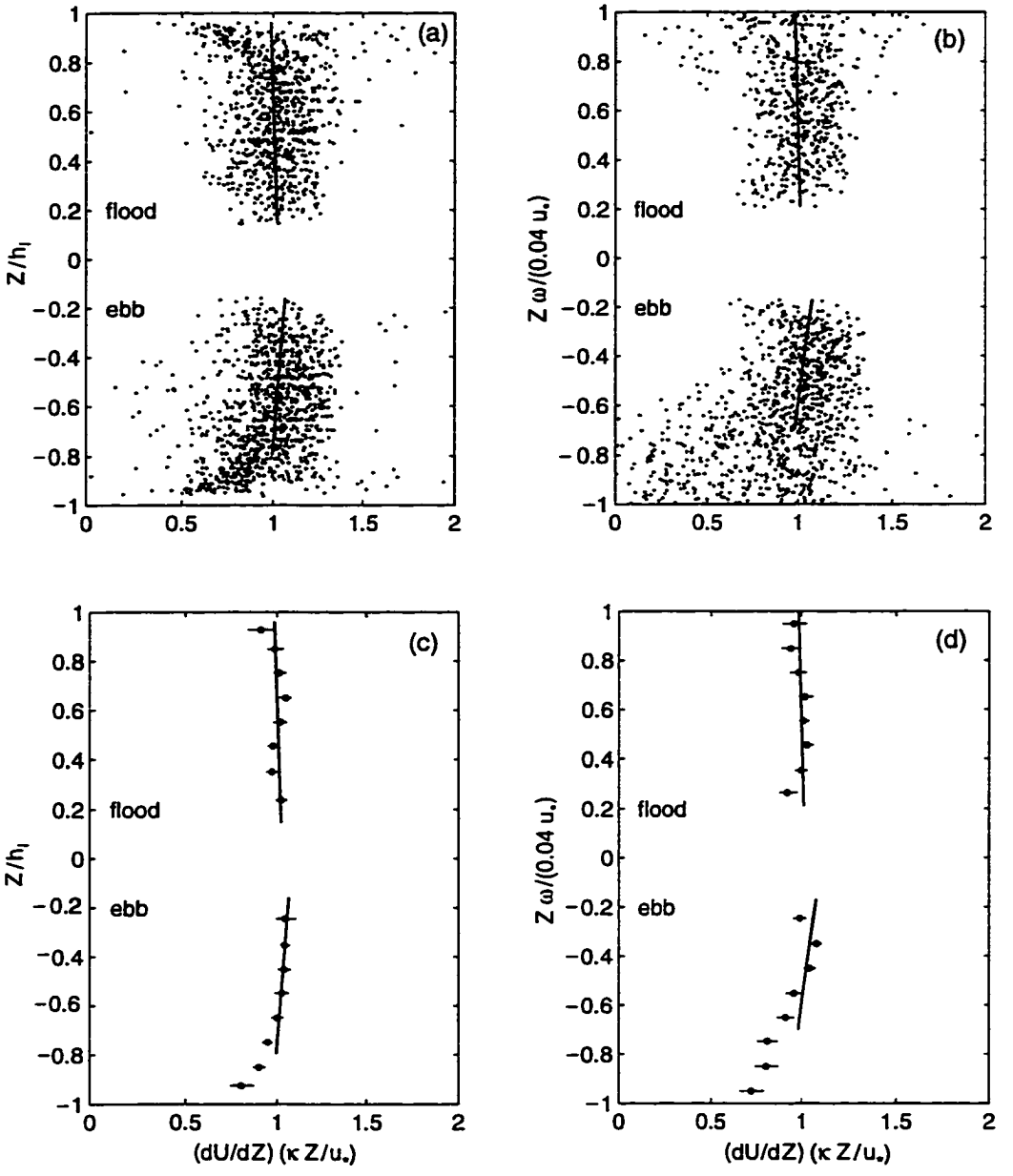

Figure 5.35: Non-dimensional shear $(\partial u_s/\partial z)/(u_*/\kappa z)$ against non-dimensional vertical coordinates z/h_l (a,c) and $z/(0.04u_*/\omega)$ (b,d) for all 4.5-day data. Negative z corresponds to ebb. Open circles in (c) and (d) are the averages of points in (a) and (b) over segments of z/h_l and $z/(0.04u_*/\omega)$; horizontal lines added to the circles show 95% confidence intervals. The straight lines are fitted to the points by the criterion of least absolute deviations. Note that the fitted straight lines are obtained for different ranges in the $y-$axis.

only for $|z/h_l| < 0.8$ during the ebb. Near the top of the log-layer the shear is small, hence small velocity variations that depart from the mean logarithmic profile by less than 1% can still produce large variations in the non-dimensional shear. The statistics of the non-dimensional shear provides a more stringent test of the existence of a log-layer than the fitting of velocity profiles. Thus, the mean non-dimensional shear agrees with its theoretically predicted value of 1 to height h_l during the flood and to $0.8h_l$ during the ebb.

Is it possible to predict the height to which the mean non-dimensional shear equals unity? The distribution of $(\partial u_s/\partial z)/(u_*/\kappa z)$ against $0.04u_*/\omega$ is shown in Fig. 5.35b. The values of $(\partial u_s/\partial z)/(u_*/\kappa z)$ averaged over segments of $z/(0.04u_*/\omega)$ (figure 5.35(d)) are equal to unity at the 95% confidence level up to $z/(0.04u_*/\omega) = 1$ during the flood but only for $|z/(0.04u_*/\omega)| < 0.7$ during the ebb. The straight lines in Figs. 5.35b and d show that the points can be fitted to $(\partial u_s/\partial z)/(u_*/\kappa z) \approx 1$, up to $z/(0.04u_*/\omega) = 1$ for flood and $|z/(0.04u_*/\omega)| < 0.7$ for ebb. Thus, the log-layer height can be predicted as $0.04u_*/\omega$ during the flood, and $0.03u_*/\omega$ during the ebb.

5.3 Estimation of the bottom drag coefficient

The quadratic law of bottom stress expressed by (5.29) is equivalent to

$$u_*^2 = C_D U_r^2. \tag{5.35}$$

Usually, the reference velocity, U_r, is chosen to be either the depth-averaged or a near-bottom (say, at 1 m above the seabed) velocity. The velocity profiles did not cover the whole depth range in our study, hence the depth-mean velocity is not known. Assuming that the log-layer extends to $z = 10$ m, and the velocity remains constant above this height, then for $u_* = 0.05$ m s^{-1}, the mean velocity in a water column 30 m deep is only 0.02 m s^{-1} less than that averaged over the profiling range ($z = 3.1$ to 28.1 m). Hence the velocity averaged over the profiling range, U_m, should be quite

Table 5.2: Bottom drag coefficient ($C_D \times 10^3$) for different reference velocities (U_r) obtained by least-squares fitting in "linear" and "log" scales. The error bars of C_D at the 95% confidence level obtained by least-squares fitting in "linear" and "log" scales. The error bars of C_D at the 95% confidence level are obtained using a bootstrap method.

	U_r	all	ebb	flood
linear	U_m	4.3 ± 0.3	4.2 ± 0.4	4.8 ± 0.4
	$U_{3.6}$	6.1 ± 0.6	5.8 ± 0.8	7.5 ± 0.8
	U_1	9.2 ± 1.4	8.6 ± 1.5	12.5 ± 2.0
log	U_m	3.7 ± 0.3	3.5 ± 0.4	4.0 ± 0.6
	$U_{3.6}$	5.2 ± 0.6	5.0 ± 0.7	5.7 ± 1.0
	U_1	9.4 ± 1.4	8.8 ± 1.7	10.6 ± 2.4

close to that averaged over the total depth. The streamwise velocity at the center of the first bin ($z = 3.6$ m), denoted as $U_{3.6}$, is chosen to be another reference velocity. The log-layer fitting also infers a near-bottom streamwise velocity at 1 m, denoted by U_1, which provides a third choice of reference velocity.

The fitting to (5.35) in a least-squares sense, using all the 227 values of u_* and the three different reference velocities (U_m, $U_{3.6}$, and U_1), gives various estimates of C_D and their 95% confidence intervals, obtained with a bootstrap method. The fitting can be done in the original form of (5.35) or by taking the logarithm of both sides (denoted as "linear" and "log", respectively). We also tried to apply the fit to the 136 values obtained during the ebb separately from the 91 values during the flood. The fitted C_D values are listed in Table 5.2 and the examples of the fitting are shown in Fig. 5.36. The fitting in linear form puts more weight on the larger values of (u_*, U_r) pairs than on the smaller values, whereas the fitting in log form puts more weight on the smaller (u_*, U_r) pairs. From both fits, C_D is estimated to be about 4×10^{-3} with reference to the depth-mean speed U_m, $5 \sim 6 \times 10^{-3}$ with reference to $U_{3.6}$, and 9×10^{-3} with reference to U_1. The difference between flood and ebb in the values of C_D is only marginally significant for the linear case, with the flood values tending to be larger than the ebb values. The difference between ebb and flood is not statistically significant for the log case. Fig. 5.37 shows a time series plot of u_*^2 against $C_D U_m^2$

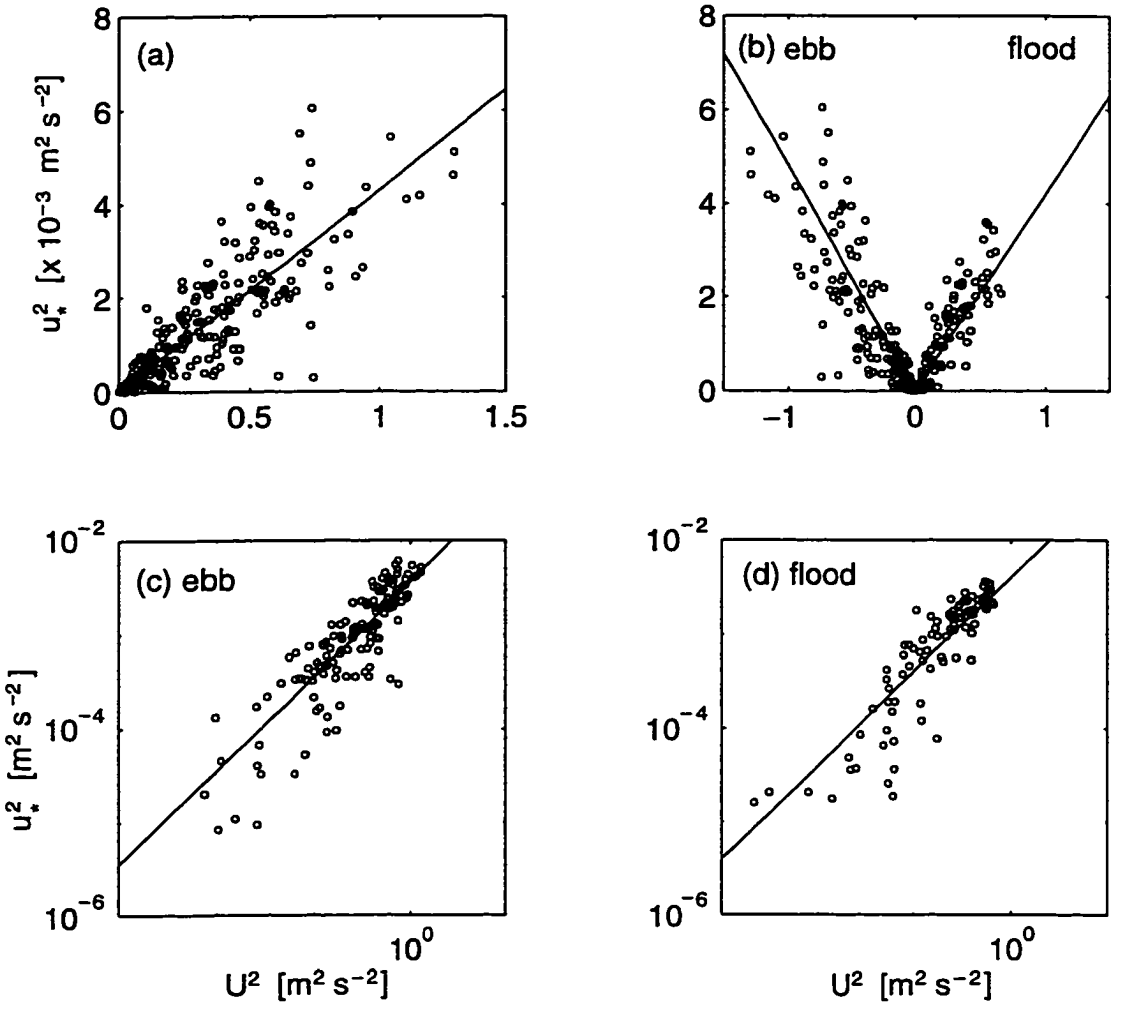

Figure 5.36: Magnitude of bottom stress u_*^2 against U_m^2 (m^2 s^{-2}). U_m is the 20-min mean velocity averaged over the profiling range. (a) and (b) are plotted in linear scales; (c) and (d) are in log-scales. The solid lines have slopes equal to the drag coefficient (C_D) obtained from least-squares fits (see Table 1). In (a) the line is fitted to all the data; In (b), (c) and (d) the lines are fitted to the data from the ebb and the flood, separately.

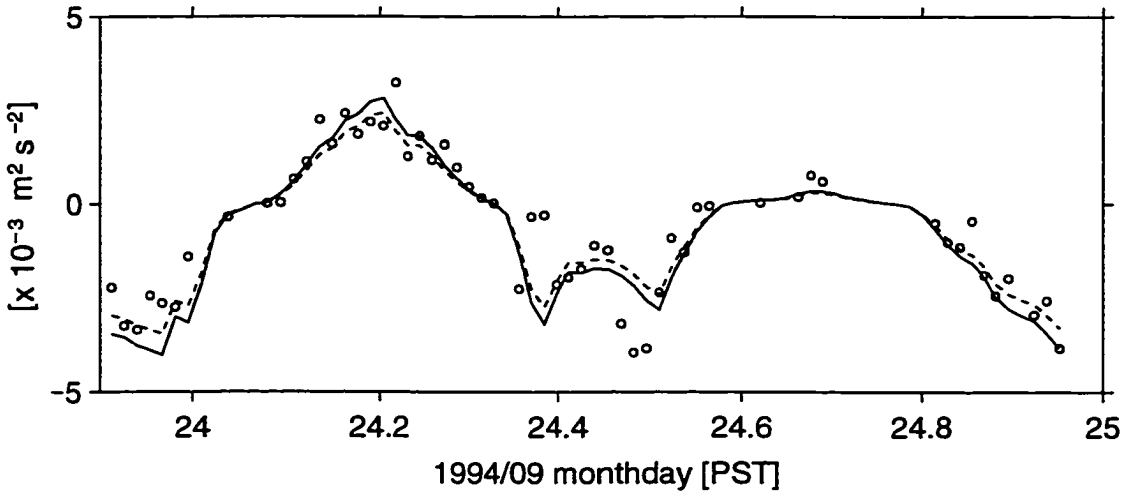

Figure 5.37: Time variation of the magnitude of u_*^2 (circles) and $C_D U_m^2$, with $C_D = 4.3 \times 10^{-3}$ (solid line) and $C_D = 3.7 \times 10^{-3}$ (dashed line).

using two values of C_D, 4.3×10^{-3} and 3.7×10^{-3}, determined from linear and log fits, respectively. It can be seen that $C_D = 4.3 \times 10^{-3}$ is more appropriate during the flood while $C_D = 3.7 \times 10^{-3}$ fits better during the ebb.

5.4 Discussion

a. Interpretation of measurement results

The observed log-layer height in Cordova Channel reaches 20 m above the seabed at peak flow. This is apparently the highest log-layer ever reported from field measurements, although Schumann (1986) observed a log-layer with large standard deviations up to 14–24 m above the seabed, inshore of the Agulhas Current. The high log-layer we observed cannot be connected to skin friction. Skin friction corresponds to a log-layer directly influenced by bottom roughness, hence lies immediately above the "bed layer" and only extends to a small distance from the bottom. For example, the observed log-layer related to skin friction is only 0.1 m high for $u_* \approx 5 \times 10^{-3}$ m s^{-1} on the continental shelf (Chriss and Caldwell, 1982), and less than 1 m high for $u_* \approx 3.5 \times 10^{-2}$ m s^{-1} in a tidal channel (Gross and Nowell, 1983).

Previous studies have found that mechanisms like wave-current interaction, the effect of small-scale topography (bed forms), etc., cause segmented log-layers with the outer log-layer extending farther from the bottom (e.g. Grant and Madsen, 1979; Chriss and Caldwell, 1982). During our measurements in Cordova Channel the wind was weak and waves were insignificant, hence the wave-current interaction was not important. Since the strong and highly turbulent flow conditions in the channel would favor erosion of the seabed and promote the formation of small-scale topography, the high log-layer observed may be related to form drag.

Wide ranges in the magnitudes of the friction velocity and the drag coefficient have been reported in literature (see the review by Soulsby (1983)). The difference between the reported estimates can be attributed to the differences in flow and bed form

conditions. Skin friction varies with the roughness of the seabed, with distinctions between hydraulically smooth, rough, or transitional conditions. The drag coefficient related to form drag can be 4 to 10 times larger than that related to skin friction, as reported by Chriss and Caldwell (1982) on continental shelf measurements. The drag coefficient we obtained is about 2.5 times larger than that estimated by Gross and Nowell (1983) in a tidal channel in Puget Sound, Washington, where the bed forms were believed to be non-existent. Our value of C_D is very close to that obtained by Grant et al. (1984) from the measurements on the continental shelf off Northern California, even though they attributed the log-layer they observed to wave-current interaction.

Our estimates of bottom roughness are quite scattered, but the values are on average larger than required to quantify the roughness of the bed material. Besides the statistical error, other mechanisms that can cause scatter in z_o are wave-current interaction, effect of bed forms, and stratification of suspended sediment (see a recent discussion by Green and McCave, 1995). We lack near-bottom flow measurements and detailed observation of seabed conditions to further address this issue.

b. Scaling arguments of the log-layer

The log-layer occupies only a small portion of the total boundary layer. Clauser (1956) found (from laboratory experiments) that the log-layer extends to 10% of the bottom boundary layer height. The boundary layer height is related to the scalings of the flow fields inside and outside the boundary layer. The tidal boundary layer can be classified as the oscillatory planetary type, and the scaling arguments applied to it were advanced by Soulsby (1983). Because the magnitudes of the tidal frequency and that of the Coriolis parameter are comparable, the scaling arguments for the tidal boundary layer are not as simple as those for purely oscillatory or planetary layers. In the case of "rectilinear free-stream flow" the boundary layer structure

bears similarities to those for a purely oscillatory one. The tidal flow near smooth coastline or in narrow channels is approximately "rectilinear". In such cases, the momentum equation in the streamwise direction is

$$\frac{\partial u_s}{\partial t} + f u_n = -g\frac{\partial \eta}{\partial s} + \frac{\partial}{\partial z}(-\overline{u_s' w'}), \tag{5.36}$$

where η is the free-surface elevation, g the acceleration due to gravity, and f the Coriolis parameter. The density of seawater is assumed to be constant. The time scales for the first term is ω^{-1}, with ω being the angular frequency of the tide. For diurnal and semi-diurnal constituents, $\omega \approx f$, and because u_n is small compared with u_s, the Coriolis term can be neglected. Hence, we can apply the scaling arguments for a purely oscillatory boundary layer, which suggest that the log-layer height is only a small portion of u_*/ω.

Neglecting the nonlinear terms in the momentum equation poses constraints on applying simple scaling arguments strictly to the near-coast and channel flows (Soulsby, 1983). In the case where a strong coastline curvature is present, the curvature forcing drives flow in the transverse direction. In Cordova Channel, the curvature forcing is weak during the flood and strong during the ebb, at the site of the ADCP. Hence, we expect that the simple scaling arguments are more appropriate to the flood than the ebb.

The log-layer height in Cordova Channel is approximately $0.04u_*/\omega$ during the flood and $0.03u_*/\omega$ during the ebb. For the reasons stated above, we take $0.04u_*/\omega$ as generally more applicable to an approximately rectilinear tidal flow near straight coastline and in narrow channels. For a tidal boundary layer in the open sea, more complicated scaling arguments for oscillatory planetary boundary layers apply (Soulsby, 1983). Interestingly, previous studies suggested that the log-layer height for a steady planetary boundary layer is $0.03u_*/f$ (Tennekes, 1973) or $0.04u_*/f$ (Soulsby, 1983).

c. On modifications of the log-layer

In this study, we only tried to fit the measured streamwise velocity to the exact logarithmic profile (5.27). Previous studies of the near-bottom layer in tidal flows frequently reported departures of measured velocity profiles from (5.27), at heights above the "inner log-layer" connected to skin friction (e.g. Chris and Caldwell, 1982; Schauer, 1987). A number of factors, including the acceleration/deceleration of the tidal flow, stratification, wave-current interaction, and bed forms, etc., can cause deviations from the exact logarithmic profile. Efforts have been made to account for these added mechanisms by a "modified" form of (5.27), which usually takes a "log-linear" form (e.g.,Gross et al., 1992):

$$U(z) = \frac{u_*}{\kappa}\left[\ln\left(\frac{z}{z_o}\right) + \beta z\right]. \tag{5.37}$$

The meaning of the new parameter β varies according to the mechanism under consideration. For example, in the scheme proposed by Soulsby and Dyer (1981), β is related to the acceleration/deceleration effect by

$$\beta = -\frac{1}{\gamma}\frac{du_*/dt}{u_*|u_*|}, \tag{5.38}$$

where γ is a constant. The log-linear velocity profile can also be obtained by modifying the mixing length l from a linear variation with z, i.e., $l = \kappa z$, to $l = \kappa z/(1 + \kappa z/L)$, where L is the upper limit of l (Schauer, 1987). Schauer's scheme corresponds to

$$\beta = \frac{\kappa}{L}. \tag{5.39}$$

To account for stratification, β takes the same form of (5.39) except that L is replaced by the Monin-Obukov length and κ is replaced by another constant (Taylor and Dyer, 1977).

These modifications of the log-layer were all proposed to explain the velocity profiles in the near-bottom layer obtained from measurements seldom extending to more than 3 m above the sea bed. Although fitting the observed velocity profiles to

(5.37), which adds one more degree of freedom, is always technically feasible, there are no obvious reasons to apply these modifications to the "outer" layer measured in Cordova Channel. In fact, we can fit (5.37) to the streamwise velocity (with 1% accuracy) to greater heights than we can fit this velocity to (5.27). However, the "log-linear" fits cannot account for the mechanisms in the above listed schemes. In Soulsby and Dyer's scheme, β is negative (positive) during the accelerating (decelerating) phase of the flow. Hence, as the height increases, a log-linear profile has a smaller (larger) velocity and shear than a log-layer profile. In Cordova Channel, the measured streamwise velocity above the logarithmic part is always *smaller* in magnitude than predicted by the log-layer model during *both* the accelerating and the decelerating phases (Fig. 5.30). Hence, the measured profiles are inconsistent with the correction for the effect of acceleration and deceleration. According to the schemes proposed by Taylor and Dyer, or Schauer, β is always positive, and a log-linear profile has a *larger* velocity and shear than (5.27). Thus, modifications of the logarithmic profile to account for stratification and a nonlinear mixing length are also inconsistent with our observation.

The decreasing velocity and shear above the log-layer is more easily explained by the boundary condition of zero stress at the surface and by the entrainment of the shallow water from the shoals of Saanichton Bay. The tight log-layer fits we obtained indicate that the modifications of log-layer model proposed by previous researchers do not apply to the outer layer. It is plausible that the simple scaling arguments leading to the existence of a log-layer apply within both the near-bottom and outer layers, whereas more scales exist in the transition region where modifications of (5.27) may be required.

5.5 Summary

The major contribution of this chapter is the observation of a time varying log-layer in a turbulent tidal channel flow. The fitting of streamwise velocity profiles to the logarithmic form is performed under a 1% criterion in velocity magnitude, which is compatible with the uncertainty levels in the mean velocity estimates. The observed log-layer height reaches 20 m above the seabed during peak tidal flows of 1 m s^{-1}. During the ebb, mid-depth shear reversals, presumably caused by the entrainment of slower waters from the shoals of Saanichton Bay on the western side of the channel, limit the maximum height of the log-layer. This log-layer is not connected to skin friction, but is more likely the result of form drag. The mean profile of the non-dimensional shear, defined as $(\partial U/\partial z)/(u_*/\kappa z)$, is statistically indistinguishable from unity up to 100% (for the flood) and up to 80% (for the ebb) of the log-layer height obtained from profile fitting. Correspondingly, the log-layer height is predicted by $0.04u_*/\omega$ during the flood and $0.03u_*/\omega$ during the ebb, where ω is the angular frequency of the dominant tidal constituent, M_2.

The estimated friction velocity also varies tidally, reaching 0.05 m s^{-1} at peak current flow. The quadratic drag coefficient derived from the friction velocity is 4×10^{-3} with reference to the depth mean streamwise velocity, and is about 6×10^{-3} and 9×10^{-3} with reference to the velocity at 3.6 m and 1 m above the bottom, respectively. The drag coefficient is larger than that connected with skin friction, consistent with the previously reported increasing of drag coefficient over bedforms. Although during the ebb there is considerably more flow curvature, transverse flow and transverse shear, the drag coefficient is statistically indistinguishable between the flood and the ebb. The estimated values of bottom roughness length have a large scatter.

Near the top of the log-layer, both the measured velocity and shear are less than predicted by the log-layer model. This deviation is inconsistent with the effects of

acceleration/deceleration, stratification, and a modified mixing length. The observed deviation from a logarithmic profile can be more easily explained by the zero-stress boundary condition at surface and the entrainment of shallow water from Saanichton Bay.

Chapter 6

Turbulence Characteristics in Cordova Channel

6.1 Introduction

In this chapter, we present an analysis of the turbulent quantities in Cordova Channel from measurements with the ADCP and the moored microstructure instrument TAMI. The measurement results describe the space and time variability of the turbulence and the structure of a tidal boundary layer. The relative importance of the terms to the turbulent kinetic energy (TKE) budget is evaluated; and a parameterization scheme for the rate of dissipation of TKE is tested with the observational data.

There have been minimal turbulence measurements in comparison to the vast pool of mean flow data. The important turbulent quantities of practical interests are the frictional force on the flow, turbulence intensity, and various coefficients describing the mixing efficiency of momentum and scalars. In reality, turbulent quantities undergo complicated variations in space and time. A turbulent boundary layer is formed above the seabed by bottom friction. Within the boundary layer the flow is attenuated, the shear and frictional force are enhanced, and the turbulent kinetic energy (TKE) production is intensified. It is generally believed that the structure of oceanic boundary layer bears many similarities to that in atmospheric and laboratory flows. More measurement evidence, particularly from oceanic boundary layer, is required to convincingly establish this analogy.

Turbulent closure schemes are commonly proposed with scaling arguments, and include constants to be determined from measurements. Mellor and Yamada (1974,

1982) proposed a hierarchy of turbulent closure models for geophysical boundary layer flows, and their level-2.5 version has been implemented in practical modeling of coastal water circulation (e.g. Blumberg and Mellor, 1987; Lynch et al., 1996). The feasibility of this closure scheme and the values of the empirical constants need to be tested with oceanic measurements. Whereas turbulent parameterization can be indirectly tested by the ability of the model to reproduce the time-mean field, a more critical test is the model's ability to describe the depth dependence and time evolution of the turbulence parameters (Simpson et al., 1996).

6.2 Turbulence measurements with the ADCP and TAMI

Measurements with the ADCP provide profiles of two components of the Reynolds stress. the TKE density ($q^2/2$), the rate of TKE production (P), the vertical eddy viscosity coefficient (A_v) (Chapter 4), and the Prandtl mixing length.. The moored microstructure instrument TAMI was deployed twice during the experiment at a nominal depth of 15 m. The turbulent velocity and temperature fluctuations were measured, respectively, by shear probes and fast thermistors mounted on TAMI. The TKE dissipation rate, ϵ, were estimated by fitting the velocity spectra to the theoretical spectra in the inertial subrange (Huang, 1996; Lueck and Huang, 1997). The temperature spectra $\psi(k)$ provide estimates of the weighted-mean temperature spectral level

$$\zeta = \overline{\psi(k) k^{5/3} \epsilon^{1/3}}, \tag{6.40}$$

where the overbar denotes an average over the inertial-convection subrange. The dissipation rate of temperature fluctuation variance, 2χ, is related to ζ by

$$\chi = \zeta/\beta, \tag{6.41}$$

where β is a constant. This constant ranges between 0.35 to 1.15 (e.g. Gargett, 1985). Following Edson et al. (1991), we choose $\beta = 0.79$ in this study.

6.3 Turbulent parameters and closure model

a. Mixing coefficients and mixing length

The effects of turbulence in transferring momentum and in mixing scalars are usually parameterized by introducing viscosity and diffusivity coefficients. From measurements with the ADCP, estimates of the vertical viscosity coefficient A_v are obtained by dividing the observed Reynolds stress with the mean shear. In this analysis, A_v is calculated by dividing the TKE production rate (P) with the squares of the shear magnitude ($\partial U/\partial z$), i.e.,

$$A_v = \frac{P}{(\partial U/\partial z)^2}. \tag{6.42}$$

At mid-depth, the fine- and microstructure measurements made with TAMI provide two estimates of eddy diffusivity coefficient. By assuming that the rate of TKE loss to buoyancy ($B = (g/\rho_o)\overline{w'\rho'}$) is proportional to the rate of TKE dissipation (ϵ), i.e., $\Gamma = B/\epsilon$, the vertical diffusivity for density is derived as

$$K_v^\rho = \frac{\Gamma\epsilon}{N^2}. \tag{6.43}$$

Assuming that the dissipation rate of temperature fluctuation variance, 2χ, is approximately balanced by the variance production rate (Osborn and Cox, 1972), we derive the diffusivity for temperature as

$$K_v^T = \frac{2\chi}{(\partial T/\partial z)^2}. \tag{6.44}$$

The eddy viscosity and diffusivity coefficients are related to the turbulent mixing length. In this study, measurements with the ADCP provide the estimates of the Prandtl mixing length, l_m, which is defined as

$$l_m = \frac{(|\overline{u'w'}|)^{1/2}}{\partial U/\partial z} = \frac{P^{1/2}}{(\partial U/\partial z)^{3/2}}, \tag{6.45}$$

where $|\overline{u'w'}|$ represents the magnitude of the Reynolds stress. In turbulent shear flow, l_m is a characteristic length scale of TKE-containing eddies. At mid-depth, the

observational data from TAMI provide estimates of the Ozmidov length scale,

$$l_O = \left(\frac{\epsilon}{N^3}\right)^{1/2}. \tag{6.46}$$

In stratified flow, l_O characterizes the largest possible overturn that turbulence can accomplish (Turner, 1973).

Both l_m and l_O are macroscales. With the rate of dissipation of TKE available, one can also derive a turbulence microscale, i.e., the Kolmogorov scale

$$l_K = (\nu^3/\epsilon)^{1/4}, \tag{6.47}$$

where ν is the kinematic molecular viscosity. The Kolmogorov scale represents the lower bound on the scales of turbulent motions.

b. The Mellor-Yamada closure model

In the hierarchy of turbulent closure models proposed by Mellor and Yamada (1974, 1982), turbulent viscosity/diffusivity coefficients are parameterized in terms of the turbulent intensity, q, and a turbulent macroscale l, i.e.,

$$(A_v, K_v, K_v^q) = (S_m, S_h, S_q) lq, \tag{6.48}$$

where K_v is the vertical diffusivity for passive scalars (e.g. salinity and temperature), K_v^q is the diffusivity for $q^2/2$, and (S_m, S_h, S_q) are stability functions.

The governing equation for TKE density reads

$$\frac{\partial}{\partial t}\left(\frac{q^2}{2}\right) + \mathbf{u}\cdot\nabla\left(\frac{q^2}{2}\right) - \frac{\partial}{\partial z}\left[K_v^q \frac{\partial}{\partial z}\left(\frac{q^2}{2}\right)\right] = P - B - \epsilon. \tag{6.49}$$

In geophysical boundary layers where the mean flow and density fields vary more strongly with depth than with horizontal distance, the rate of TKE production (P) is related to the velocity shear by (6.42), and the rate of TKE loss to buoyancy (B) is related to local stratification by

$$B = K_v N^2. \tag{6.50}$$

The rate of TKE dissipation (ϵ) is parameterized as

$$\epsilon_{MY} = \frac{q^3}{B_1 l}, \tag{6.51}$$

where B_1 is an empirical constant. The three stability functions were formulated by Galperin et al. (1988) as

$$S_m = \frac{(g_2 - g_3 G_h)}{(1 - g_4 G_h)(1 - g_5 G_h)}, \tag{6.52}$$

$$S_h = \frac{g_6}{(1 - g_4 G_h)}, \tag{6.53}$$

$$S_q = 0.2, \tag{6.54}$$

where

$$G_h = -\frac{l^2}{q^2} N^2, \tag{6.55}$$

and $g_{2,\ldots,6}$ are empirical constants. The values of these empirical constants were determined by appealing to data from the laboratory and the atmosphere under neutral conditions (Mellor and Yamada, 1982).

Mellor and Yamada (1982) proposed an additional equation for $q^2 l$ to determine the mixing length l. For turbulent boundary flows, l is usually prescribed as a function of the distance from the boundary. For example, Simpson et al. (1996) specified l in tidal boundary layer as

$$l = \kappa z \left(1 - \frac{z}{h}\right)^{1/2}, \tag{6.56}$$

where z is the height above the seabed, h the water depth, and $\kappa = 0.4$ is von Karman's constant. By choosing $l = l_m$, the combination of (6.48) with (6.42) gives

$$\frac{|\overline{u'w'}|}{q^2} = S_m^2. \tag{6.57}$$

c. The local TKE balance

In turbulent boundary layers, terms on the left-hand side of (6.49) are usually small compared to terms on the right-hand side, hence (6.49) reduces to a local balance of

P, ϵ and B, i.e.,

$$P = \epsilon + B. \tag{6.58}$$

By introducing the mixing efficiency $\Gamma = B/\epsilon$, or equivalently, the flux Richardson number $R_f = B/P$, we reduce the three-term local balance of TKE to two terms. By combining (6.58) with (6.57), the relationship between the two empirical constants S_m and B_1 is derived as

$$\frac{1}{B_1} = \frac{S_m^3}{1+\Gamma}. \tag{6.59}$$

In stratified oceanic flows, the magnitude of Γ varies between 0.04 and 0.4 (Peters et al., 1995) and is typically $\Gamma \leq 0.2$ (Osborn, 1980).

Under local balance of TKE, equivalent estimates of the Ozmidov and Kolmogorov scales can be obtained by replacing the rate of TKE dissipation (ϵ) with the production rate (P). This gives

$$l_N = \left(\frac{P}{N^3}\right)^{1/2} \sim l_O, \tag{6.60}$$

and

$$l_\nu = (\nu^3/P)^{1/4} \sim l_K. \tag{6.61}$$

For a recent study on the implications of both the macro- and microscales to turbulence generating mechanism in coastal waters, see Stacey et al. (1997).

6.4 Turbulent characteristics in the near-bottom layer

A total of 3.8 days of estimates of the turbulent quantities are obtained from measurements with the ADCP (Fig. 6.38). The depth-time variations of the Reynolds stress, TKE density, production rate, and the eddy viscosity coefficient, are consistent with the 1-day results of Fig. 4.29.

At 3.6 m above the seabed, variations of the TKE density and the magnitude of the Reynolds stress are well correlated (Fig. 6.39a). Both $q^2/2$ and $|\overline{-u'w'}|$ contain

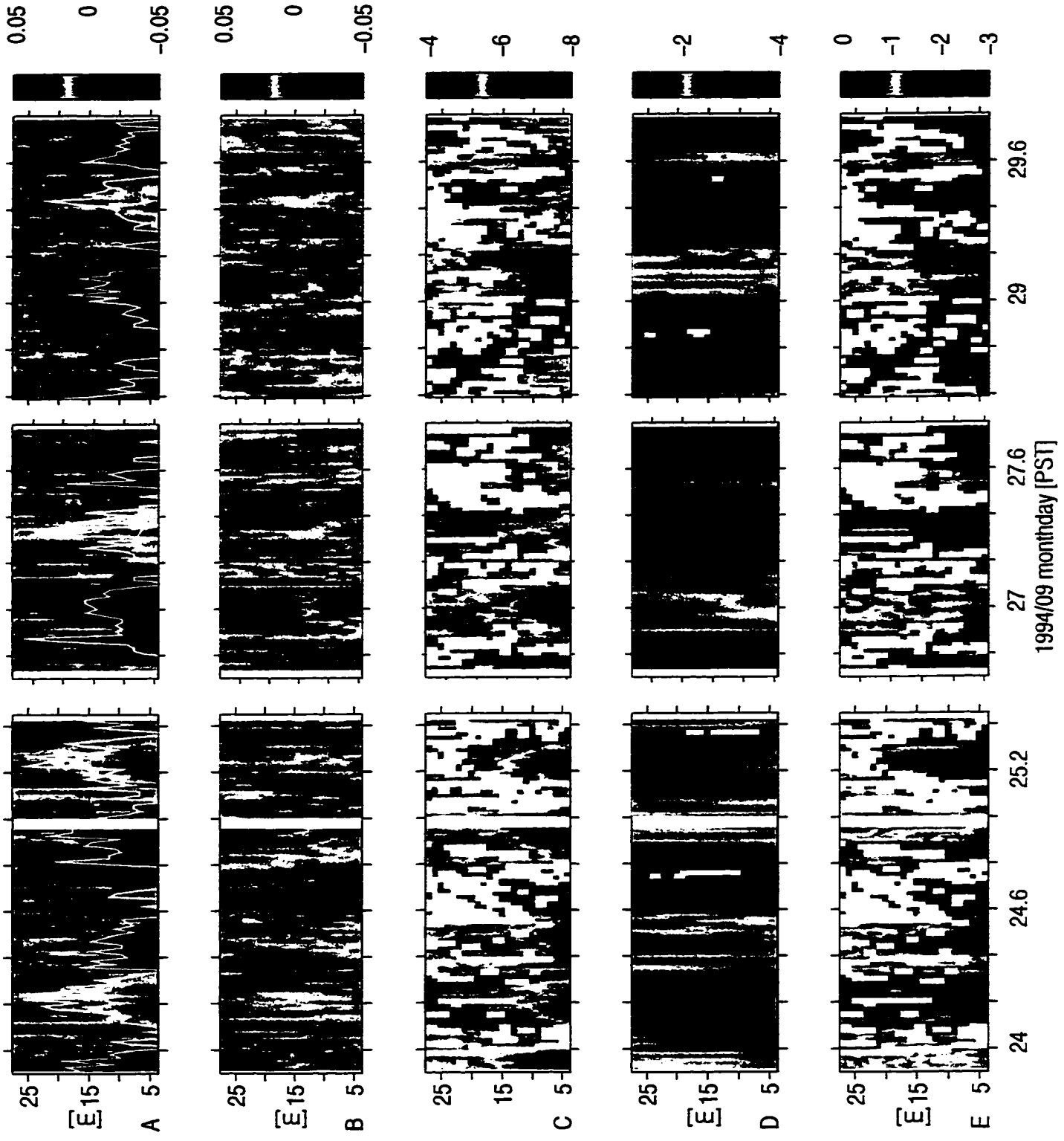

Figure 6.38: Depth-time sections of the 20-min mean local friction velocities (a) u_{*s}, (b) u_{*n} (m s^{-1}), (c) $log_{10}P$ (m^2 s^{-3}), (d) $log_{10}S$ (m^2 s^{-2}), and (e) $log_{10}A_v$ (m^2 s^{-1}). The blank areas in (c), (d) and (e) are where negative values of the corresponding quantities are obtained. White curves in panel (a) denote the height of the log-layer (m).

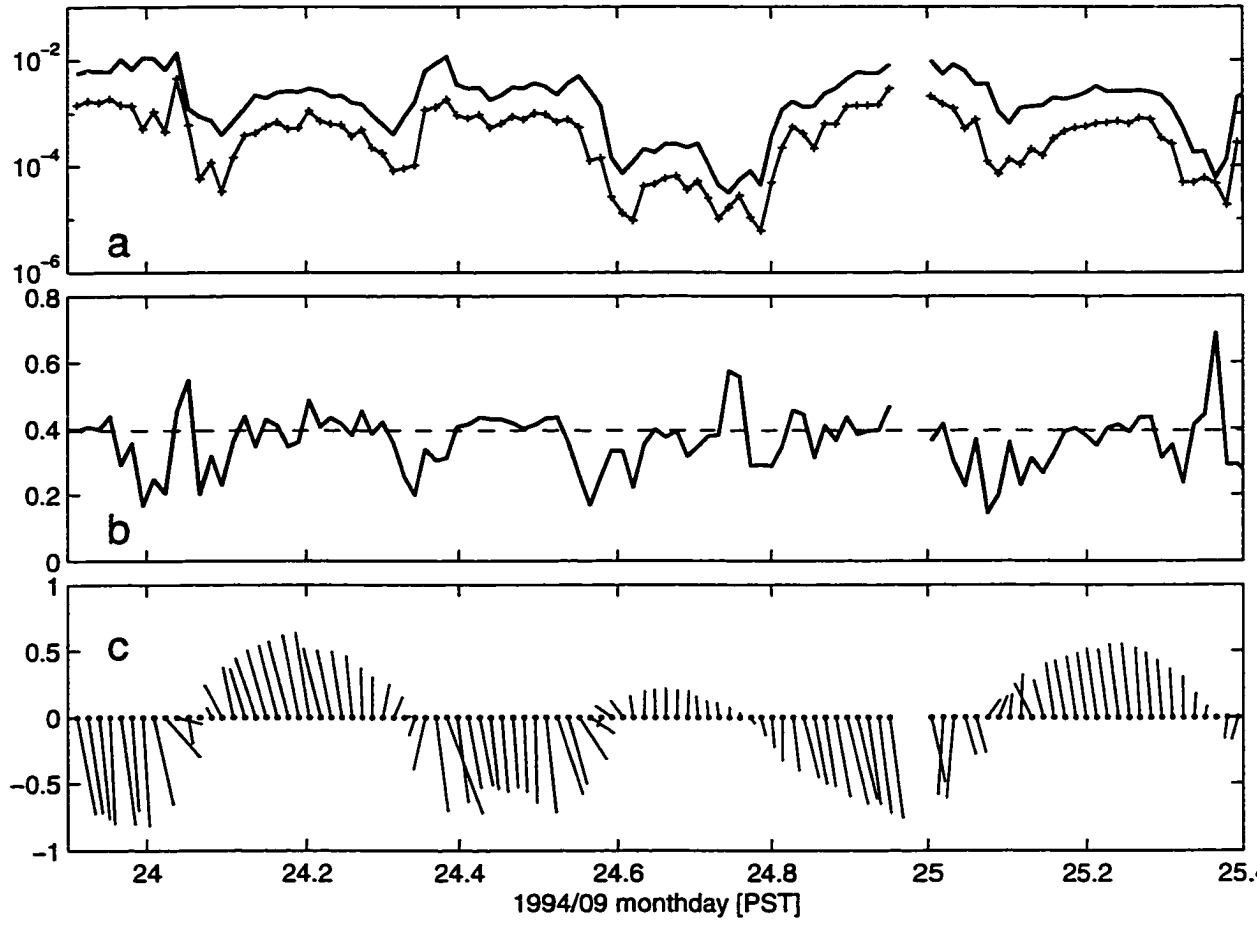

Figure 6.39: (a) TKE density $q^2/2$ (heavy solid lines) v. stress magnitude $|\overline{u'w'}|$ (thinner lines with crosses) (both in $m^2\ s^{-2}$); (b) Values of the stability function S_m calculated with (6.57) (solid line) v. $S_m = 0.39327$ (dashed line); (c) the stick diagram of the flow. The quantities are estimated at $z = 3.6$ m.

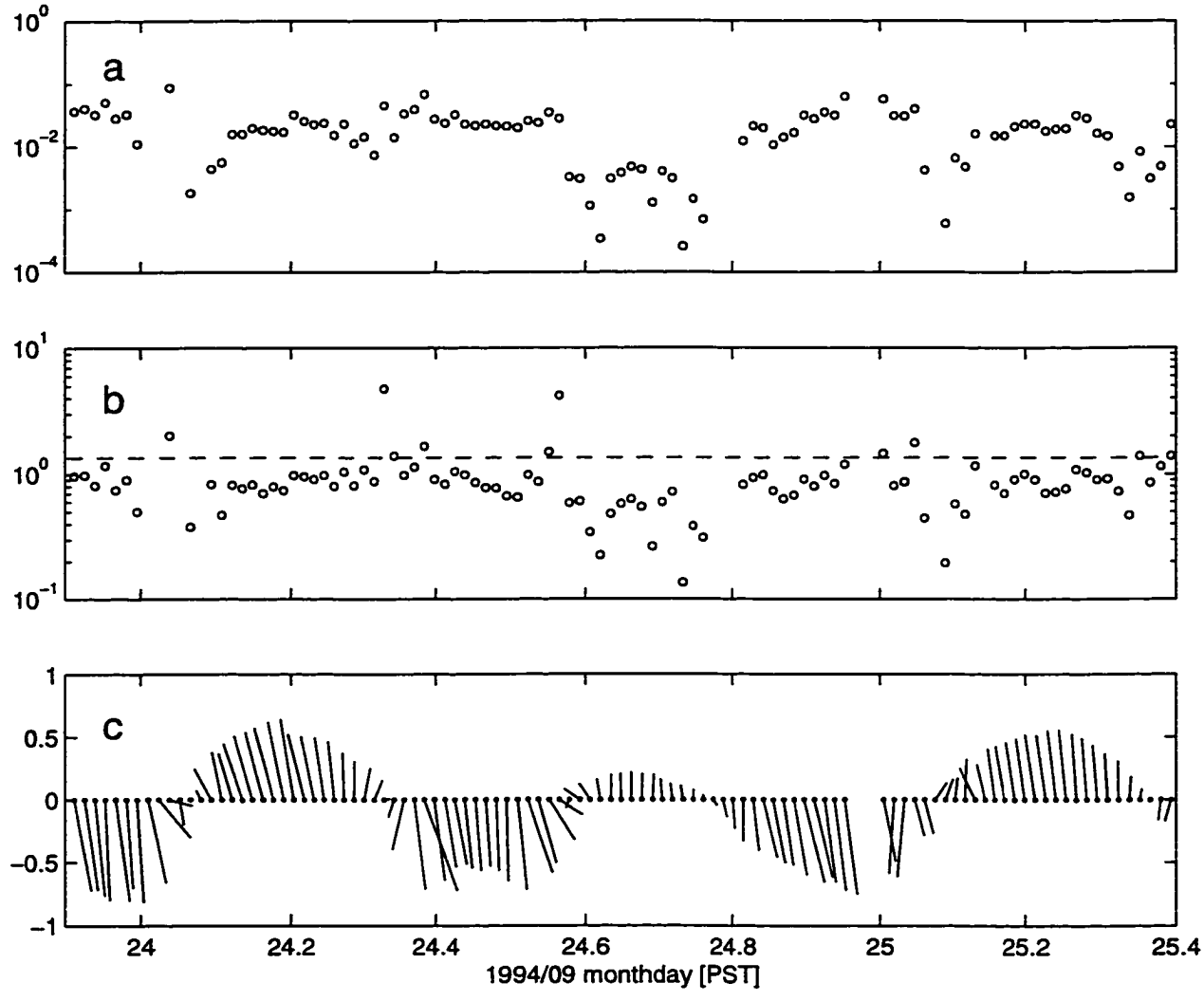

Figure 6.40: (a) Vertical eddy viscosity (A_v), (b) Prandtl mixing lengths l_m v. l defined by (6.56) (dashed lines). Panel (c) shows a stick diagram of the 20-min flow. The quantities are estimated at z = 3.6 m.

clear tidal variations, but they are elevated during the beginning and the end of the ebb when the flow direction is turning. Fig. 6.39b shows the values of the stability function S_m, which is related to the $q^2/2$-to-$|\overline{-u'w'}|$ ratio by (6.57). According to (6.52), S_m is a constant in unstratified flow, and equals $g_2 = 0.39327$ (Galperin et al., 1988). It is seen that the magnitude of S_m is close to g_2 during strong flows, and tends to be less than g_2 when the flow is weak.

A least-squares regression in logarithmic scales obtains a mean $q^2/2$-to-$|\overline{-u'w'}|$ ratio of 4.94, with a 95% confidence interval of ± 0.27 determined with a bootstrap method. By using (6.59) and assuming $\Gamma = 0$, the value of B_1 is determined to be 31.1 ± 2.5.

Fig. 6.40a shows the time variations of the vertical viscosity coefficient A_v. Except during the turning of the tide and during the weak flood between day 24.55 and 24.75, the eddy viscosity is almost independent of flow magnitude at logarithmic scales, ranging between 0.02-0.04 $m^2\ s^{-1}$. During the weak flood, A_v drops to 5×10^{-3} $m^2\ s^{-1}$ and lower. Fig. 6.40b illustrates the measured Prandtl mixing length (l_m). The majority values of l_m are about 1 m, and smaller than $l = 1.35$ m calculated using (6.56).

Fig. 6.41 compares P with the local time-derivative, advection by vertical flow, and diffusion of the TKE density $q^2/2$. The magnitude of P is constantly about 1 to 2 decades larger than the magnitudes of any of the other three terms. Hence, the contributions from the three terms on the left-hand side of (6.49) (except possibly the advection by horizontal flow which is not evaluated) are negligible to the TKE balance. Stratification is weak near the bottom, hence, the dominant balance in the TKE equation must be between production and dissipation.

Fig. 6.42 compares the TKE production rate P and the closure-based dissipation rate ϵ_{MY}, calculated by using $B_1 = 31.1$. The ebb-flood asymmetry in the magnitudes of both quantities is evident. During the ebb, the peaks of P and ϵ_{MY} are about

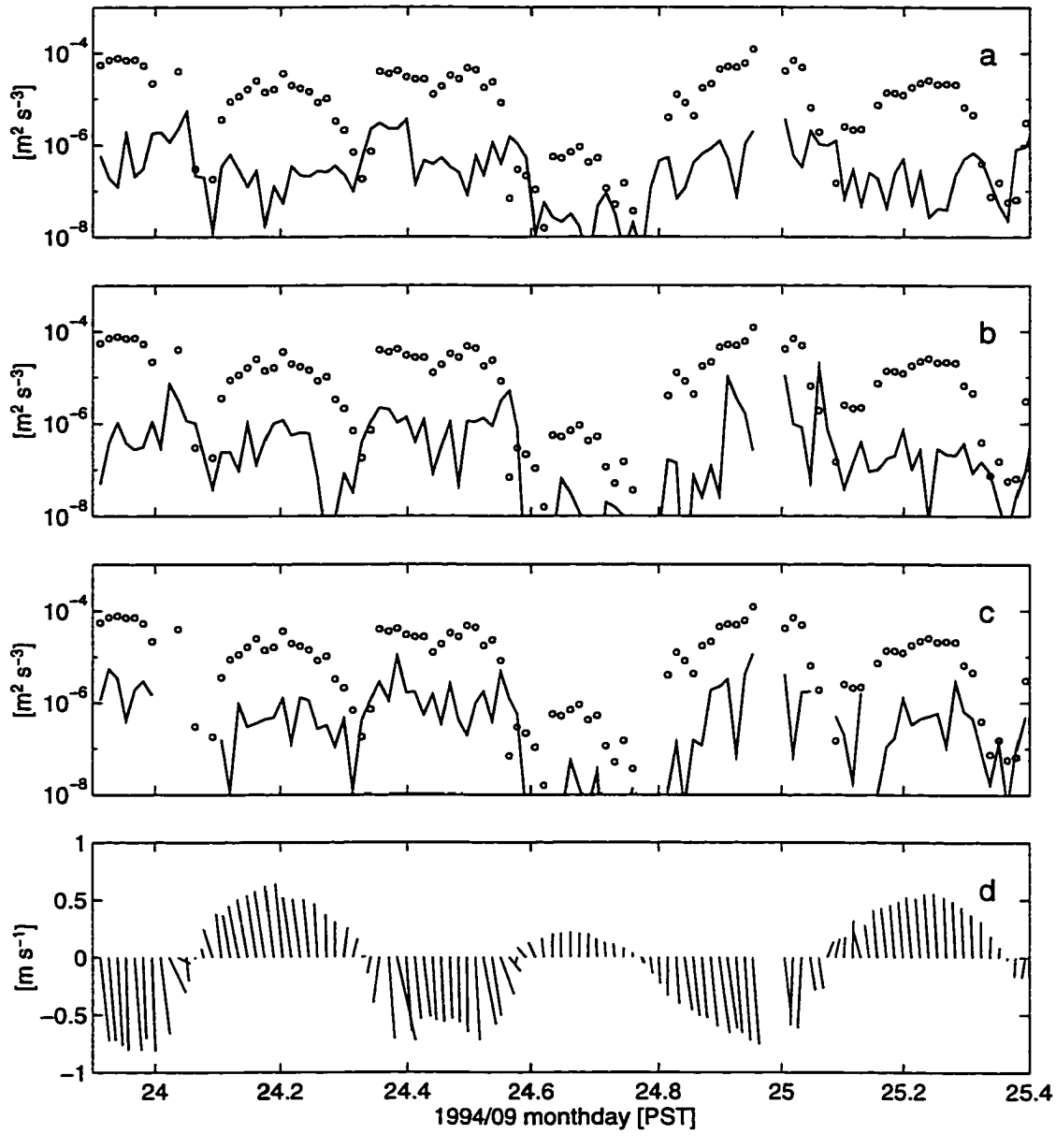

Figure 6.41: TKE production rate (open circles) v. (a) $\partial/\partial t(q^2/2)$, (b) $w\partial/\partial z(q^2/2)$, and (c) $\partial/\partial z[K_q^v \partial/\partial z(q^2/2)]$. Panel (d) shows a stick diagram of the 20-min flow. The quantities are estimated at $z = 3.6$ m.

1×10^{-4} m^2 s^{-3} when the flow is about 1 m s^{-1}. In contrast, peak values of P and ϵ_{MY} reach only 10^{-5} m^2 s^{-3} during the flood. There is a very good correlation between the variations of the two rates. Fig. 6.43 is a scatter plot of P vs. ϵ_{MY}. For a flow magnitude greater than 0.35 m s^{-1}, the two rates agree within a factor of 2. If $B_1 = 16.6$, the value suggested by Mellor and Yamada (1982), is used, the estimates of ϵ_{MY} tend to be 2 times larger than P. For a flow magnitude less than 0.35 m s^{-1}, the magnitude of the production rate is small (less than 3×10^{-6} m^2 s^{-3}), and the closure-based dissipation rate tend to be larger than P.

The along- and cross-channel local friction velocities u_{*s} and u_{*n} at 3.6 height are shown in Fig. 6.44. The along-channel friction velocity reaches 0.04 m s^{-1} during peak flows, corresponding to a streamwise stress magnitude of 1.6×10^{-3} m^2 s^{-2} (the large stress estimates obtained during the turning of the tide are not reliable). The cross-channel friction velocity reaches 0.025 m s^{-1} during peak ebb flows and is small during the flood. The variation of u_{*s} shows a clear tidal signal and correlates with the bottom friction velocity u_* (shown also in Fig. 6.44a) obtained by fitting the streamwise velocity profiles to a log-layer (Chapter 5). However, the log-layer fitted friction velocity is consistently larger than the local friction velocity at 3.6 m height, although the height of the log-layer, when it exists, exceeds 3.6 m. A regression shows that the bottom stress u_*^2 is on average 3 times larger than the along-channel stress $(\overline{-u'w'})_s$ at 3.6 m height. Fig. 6.45 shows a total of 22 consecutive profiles of along-channel friction velocity over one-half of the tidal period from day 24.2 - 24.5. Individual profiles of the along-channel stress are not constant, even within the log-layer.

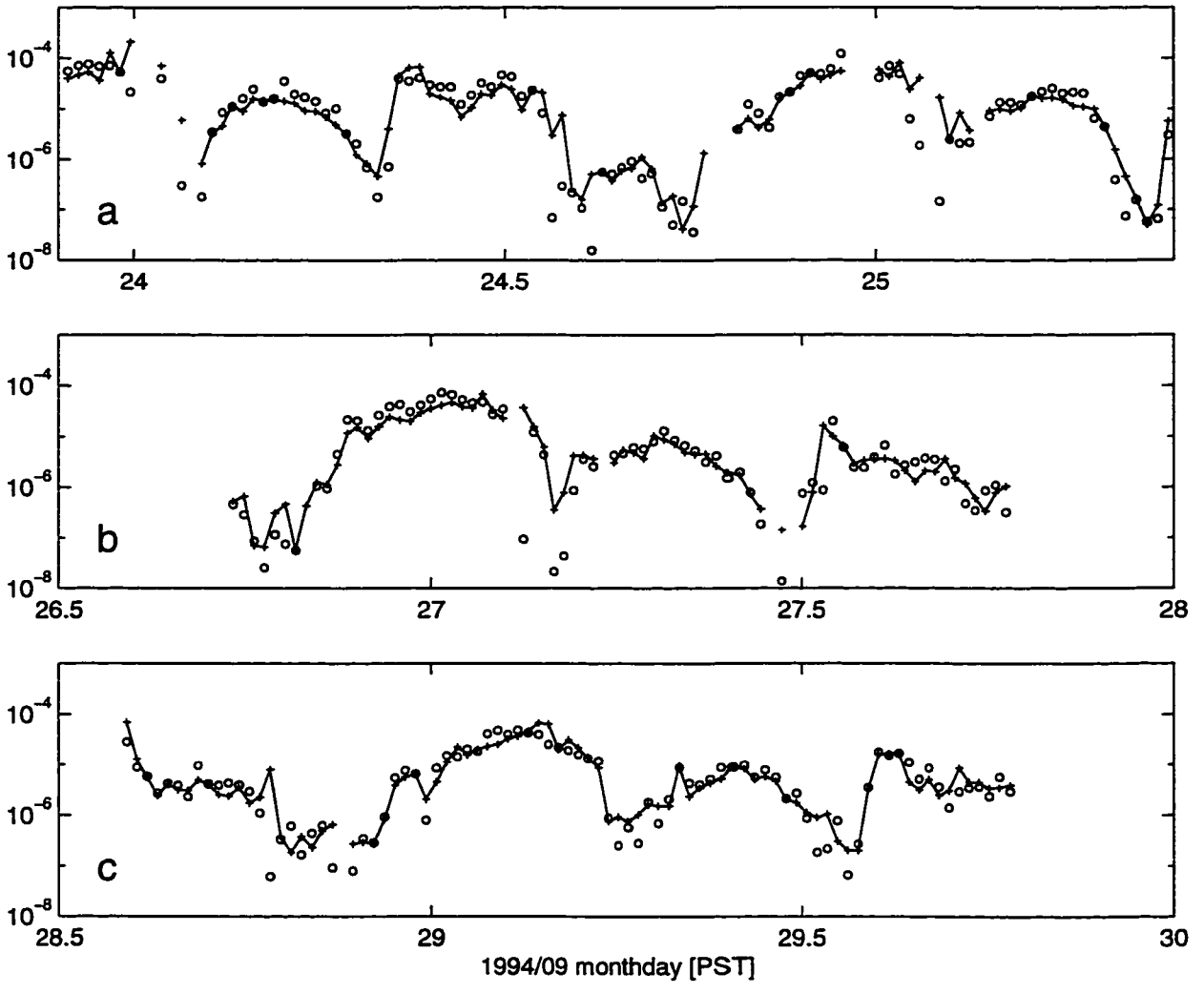

Figure 6.42: TKE production rate (open circles) v. the closure-based dissipation rate (solid lines with "+") at z = 3.6 m.

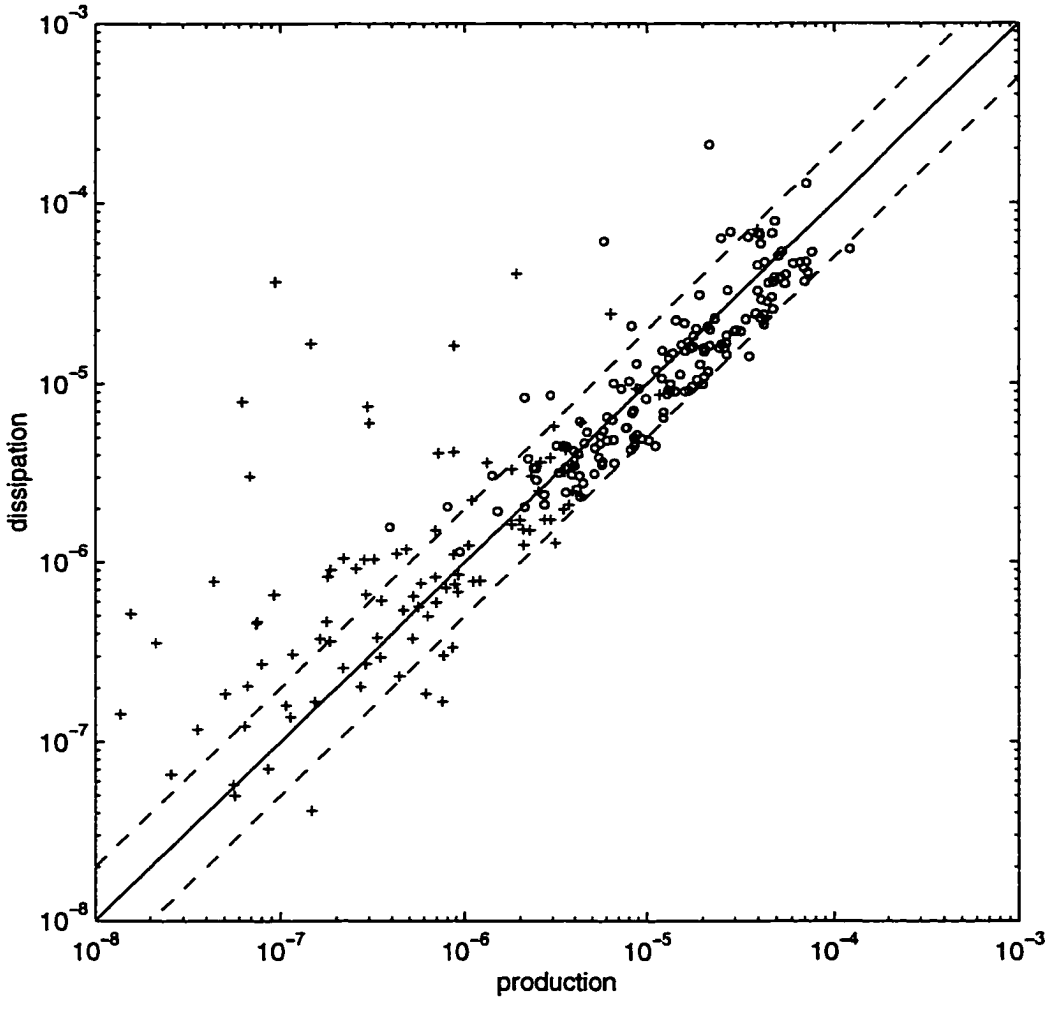

Figure 6.43: Scatter diagram of the TKE production rate v. dissipation rate (ϵ_{YM})at z = 3.6 m. The open circles are for flow magnitude > 0.35 m s^{-1} and crosses are for flow < 0.35 m s^{-1}. Solid line denotes a ratio of 1 and dashed lines represent ratios of 2 and 1/2 between the two quantities, respectively.

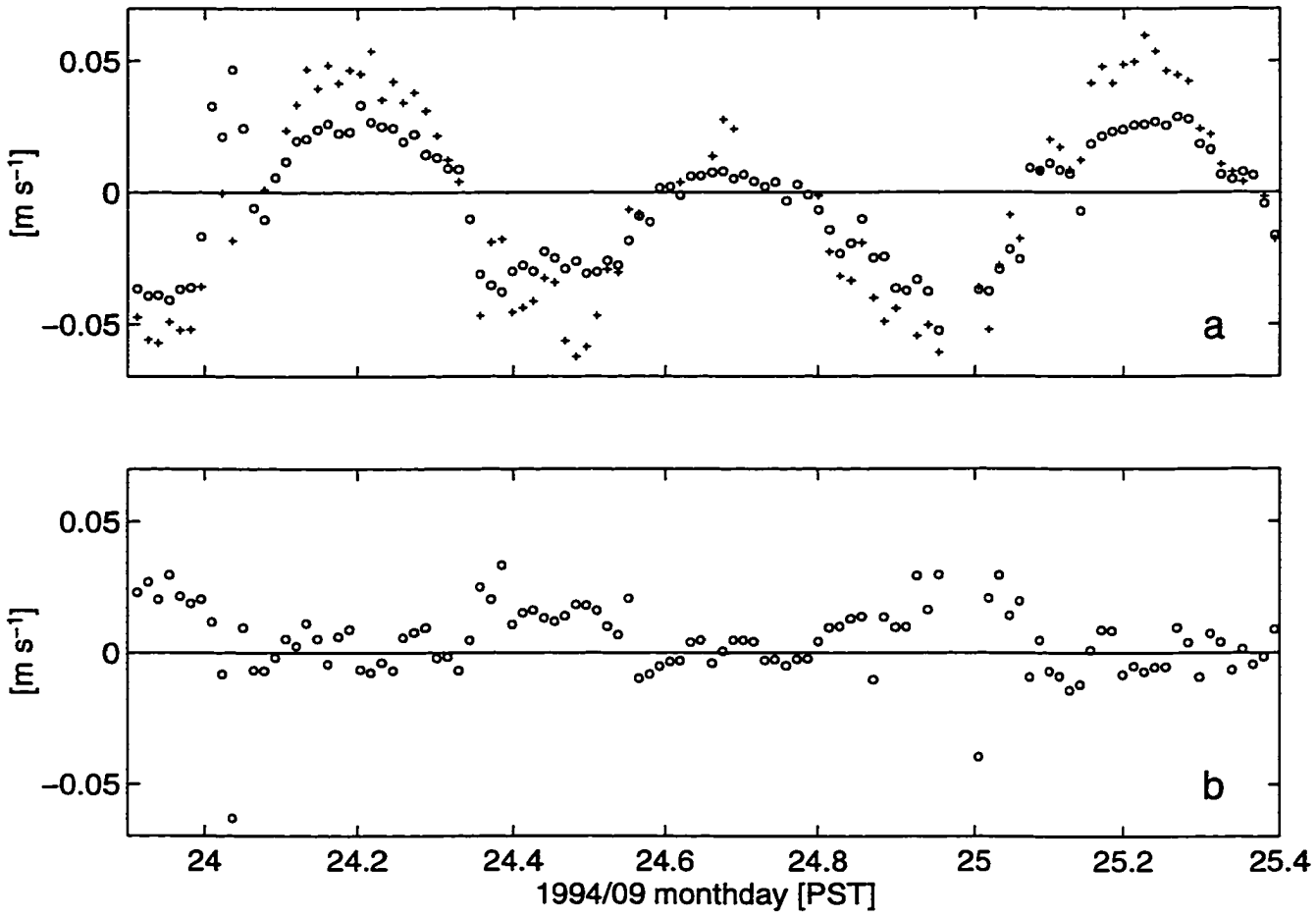

Figure 6.44: Time series of local friction velocities (a) u_{*s} and (b) u_{*n} (open circles) at z = 3.6 m, and u_* obtained by fitting the streamwise velocity profiles to a log-layer (+).

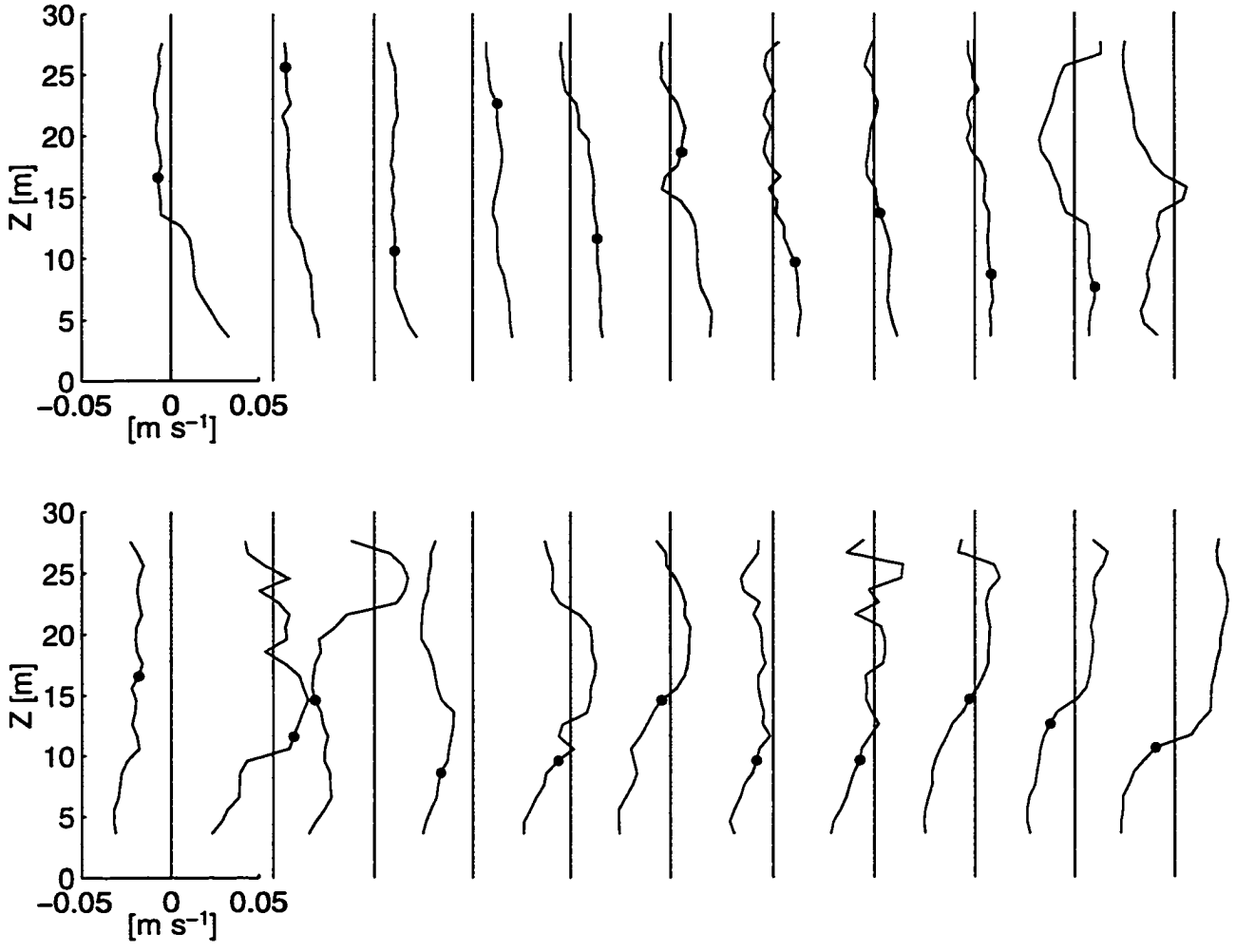

Figure 6.45: Consecutive profiles of along-channel friction velocity u_{*s} over one-half of the period of the M_2 tide (day 24.2 - 24.5). The solid circles mark the height of the log-layer.

6.5 Turbulence characteristics at mid-depth

Both the ADCP and TAMI took measurements at mid-depth in the channel. The two instruments were apart by about 50 and 100 m during the first and second deployments of TAMI, respectively. The vertical displacement of TAMI was determined to be less than ±1 m (Huang, 1996). To compare the estimates from the two instruments, the measurements from TAMI are averaged into 20-min ensembles, and the quantities estimated with the ADCP are averaged over three levels near mid-depth over the same 20-min intervals.

Variations of the TKE density $q^2/2$ and the magnitude of Reynolds stress $|\overline{-u'w'}|$ at mid-depth are shown in Fig. 6.46a. As was found near the bottom, there is a clear correlation between the magnitudes of the Reynolds stress and $q^2/2$. Values of the stability function S_m determined by the measured $q^2/2$-to-$|\overline{-u'w'}|$ ratio are comparable with those calculated using (6.52). Due to stratification, S_m at mid-depth is less than $g_2 = 0.39327$ (Fig. 6.46b). The mean $q^2/2$-to-$|\overline{-u'w'}|$ ratio is 6.06 ± 0.45, which is larger than the mean ratio of 4.94 ± 0.27 obtained at 3.6 m above the seabed. The value of B_1 is determined to be 42.2 ± 8.8 by assuming $\Gamma = 0$. The mean value of B_1 is 50.1 if $\Gamma = 0.2$.

Fig. 6.47 compares the vertical eddy viscosity coefficient A_v measured with the ADCP (using Eq. (6.42)) against (a), the diffusivity for density (K_v^ρ, calculated with (6.43) using $\Gamma = 0.2$), and (b), the diffusivity for temperature (K_v^T), both from measurements with TAMI. The agreement between A_v and K_v^ρ is very good and both ranged between $10^{-3} - 1$ m^2 s^{-1}. The correlation between A_v and K_v^T is generally good except that K_v^T occasionally has spikes of up to 10 m^2 s^{-1}, due to the small temperature gradients.

Fig. 6.48 compares the measured Prandtl mixing length (l_m), the Ozmidov length (l_O), and the z-dependent mixing length (l) specified by (6.56). Both l_m and l_O vary significantly with time. Similar as at z = 3.6 m, l_m is generally smaller than the

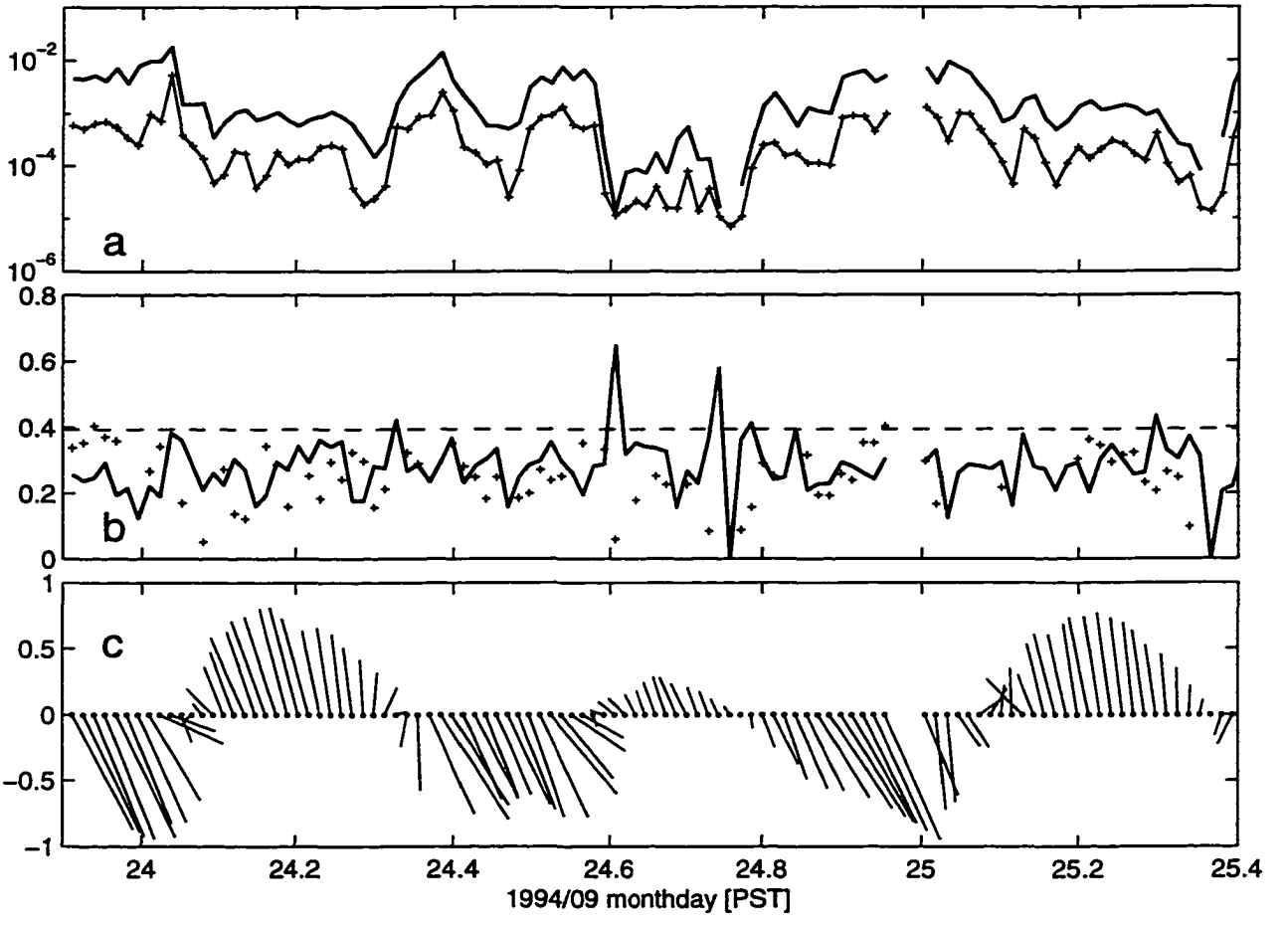

Figure 6.46: (a) TKE density $q^2/2$ (heavy solid lines) v. stress magnitude $|\overline{u'w'}|$ (thinner lines with crosses) (both in $m^2\ s^{-2}$); (b) Values of the stability function S_m calculated with (6.57) (solid line) and (6.52) (+) v. $S_m = 0.39327$ (dashed line); (c) the stick diagram of the flow. The quantities are estimated at mid-depth.

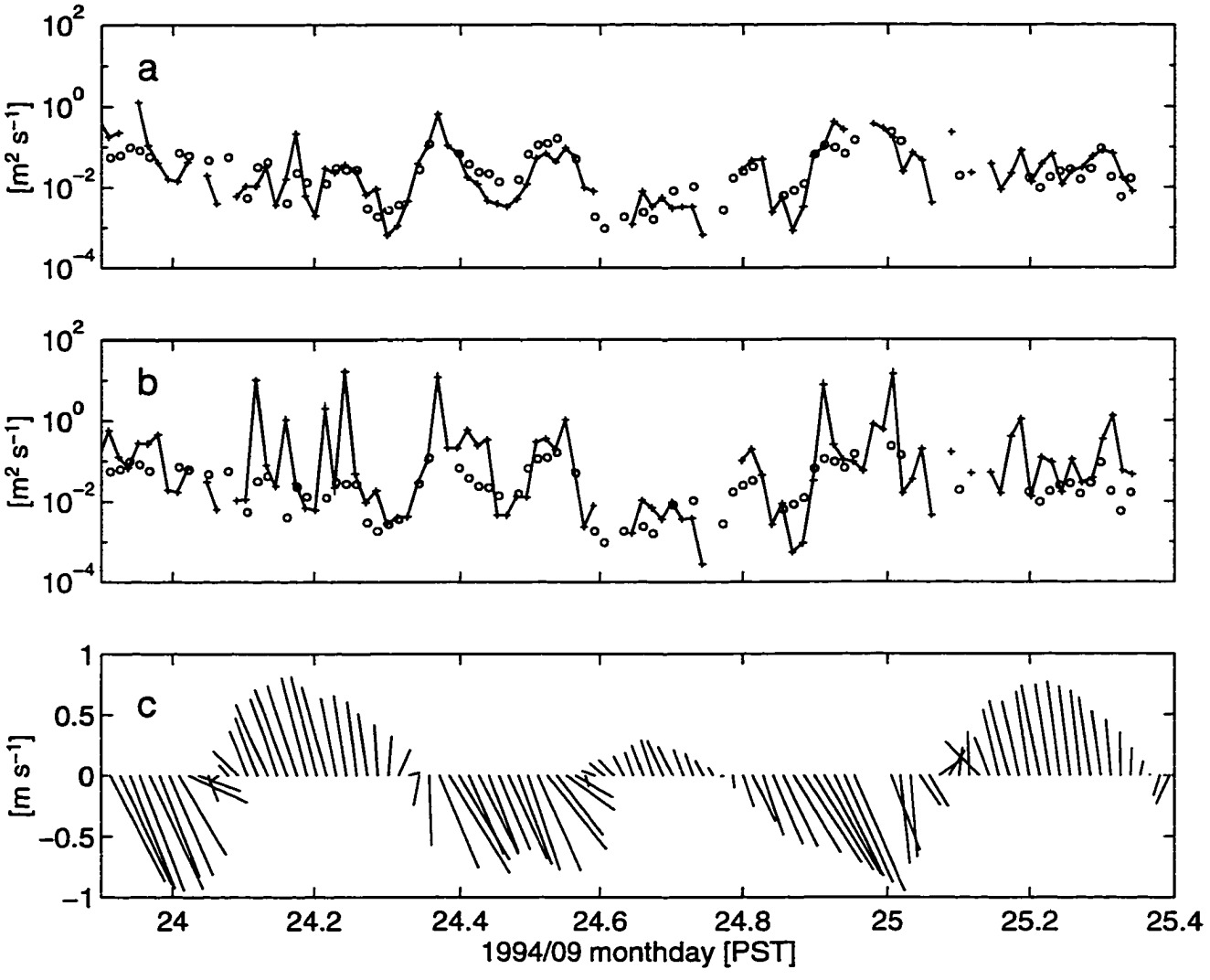

Figure 6.47: Time variations of the diffusivity for (a) density (K_v^ρ) and (b) temperature (K_v^T) (both denoted by solid lines with "+") against the vertical eddy viscosity A_v (open circles, both panels). Panel (c) shows a stick diagram of the 20-min flow. The quantities are estimated at mid-depth.

z-dependent mixing length l, which is 4.3 m at mid-depth. From (6.45) and (6.46), the ratio l_m to l_O is $Ri^{3/4}$ if $P \approx \epsilon$. With reference to Fig. 2.5, l_m is close to l_O when stratification is strong, while less than l_O when Ri is small.

Fig. 6.49 compares the closure-based TKE dissipation rate ϵ_{MY} (using $B_1 = 42.2$) with the completely independent estimates of ϵ from TAMI. Correlation between the variations of the two quantities can be observed, and their magnitudes are equal on average. If the original value of B_1 (16.6) is used, the closure-based dissipation rate tends to be 2.5 times larger than the estimates with TAMI.

We now proceed to discuss the TKE balance at mid-depth. Fig. 6.50 compares the estimates of ϵ from TAMI against the estimates of P from the ADCP. The time variations of ϵ correlate well with those of P. The peak values of both rates are about 2×10^{-5} m^2 s^{-3} (W kg^{-1}), and the minimum values are about 2×10^{-8} m^2 s^{-3}. Note that during the ebb from day 24.3 - 24.6, both quantities peaked when the flow direction fluctuated and dropped when the flow was unidirectional. The agreement between the two rates is slightly better during the first deployment of TAMI probably because the two instruments were closer together. Fig. 6.51 shows a scatter plot of P vs. ϵ. During the first deployment of TAMI, almost all of the ϵ values agree with P within a factor of 5, and this is also true for the majority of the ϵ values from the second deployment. This factor of 5 agreement is mainly due to the statistical nature of the P and ϵ estimates and the spatial separation of the two instruments. The agreement between the two quantities shrinks to within a factor of 2 if the two quantities are averaged over one quarter of a tidal cycle. The agreement is quite remarkable, considering that the two rates are obtained with two completely different instruments that are 50 - 100 m apart.

Fig. 6.52 compares the production rate and the magnitudes of the three terms on the left-hand side of (6.49). Estimates of the diffusion term are discarded when a negative diffusivity is included in the calculation. Consequently, we obtain only a few

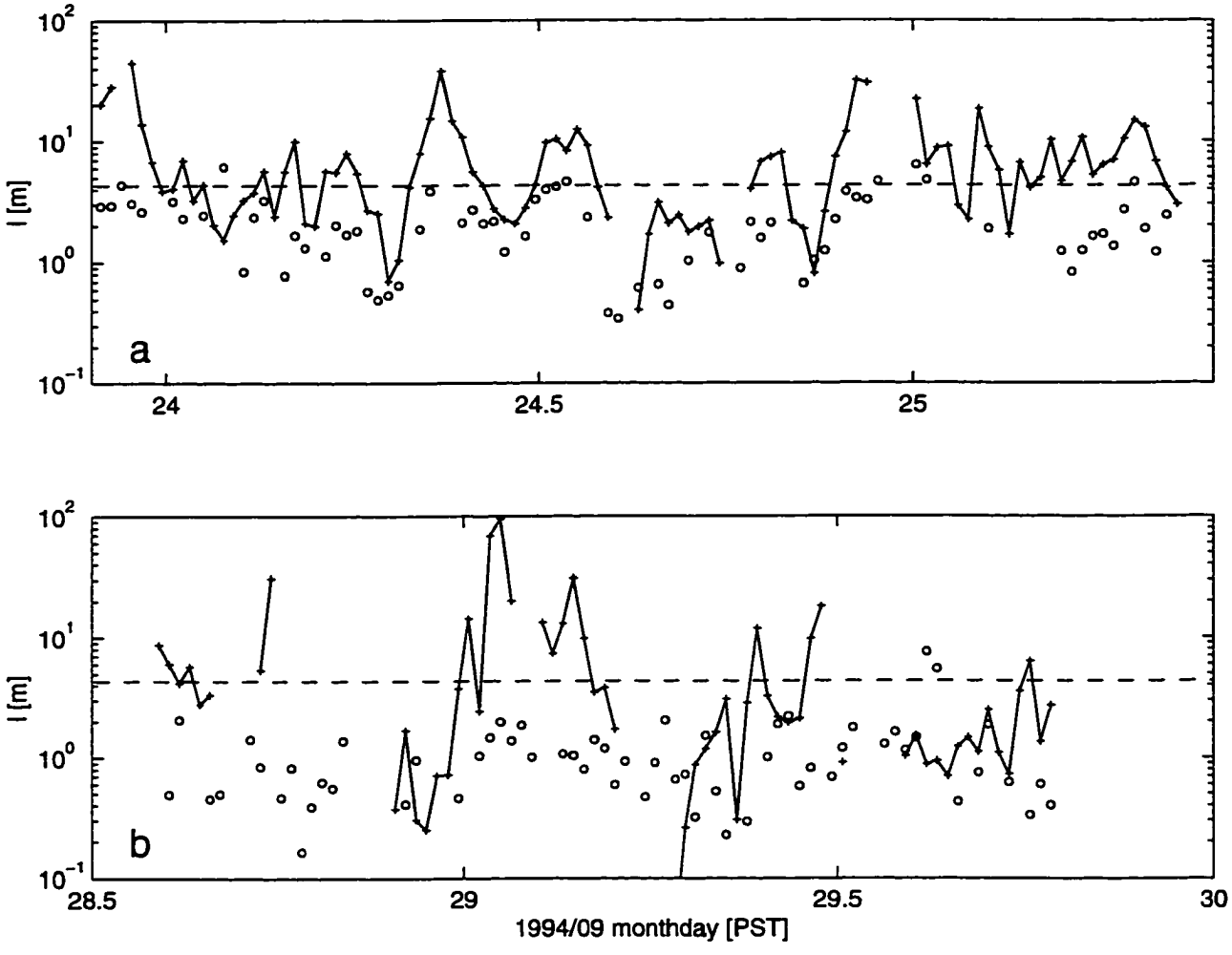

Figure 6.48: Time variations of the Prandtl mixing length l_m (open circles) and the Ozmidov length l_O (solid lines with "+"). The z-dependent mixing length l is plotted as dashed lines. The quantities are estimated at mid-depth.

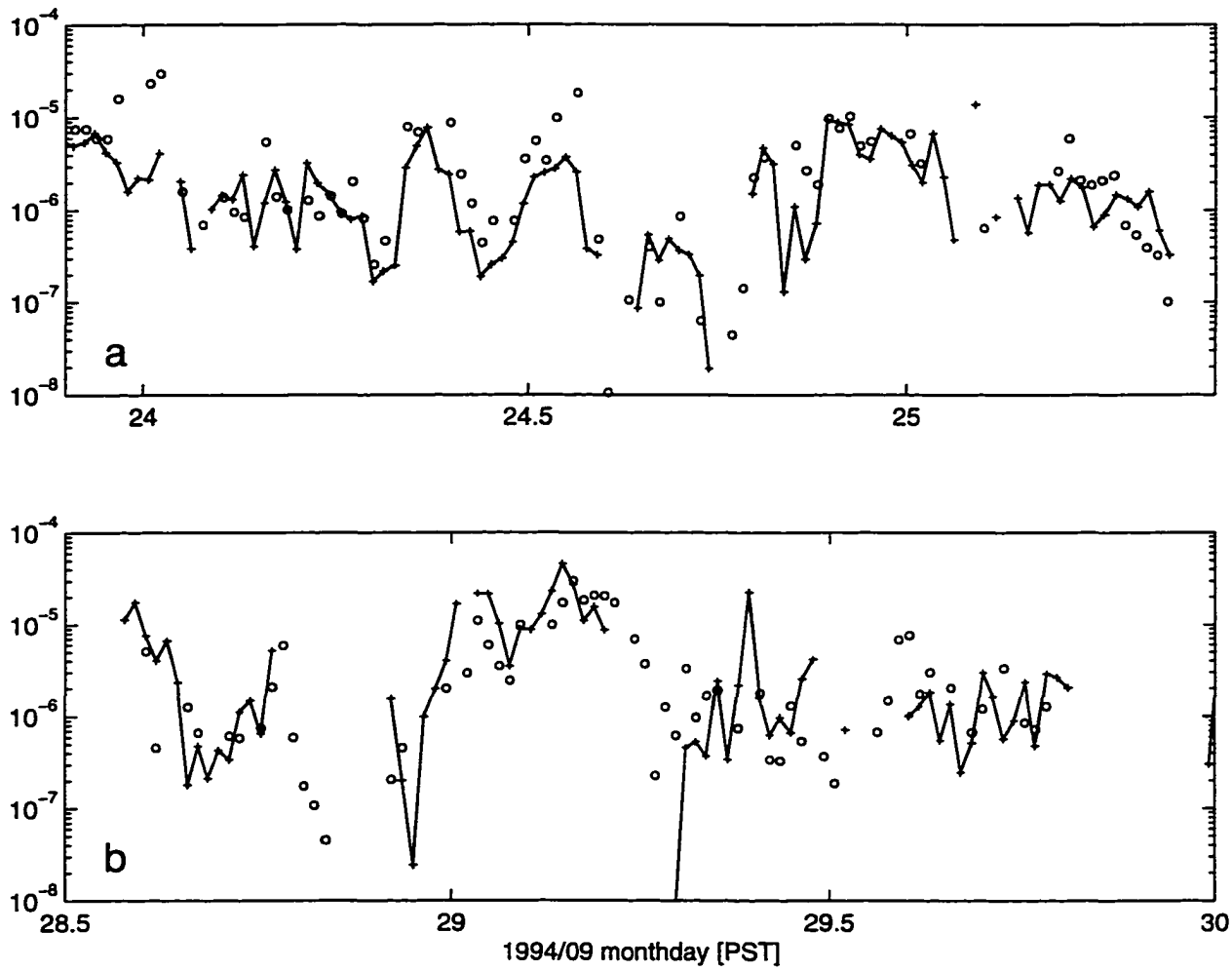

Figure 6.49: TKE dissipation rate ϵ measured with TAMI (solid lines with "+") v. closure-based dissipation rate ϵ_{MY} (open circles) at mid-depth.

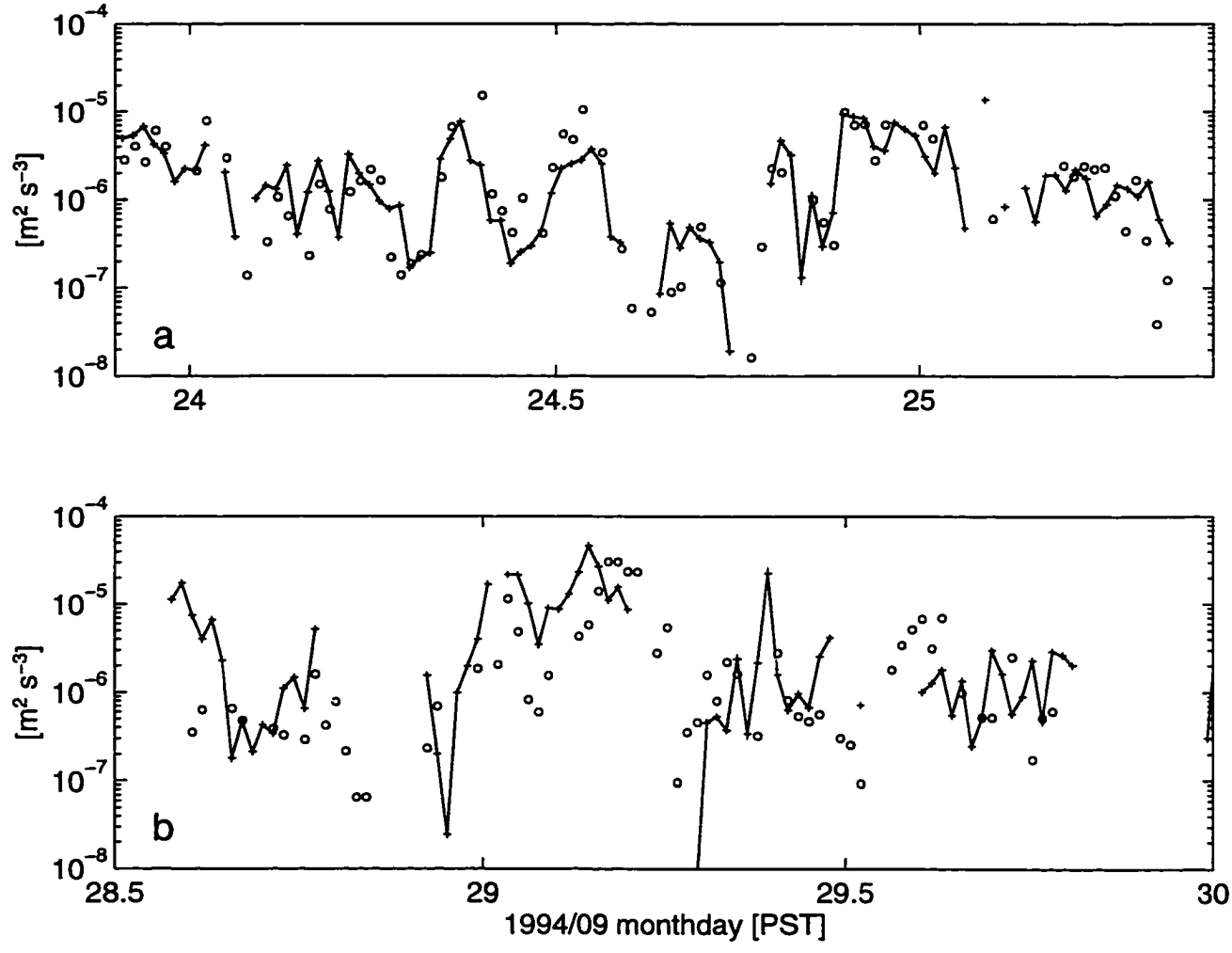

Figure 6.50: TKE dissipation rate ϵ measured with TAMI (solid lines with "+") v. production rate P (open circles) at mid-depth.

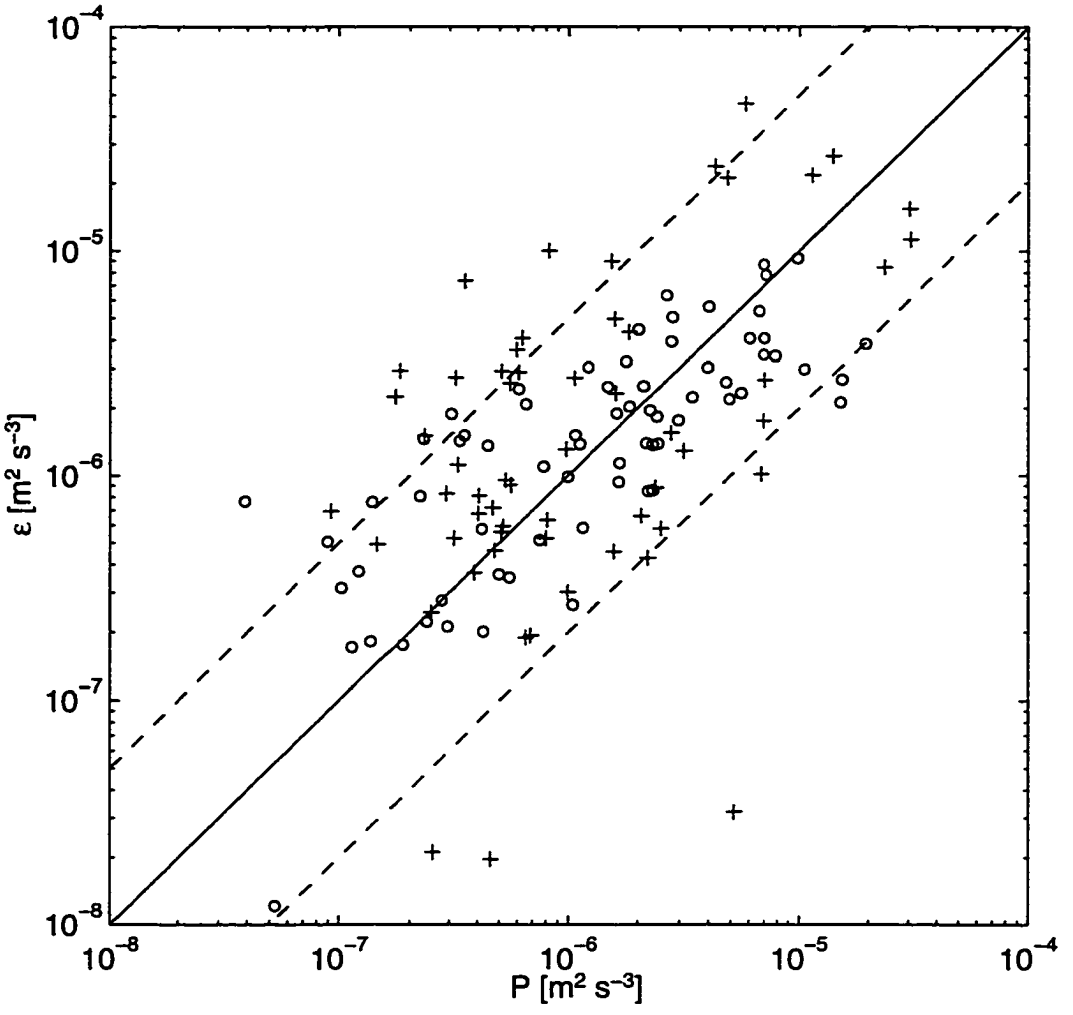

Figure 6.51: Scatter diagram of the TKE dissipation rate v. production rate at mid-depth. Open circles and crosses distinguish the first and second deployments of TAMI respectively. Solid line denotes a ratio of 1 and dashed lines represent ratios of 5 and 1/5 between the two quantities.

estimates of the diffusion term. In general, the production rate is about one decade larger than any of the other three terms at mid-depth. The local time derivative term, $\partial(q^2/2)/\partial t$, is comparable to P only when the TKE density drops sharply from an interval of high intensity to a less energetic one and vice versa (cf., Fig. 6.38d). The advection by mean vertical flow becomes comparable with P only during short intervals of large (> 0.015 m s^{-1}) vertical flow. The diffusion term also becomes comparable with P at times. Including the time derivative, advection and diffusion terms in P, $P - \partial/\partial t(q^2/2) - w\partial/\partial z(q^2/2) + \partial/\partial z[K_v^q \partial/\partial z(q^2/2)]$ does not show a better agreement with ϵ.

At mid-depth, there are no clear tidal signals in the estimates of turbulent quantities. Variations of the turbulent parameters appear to be only correlated with changes in TKE intensity. From Fig. 38c, the region of bottom-enhanced TKE production is generally below mid-depth during the flood. During the ebb, the region of enhanced production protrudes above mid-depth, which can be explained by the entrainment of water from the shallow Saanichton Bay to the main stream and eddy activities associated with the curvature effect of the headland.

6.6 Summary and discussion

A bottom-mounted ADCP and TAMI, moored at mid-depth, provide estimates of turbulent quantities at both the energy-containing and dissipation scales, as well as the estimates of the mean flow, shear, and the gradient of density. Using these data, we tested the Mellor-Yamada turbulent closure model on its parameterization of TKE dissipation rate (Eq. (6.51)), the formulation of the stability function S_m (Eq.(6.52)), and the value of the empirical constant B_1.

Close to the bottom where stratification is usually negligible, the measured ratio of TKE density $q^2/2$ to stress magnitude is 4.94 ± 0.27. The values of S_m are close to the specified value using (6.52) during strong flows, but tend to be less during weak

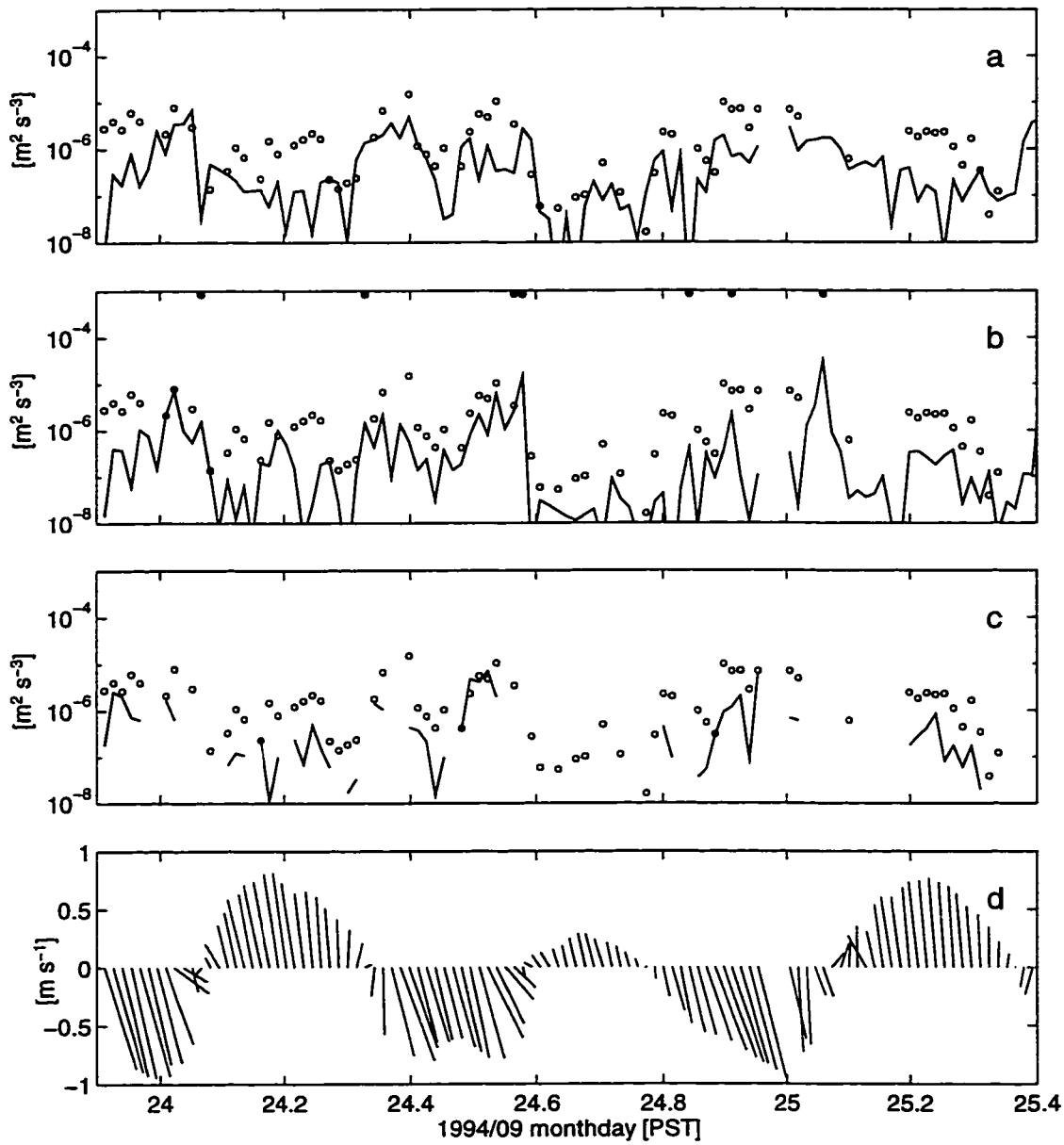

Figure 6.52: TKE production rate (open circles) v. (a) $\partial/\partial t(q^2/2)$, (b) $w\partial/\partial z(q^2/2)$, and (c) $\partial/\partial z[K_q^v \partial/\partial z(q^2/2)]$. The solid circles in panel (b) mark the events with the magnitude of the mean vertical flow > 0.015 m s^{-1}. Panel (d) shows a stick diagram of the 20-min flow. The quantities are estimated at mid-depth.

flows. The mean value of B_1 is 31.1 ± 2.5, larger than 16.6 given by Galperin et al. (1988). Using $B_1 = 31.1$, the measured production rate agrees with the closure-based dissipation rate within a factor of 2, and both are one to two decades larger than the rate of TKE change with time, the advection by the mean vertical flow, and diffusion. The increasing of B_1 from its original value, hence, is consistent with the local balance of TKE near the bottom.

At mid-depth, the measured $q^2/2$-to-$|\overline{-u'w'}|$ ratio is 6.06 ± 0.45. The values of S_m agree with the prediction using (6.52), and are less than $S_m = g_2$ in unstratified flow. The mean value of B_1 is 42.2 ± 8.8, which gives the closest agreement between the closure-based dissipation rate and that measured by TAMI.

The increasing of B_1 in wall-bounded boundary layers, from the original value used in Mellor-Yamada model, has been supported by the results of large-eddy simulations (Andre and Moeng, 1993). However, we must note that the values of B_1 matching the current dataset may not be exact, considering the uncertainties or biases in the Reynolds stress and TKE density estimates. The robustness of this analysis is the validation of the parameterization for dissipation rate with TKE density and mixing length (Eq.(6.51)). The measurement results also verify the decreasing of S_m with increasing stratification, as predicted by (6.52).

At mid-depth, independent estimates of the TKE production and dissipation rates are available, and both quantities agree within a factor of 5 for 20-min mean ensembles, and within a factor of 2 for averages over a quarter of tidal cycle. The terms representing the rate of TKE change with time, advection by mean vertical flow, and diffusion are usually 10 times smaller than either the production or dissipation rate.

The estimates of the eddy viscosity in the near-bottom layer range between 0.02 - 0.04 $m^2\ s^{-1}$, and are fairly steady except during the turning of the tide and very weak flows. At mid-depth, various estimates of the viscosity and diffusivity coefficients are in good agreement.

The measured Prandtl mixing length shows significant time variations and is smaller than the simple z-dependent specification of l by (6.56). At mid-depth, the Ozmidov length is larger than the Prandtl mixing length when stratification is weak, whereas l_O is close to l_m when the gradient Richardson number exceeds 0.25.

The estimated turbulent quantities contain clear signals of tidal variations near the bottom. At mid-depth, the major signal of time variation is the flood-ebb asymmetry, presumably caused by the events of eddy separation associated with the coastal curvature, and the entrainment of flow into the main stream of the channel from Saanichton Bay.

Changes in the sign and magnitude of the Reynolds stress correspond well with the changes in velocity shear. Although the mean velocity profiles are fitted accurately to a log-layer, the Reynolds stress is not constant within the log-layer. At 3.6 m height, the magnitude of the along-channel stress is smaller than the log-layer fitted bottom stress by a factor of 3. This result is inconsistent with the nearly "constant stress" profile predicted by the scaling arguments in the classical theory, for turbulent boundary layers over horizontal homogeneous bottoms (see, e.g. Tennekes, 1973). Interestingly, Johnson et al. (1994) found the same factor of 3 discrepancy between the bottom stress obtained from log-layer fitting and that derived from dissipation estimates using data collected in the Mediterranean outflow.

The mismatch between the log-layer fitted bottom stress and the direct estimates of Reynolds stress near the bottom is related to the difference between the measured Prandtl length and the z-dependent specification of mixing length. Further examination of other possible biases in estimating stress with the variance technique using the ADCP, particularly the potential variance reduction associated with spatial-averaging, needs to be pursued (Stephen Monismith, personal communication, 1997). If the measurement biases are proved to be negligible, a possible explanation for the mismatch is the influence of horizontal inhomogeneity caused by bed forms (Belcher

et al., 1993). We leave the question about the connection between the bottom friction velocity and the Reynolds stress distribution to a future study.

Chapter 7

Conclusions

During a multi-investigator experiment conducted in a tidal channel along the coast of British Columbia, we deployed a broadband ADCP and a moored microstructure instrument (TAMI). The goal of this thesis is to study the use of the ADCP for taking measurements in a highly turbulent environment, and to examine the flow and turbulence in a tidally forced boundary layer.

7.1 Measurements with an ADCP

A multi-beam ADCP remotely senses the velocities in the directions along its acoustic beams. The performance of an ADCP in velocity profiling can be described by several key parameters: profiling range, spatial resolution, sampling rate, and noise level. The profiling range of an ADCP covers a large portion of water column in coastal waters, except that it cannot be used to take measurements within a short (1 - 2 m) distance from the bottom and the surface. The spatial resolution is adequate to reveal the rapid changes of flow field in the vertical space. For direct-reading deployments, there are no constraints of battery capacity and solid-state memory, hence, the data can be collected at rapid rates. The fastest sampling rate we obtained is 1.3 Hz, which makes it possible to determine the statistical uncertainty of the mean flow estimates, and to resolve the spectral ranges contributing to the Reynolds stress and turbulent kinetic energy (TKE) density. The single-ping standard deviation of Doppler noise is estimated to be 0.02 - 0.03 m s^{-1} for our broadband unit. However, the statistical uncertainties in the estimates of the mean flow, shear, and turbulence stem mainly

from turbulent fluctuations. Doppler noise causes a systematic bias in the estimates of the TKE density, but not to the Reynolds stress if the noise standard deviations of the two beams in a pair are identical.

In the derivation of the mean flow vector and the second-order turbulent moments, one must assume that the mean flow field and turbulent statistics are homogeneous over the distance separating the beam pairs. A comparison of the estimated mean velocity against the "error" velocity provides an explicit test for statistical homogeneity. The number of horizontal velocity estimates that pass a simple test for homogeneity increases rapidly with increasing averaging distance, and exceeds 95% for distances exceeding 55 beam separations. There are no explicit tests for the homogeneity of the second-order moments. In this study, we choose 20 minutes as the ensemble averaging time to calculate the mean flow and turbulent quantities. Velocity fluctuations at periods longer than 20 minutes make little contributions to the estimates of the Reynolds stress and TKE density.

Instrument motion must be carefully considered in interpreting the measurements using an ADCP in a turbulent environment. Analysis of the computation algorithm shows that, for non-rigidly mounted deployments, the influence of instrument motions is likely to be negligible in the estimates of horizontal velocity, whereas it can be significant for the vertical flow. To estimate turbulent moments with the variance technique requires the ADCP to be rigidly mounted.

The misalignment of the instrument axis with respect to vertical, i.e., the magnitudes of the pitch and roll angles, can be compensated in the calculation of the mean flow. However, it causes a bias in the estimates of the Reynolds stress. This bias can be eliminated if the ADCP has a fifth transducer directed along the instrument axis. Another advantage of using a 5-beam unit is that the TKE density can be unambiguously determined. When using a 4-beam unit, one must assume a value for the anisotropy factor in estimating the TKE density.

With increasing TKE density, the statistical uncertainty of the Reynolds stress estimates increases, whereas the relative uncertainty decreases. The highest signal to noise ratio is obtained at levels close to the bottom, where the stress magnitudes are large. The minimum uncertainty of stress estimates is $\pm 1.5 \times 10^{-5}$ m^2 s^{-2}, obtained during weak flows. During the turning of the tide and the events of flow separation from the headland at one side of the channel, turbulence was not stationary, and the estimates of turbulent moments are unreliable. The production rate of TKE and the vertical eddy viscosity coefficient are derived by combining estimates of the Reynolds stress and shear.

7.2 The tidally forced turbulent boundary layer

CTD profiles, taken near the southern entrance of the channel (upstream during the flood), show a fairly well mixed layer above the seabed. The height of this mixed layer varies with tidal flow, in accordance with the variation of the height of the log-layer. At mid-depth, estimates of the gradient Richardson number show that the water column is stable more often than it is unstable during the flood, whereas the chances of shear stability and instability are roughly equal during the ebb. Toward the bottom layer, the frequency of occurrence of shear instability increases.

Measurements with the ADCP provide a total of 4.5 days of estimates of the mean flow and shear and 3.8 days of estimates of the turbulent quantities. The profiling range (in terms of the center of the depth cells) is between 3.6 - 27.6 m in the center of the channel, where the depth is about 30 m. The spatial resolution of the estimates is 1 m. Clear tidal signals are contained in the streamwise velocity. The streamwise shear and the along-channel stress also contain clear tidal variations in the lower half of the water column, but reverse signs above mid-depth. The transverse flow, shear, and cross-channel stress present a flood-ebb asymmetry caused by the variations in the curvature effect of the headland. During the ebb, the curvature effect is strong

and drives a substantial secondary flow causing the transverse shear. During the flood the curvature effect is weak, and the transverse flow, shear, and cross-channel stress are small. The TKE production rate generally intensifies toward the bottom, bearing the character of wall-bounded turbulence. Events of large production above mid-depth, corresponding to the sign reversals of shear and stress, occur occasionally during the ebb.

Profiles of the streamwise velocity are fitted to a logarithmic form with 1% accuracy. The height of the log-layer varies tidally and reaches 20 m above the bottom during peak flows of 1 m s^{-1}. The height is well predicted by $0.04u_*/\omega$, where u_* is the friction velocity and ω is the angular frequency of the dominant tidal constituent. The mean non-dimensional shear, $(\partial U/\partial z)/(u_*/\kappa z)$, is within 1% of unity at the 95% level of confidence inside the log-layer. The friction velocity varies tidally and reaches $O(0.05)$ m s^{-1} during peak current flow. The bottom drag coefficient, referenced to the depth-mean flow, is 4×10^{-3}. The observed log-layer is not connected to skin friction, but possibly to form drag. Deviations of the measured velocity from the logarithmic profiles above the log-layer can be explained by the zero-stress boundary condition at the surface and by the entrainment of shallow water at mid-depth. The deviations are inconsistent with the effects of acceleration/deceleration and stratification.

The moored microstructure instrument TAMI was deployed twice at mid-depth, apart from the ADCP by 50 and 100 m during the first and second deployments, respectively. Measurements with TAMI provide estimates of the dissipation rates of TKE and temperature fluctuation variance, and the buoyancy frequency at mid-depth. Combining the measurements taken with the ADCP and TAMI, we obtained estimates of the eddy viscosity and diffusivity coefficients, and the Prandtl mixing length and Ozmidov length. The estimated turbulent quantities contain clear signals of tidal variations near the bottom, but tidal variations are less evident at and above

mid-depth. Near the bottom, the eddy viscosity is almost independent of flow magnitude at logarithmic scales, ranging between 0.02 - 0.04 $m^2\ s^{-1}$, except during the turning of the tide and during the weak flows. At mid-depth, the diffusivity of density and heat (deduced from microstructure measurements) agrees with the viscosity derived from measurements with the ADCP. Both near the bottom and at mid-depth, the measured Prandtl length contains significant time variations, and it is less than the Ozmidov length when stratification is weak. With the measured turbulent quantities, we tested the Mellor-Yamada turbulent closure model on its parameterization of TKE dissipation rate with TKE density and the mixing length. Both near bottom and at mid-depth, the closure-based dissipation rate agrees with the measured production and dissipation rates by increasing the value of the empirical parameter B_1 from the original value used in Mellor-Yamada model. At mid-depth, the rate of production deduced from the ADCP agrees with the rate of dissipation measured with TAMI. The dominant terms in the TKE budget are the rates of production and dissipation of TKE, and both rates are one to two decades larger than the other terms in the TKE conservation equation.

The scaling of the log-layer height with tidal frequency in the channel is comparable to the scaling with Coriolis parameter for the log-layer in steady planetary boundary layer. However, some results are inconsistent with those from boundary layers over horizontal homogeneous bottoms. The Reynolds stress is not constant within the log-layer, and its magnitude at 3.6 m height is on average 3 times smaller than the shear velocity squared (u_*^2) derived from log-layer fitting. The peak of the non-dimensional spectrum for the Reynolds stress, when compared to the measurements from the atmospheric boundary layer, is shifted to higher wavenumbers (non-dimensionalized by κz) by a factor of 2.5. The measured Prandtl mixing length vary with time and are usually smaller than lengths based only on geometry, for example, $\kappa z(1 - z/h)^{1/2}$, or κz as suggested by the scaling arguments that derive

the log-layer. One possible explanation for these discrepancies is the influence of horizontal inhomogeneity caused by bed forms.

Bibliography

[1] Andrew, A., and Moeng, C.-H., 1993. Single-point closures in a neutrally-stratified boundary layer. *J. Atmos. Sci.*, **50**, 3366-3379.

[2] Belcher, S. E., T. M. J. Newley, and J. C. R. Hunt, 1993. The drag on an undulating surface induced by the flow of a turbulent boundary layer. *J. Fluid Mech.*, **249**, 557-596.

[3] Blumberg, A.F., and G. L. Mellor, 1987. A description of a three-dimensional coastal ocean circulation model. In: *Three-Dimensional Coastal Ocean Models*, Heaps, N. S. (Ed.), Coastal and Estuarine Sciences, **4**, AGU, Washington , D.C., pp. 1-16.

[4] Bowden, K. F., 1978. Physical problems of the benthic boundary layer. *Geophys. Surv.*, **3**, 255-296.

[5] Brors, B., and K. J. Eidsvik, 1994. Oscillatory boundary layer flows modeled with dynamic Reynolds stress turbulence closure. *Cont. Shelf Res.*, **14**, 1455-1475.

[6] Chriss, T. M. and D. R. Caldwell, 1982. Evidence for the influence of form drag on bottom boundary layer flow. *J. Geophys. Res.*, **87**, 4148-4154.

[7] Clauser, F. H., 1956. The turbulent boundary layer. *Advances in Applied Mechanics*, **4**, 2-51.

[8] Dewey, R. K., and W. R. Crawford, 1988. Bottom stress estimates from vertical dissipation rate profiles on the continental shelf. *J. Phys. Oceanogr.*, **18**, 1167-1177.

[9] Edson, J. B., C. W. Fairall, P.G. Mestayer, and S. E. Larsen, 1991. A study of the inertial-dissipation method for computing air-sea fluxes. *J. Geophys. Res.*, **96**, 10,689-10,711.

[10] Efron, B., and R. J. Tibshirani, 1993. *An Introduction to the Bootstrap.* Chapman & Hall, New York-London, 436 pp.

[11] Fleury, M., and R. G. Lueck, 1994. Direct heat flux estimates using a towed vehicle. *J. Phys. Oceanogr.*, **24**, 801-818.

[12] Foreman, M. G. G., R. A. Walters, R. F. Henry, C. P. Keller, and A. G. Dolling, 1995. A tidal model for eastern Juan de Fuca Strait and the southern Strait of Georgia. *J. Geophys. Res.*, **100**, 721-740.

[13] Galperin, B., L. H. Kantha, S. Hassid, and A. Rosati, 1988. A quasi-equilibrium turbulent energy model for geophysical flows. *J. Atmos. Sci.*, **45**, 55-62.

[14] Gargett, A.E., 1985. Evolution of scalar spectra with the decay of turbulence in a stratified fluid. *J. Fluid Mech.*, **159**, 379-407.

[15] Gargett, A.E., 1988. A "large-eddy" approach to acoustic remote sensing of turbulence kinetic energy dissipation rate ϵ. *Atmos.-Ocean*, **26**, 483-508.

[16] Gargett, A.E., 1994. Observing turbulence with a modified acoustic Doppler current profiler. *J. Atmos. Oceanic Technol.*, **11**, 1592-1610.

[17] Garrett,C. J. R., and R. H. Loucks, 1976. Up-welling along the Yarmouth shore of Nova Scotia. *J. Fish. Res. Board Can.*, **33**, 116-117.

[18] Geyer, W. R., 1993. Three-dimensional tidal flow around headlands. *J. Geophys. Res.*, **98**, 955-966.

[19] Geyer, W. R., and R. Signell, 1991. Measurements and modeling of the spatial structure of nonlinear tidal flow around a headland. In: *Tidal Hydrodynamics*, Parker, B. B. (Ed.), John Wiley and Sons, 883pp.

[20] Grant, H.L., R. W. Stewart, and A. Moilliet, 1962. Turbulence spectra from a tidal channel. *J. Fluid Mech.*, **12**, 241-263.

[21] Grant, W. D., and O. S. Madsen, 1979. Combined wave and current interaction with a rough bottom. *J. Geophys. Res.*, **84**, 1797-1808.

[22] Grant, W. D., A. J. Williams, and S. M. Glenn, 1984. Bottom stress estimates and their prediction on the Northern California continental shelf during CODE-1: The importance of wave-current interaction. *J. Phys. Oceanogr.*, **14**, 506-527.

[23] Green, M. O., and I. N. McCave, 1995. Seabed drag coefficient under tidal currents in the eastern Irish Sea. *J. Geophys. Res.*, **100**, 16057-16069.

[24] Gross, T. F., 1986. Modeling time dependence in a tidal boundary layer. *Cont. Shelf Res.*, **3**, 431-448.

[25] Gross, T. F., and A. R. M. Nowell, 1983. Mean flow and turbulence scaling in a tidal boundary layer. *Cont. Shelf Res.*, **2**, 109-126.

[26] Gross, T. F., and A. R. M. Nowell, 1985. Spectral scaling in a tidal boundary layer. *J. Phys. Oceanogr.*, **15**, 496-508.

[27] Gross, T. F., A. E. Isley, and C. R. Sherwood, 1992. Estimation of stress and bed roughness during storms on the Northern California Shelf. *Cont. Shelf Res.*, **12**, 389-413.

[28] Heathershaw, A. D., 1976. Measurements of turbulence in the Irish Sea benthic boundary layer. In: *The Benthic Boundary Layer*, McCave, I. N. (Ed.), Plenum Press, New York, pp. 11-31.

[29] Huang, D., 1996. *Turbulent Mixing in a Tidal Channel.* MSc thesis, School of Earth and Ocean Sciences, University of Victoria, 125 pp.

[30] Jenkins, G. M., and D. G. Watts, 1968. *Spectral Analysis and its Applications*, Holden-Day, San Francisco, 525 pp.

[31] Johnson, G. C., T. B. Sanford, and M. O. Baringer, 1994a. Stress on the Mediterranean outflow plume: Part I. Velocity and water property measurements. *J. Phys. Oceanogr.*, **24**, 2072-2083.

[32] Johnson, G. C., R. G. Lueck, and T. B. Sanford ,1994b. Stress on the Mediterranean outflow plume: Part II. Turbulent dissipation and shear measurements. *J. Phys. Oceanogr.*, **24**, 2084-2092.

[33] Jones, D.W., 1989. *Velocity Profiler (XCP) Observations of a Bottom Boundary Layer in the Strait of Juan de Fuca.* Technical Report, APL-UW TR8927, Applied Physics Laboratory, University of Washington, 209 pp.

[34] Kaimal, J. C., J. C. Wyngaard, Y. Izumi, and O. R. Cote, 1972. Spectral characteristics of surface-layer turbulence. *Quart. J. R. Met. Soc.*, **98**, 563-589.

[35] Kalkwijk, J. P. T., and R. Booij, 1986. Adaption of secondary flow in near-horizontal flow. *J. Hydraul. Res.*, **24**, 19-37.

[36] Lohrmann, A., B. Hackett, and L. P. Roed, 1990. High resolution measurements of turbulence, velocity and stress using a pulse-to-pulse coherent sonar. *J. Atmos. Oceanic Technol.*, **7**, 19-37.

[37] Lueck, R. G., 1987. Microstructure measurements in a thermohaline staircase. *Deep-Sea Res.*, **10**, 1677-1688.

[38] Lueck, R. G., D. Huang, D. Newman, and J. Box, 1997. Turbulence measurement with a moored instrument. *J. Atmos. Oceanic Technol.*, **14**, 143-161.

[39] Lueck, R. G., and D. Huang, 1997. Dissipation measurements with a moored instrument in a swift tidal channel. *J. Atmos. Oceanic Technol.*, submitted.

[40] Lynch D. R., J. T. C. Ip, C. E. Naimie, and F. E. Werner, 1996. Comprehensive coastal circulation model with application to the Gulf of Maine. *Cont. Shelf Res.*, **16**, 875-906.

[41] McPhee, M. G., 1994. On the turbulent mixing length in the oceanic boundary layer. *J. Phys. Oceanogr.*, **24**, 2014-2031.

[42] Mellor, G. L., and T. Yamada, 1982. Development of a turbulence closure model for geophysical fluid problems. *Rev. Geophys. Space Phys.*, **20**, 851-875.

[43] Mellor, G. L., and T. Yamada, 1982. Development of a turbulence closure model for geophysical fluid problems. *Rev. Geophys. Space Phys.*, **20**, 851-875.

[44] Osborn, T. R., 1980. Estimates of the local rate of vertical dissipation from dissipation measurements. *J. Phys. Oceanogr.*, **10**, 83-89.

[45] Osborn, T. R. and C. S. Cox, 1972. Oceanic fine structure. *Geophys. Fluid Dyn.*, **3**, 321-345.

[46] Osborn, T. R., and W. R. Crawford, 1980. An airfoil probe for measuring turbulent velocity fluctuations in water. In: *Air-Sea Interactions: Instruments and Methods*, Dobson,f., L. Hasse, and R. Davis (Eds.), Plenum, 801 pp.

[47] Peters, H., M. C. Gregg, and T. B. Sanford, 1995. Detail and scaling of turbulent overturning in the Pacific Equatorial Undercurrent. *J. Geophys. Res.*, **100**, 18,333-18348.

[48] Schauer, U., 1987. Determination of bottom boundary layer parameters at two shallow sea sites using the profile method. *Cont. Shelf Res.*, **7**, 1211-1230.

[49] Schumann, E. H. , 1986. The bottom boundary layer inshore of the Agulhas Current off Natal in August 1975. *S. Afri. J. Mar. Sci.*, **4**, 93-103.

[50] Simpson, J. H., W. R. Crawford, T. P. Rippeth, A. R. Campbell, and J. V. S. Cheok, 1996. The vertical structure of turbulent dissipation in shelf seas. *J. Phys. Oceanogr.*, **26**, 1579-1590.

[51] Soulsby, R. L., 1977. Similarity scaling of turbulence spectra in marine and atmospheric boundary layers. *J. Phys. Oceanogr.*, **7**, 934-937.

[52] Soulsby, R. L.,1980. Selecting record length and digitization rate for near-bed turbulence measurements. *J. Phys. Oceanogr.*, **10**, 208-219.

[53] Soulsby, R. L., 1983. The bottom boundary layer of shelf seas. In: *Physical Oceanography of Coastal and Shelf Seas*, Johns, B. (Ed.), Elsevier Oceanography Series, **35**, Elsevier, Amsterdam, pp. 189-266.

[54] Soulsby, R. L., and K. R. Dyer, 1981. The form of the near-bed velocity profile in a tidally accelerating flow. *J. Geophys. Res.*, **86**, 8067-8074.

[55] Stacey, M. T., 1996. *Turbulent Mixing and Residual Circulation in a Partially Stratified Estuary.* Ph.D. thesis, Stanford University, 209 pp.

[56] Stacey, M. T., S. G. Monismith, and J. R. Burau, 1997. Observations of turbulence in a partially stratified estuary. *J. Phys. Oceanogr.* (submitted).

[57] Taylor, P. A., and K. R. Dyer, 1977. The theoretical models of flow near the bed and their implication for sediment transport. In: *The Sea*, Vol. 6, Goldberg, E. D., I. McCave, J. J. O'Brien, and J. H. Steele (Eds.), Wiley-Intersciences, New York, pp. 579-601.

[58] Tennekes, H., 1973. The logarithmic wind profile. *J. Atmos. Sci.*, **30**, 234-238.

[59] Tennekes, H., and J. L. Lumley, 1972. *A First Course in Turbulence.* The MIT Press, 300 pp.

[60] Thompson, R. E., 1981. *Oceanography of the British Columbia Coast.* Canadian Special Publication of Fisheries and Aquatic Science, **56**, 291 pp.

[61] Turner, J. S., 1973. *Buoyancy Effects in Fluids.* Cambridge University Press, 367 pp.

[62] van Haren, H., N. Oakey, and C. Garrett, 1994. Measurements of internal wave band eddy fluxes above a sloping bottom. *J. Mar. Res.*, **92**, 909-946.

[63] Wolanski, E., J. Imberger, and M. L. Heron, 1984. Island wakes in shallow coastal waters. *J. Geophys. Res.*, **89**, 10553-10569.

[64] Xing, J., and A. M. Davies, 1996. The influence of mixing length formulation and stratification upon tidal currents in shallow seas. *Cont. Shelf Res.*, **42**, 417-456.